



HAL
open science

Advancements in laser doppler holography for retinal blood flow imaging

Zofia Bratasz

► **To cite this version:**

Zofia Bratasz. Advancements in laser doppler holography for retinal blood flow imaging. Medical Imaging. Université Paris sciences et lettres, 2024. English. NNT : 2024UPSLS035 . tel-04951894

HAL Id: tel-04951894

<https://pastel.hal.science/tel-04951894v1>

Submitted on 17 Feb 2025

HAL is a multi-disciplinary open access archive for the deposit and dissemination of scientific research documents, whether they are published or not. The documents may come from teaching and research institutions in France or abroad, or from public or private research centers.

L'archive ouverte pluridisciplinaire **HAL**, est destinée au dépôt et à la diffusion de documents scientifiques de niveau recherche, publiés ou non, émanant des établissements d'enseignement et de recherche français ou étrangers, des laboratoires publics ou privés.

THÈSE DE DOCTORAT

DE L'UNIVERSITÉ PSL

Préparée à ESPCI Paris
Institut Langevin

**Advancements in laser doppler holography for retinal
blood flow imaging**

**Avancées en holographie laser Doppler pour l'imagerie
du flux sanguin rétinien**

Soutenue par

Zofia BRATASZ

Le 2 Octobre 2024

Ecole doctorale n° 564

Physique en Ile de France

Spécialité

Physique

Composition du jury :

Serge, MEIMON DR, Onera	<i>Président</i>
Corinne, FOURNIER MCF, Université Jean Monnet	<i>Rapporteur</i>
Rainer, LEITGEB MCF, Medical University of Vienna	<i>Rapporteur</i>
Mickaël, TANTER Professeur, ESPCI	<i>Examineur</i>
Sebastien, POPOFF CR, ESPCI - Institut Langevin	<i>Examineur</i>
Kate, GRIEVE DR, Sorbonne Université SIM	<i>Directeur de thèse</i>

Acknowledgements

The work presented in this thesis manuscript would not have been possible without the support, guidance, and encouragement of numerous individuals over the past three years. First and foremost, I would like to express my heartfelt gratitude to Pedro Mecê and Olivier Thouvenin for their exceptional guidance during the most challenging aspects of this journey, both scientifically and personally. Their unwavering dedication to the mentorship of their students has been truly inspiring.

I am also deeply thankful to Kate Grieve and Sébastien Popoff for their steadfast support and for fostering a strong sense of belonging within the scientific community. Their encouragement has been invaluable throughout this endeavor.

My sincere thanks extend to the remarkable teams at both the Quinze-Vingts Hospital and the Langevin Institute. Their generosity in sharing knowledge and assisting in the pursuit of answers to scientific questions has been instrumental in this work. In particular, I would like to thank Michel Paques, Romain Pierrat, Claire Prada, and François Bruno for their expertise and willingness to collaborate.

I am especially grateful to Léo Puyo for his dedication and readiness to share his deep knowledge of Laser Doppler Holography, ensuring the continuity and success of this project.

Lastly, I want to acknowledge the immense importance of the camaraderie and support provided by my fellow PhD students. Their companionship has been a cornerstone of this journey, making it both productive and fulfilling.

Advances in Laser Doppler Holography

December 31, 2024

Contents

Introduction	3
I Context	7
1 Human Eye	8
1.1 Introduction	8
1.2 Vasculature of the human eye	9
1.2.1 Retinal Vasculature Network	10
1.2.2 Choroidal Vasculature Network	12
1.3 Blood flow dynamic	13
1.3.1 Ocular pathologies that modify blood perfusion	15
1.4 Model of the eye and light scattering in the eye fundus	16
1.5 Ocular Aberrations	17
1.6 Eye Movements	19
2 Digital Holography and Doppler Broadening	21
2.1 Principles	21
2.2 Fresnel propagation	22
2.3 Angular spectrum domain	23
2.4 Circular convolution and angular composition of the holograms	25
2.5 Coherent detection acceptance angle	25
2.6 Doppler effect and spectrum broadening	26
3 Laser Doppler Holography	28
3.1 Introduction	28
3.2 Optical setup	28
3.3 Digital image rendering	29
3.3.1 Doppler broadening measurements and sampling frequency	31
3.4 Blood flow analysis in retinal and choroidal vessels of the human eye fundus	31
3.4.1 Signal analysis for the retinal vessels	32
3.4.2 Signal analysis for the choroidal arteries	34
3.4.3 Characterization of the Doppler waveform	35
3.4.4 Vessel identification	36
3.5 Image of the choroid vasculature	36
3.6 Passive retinal Arteries Elastography	37
3.7 Limitations and unresolved problems of LDH	40

II	Results	41
1	Wide-field imaging	42
1.1	Introduction	42
1.2	Article	42
1.3	Optical configuration	52
1.4	Conclusions	52
2	Aberration correction	53
2.1	Introduction	53
2.1.1	Adaptive Optics (AO)	53
2.1.2	Digital aberration correction (DAO)	55
2.1.3	Aberration correction for LDH	56
2.2	Aberration compensation in Doppler holography of the human eye fundus by sub-aperture signal correlation	59
2.3	Aberration measurements validation and sources of errors	75
2.4	Aberrometry	78
2.4.1	Astigmatism quantification	78
2.4.2	Peripheral aberrations	79
2.5	Conclusions	81
3	Quantitative estimation of blood flow	84
3.1	Introduction	84
3.2	State of the art	84
3.2.1	Color Doppler Imaging (CDI)	84
3.2.2	Laser Doppler Velocimetry (LDV) and Laser Doppler Flowmetry (LDF)	84
3.2.3	Doppler OCT	86
3.2.4	Proposition of Laser Doppler holography relative to other techniques	88
3.3	Segmentation	88
3.4	Statistics of Doppler effect and analysis of spectra	89
3.4.1	Introduction	89
3.4.2	Scatterer velocity and the distribution of the frequency shift	93
3.4.3	Preliminary analysis of the velocity	95
3.5	Velocity measurement	95
3.6	Conclusions and discussion	101
4	Retinal vessels elastography	102
4.1	Introduction	102
4.2	State of the art	103
4.3	Implementation	103
4.3.1	Finding curve signal	103
4.3.2	Extraction of velocities from the curve signal	104
4.4	Result	105
4.4.1	Dispersion curves	105
4.4.2	Time of flight measurements	106
4.5	Discussion and conclusion	111

5	Holowaves software	112
5.1	Introduction	112
5.2	Holowaves	112
5.3	Holowaves extension to FF-SS-OCT	113
5.4	Future perspectives for the Holowaves software	116
	Conclusions	116
5.5	Quantification du Flux Sanguin et Elastographie des Vaisseaux Rétiniens	123
5.6	Perspectives et Conclusions	125

Introduction

Currently, our society is aging at a much faster rate than ever before. According to the World Health Organization (WHO), by the year 2030, 1 in 6 people in the world will be aged 60 or older. This demographic shift requires ensuring that health and social systems are prepared to support the elderly. For a long time, the problem of rapidly aging societies was associated with well-developed and wealthy countries, whose citizens could afford expensive and specialized healthcare. However, the WHO states that by the year 2050, two-thirds of world's population over 60 years will be living in middle- or lower-income countries. The global challenge arising from this trend is to provide affordable and widely available healthcare.

Eye conditions are one of the most common health issues in the elderly. As a result, the great majority of patients touched by eye-related diseases is above the age of 50. The most common eye diseases affecting the elderly - refractive errors and cataracts - are related to the anterior segment of the eye and are relatively easy to treat. Other conditions, slightly less common but still touching a significant proportion of older people - glaucoma, age-related macular degeneration and diabetic retinopathy - affect the posterior segment of the eye which is a far more complex and sensitive structure. Treatment of these conditions presents a significant challenge. As a result, early detection of abnormalities in the structure and physiology of the eye fundus is crucial. The high prevalence of eye conditions among the elderly, combined with the general global aging tendencies make us believe that the demand for novel diagnostic devices and treatments will continue to increase.

Moreover, the study of the eye has applications beyond the field of ophthalmology. The human retina is unique as it is the only specialized organ not shielded by protective tissues like skin and bone, making it the only part of the body where underlying structures can be imaged using visible light. As a result, the retina can be observed in vivo with a resolution of several microns. This unparalleled accessibility allows for detailed examination and monitoring of not only ocular health but also systemic conditions. Additionally, the retina is considered as an extension of the brain, which is one of the most difficult organs to image as it is almost entirely covered by a bone layer—the skull. Transcranial imaging is extremely difficult for both light-based and ultrasound techniques due to the drastic variations in scattering and elastic properties of the tissues. Consequently, the resolution of brain maps obtained remains limited. Many techniques are being developed to overcome these limitations. However, the versatility of retinal imaging techniques, and their unrivaled resolution makes the eye the best medium for detecting conditions that impact the entire nervous system, such as multiple sclerosis, Alzheimer's disease, and Parkinson's disease. Additionally, retinal imaging enables assessment of the health of the microvasculature structure which supplies nutrients to neural tissue. As a result, diseases such as diabetic retinopathy and hypertension-related complications can be diagnosed. In conclusion, there can be no doubt that retinal imaging is of crucial importance for providing healthcare.

Almost every article dedicated to retinal imaging begins by highlighting the great success of Optical Coherence Tomograph (OCT) - a technique which enabled acquiring cross-section images of the retina. Since its invention in the early 1990s, OCT has become a staple in essentially every ophthalmological clinic. A subsequent milestone occurred in 1997 with the introduction of adaptive optics to retinal imaging and vision science, which enabled resolving photoreceptors mosaic. Another innovation which has a potential to revolutionize eye imaging is the holographic detection scheme, which enables the detection of phase information about the field scattered by the sample. As a result, the axial resolution of images obtained is significantly increased. Moreover, by capturing both the amplitude and the phase components, we possess all the information necessary to fully describe the wavefront arriving at the detector. With this comprehensive data, we can digitally apply a variety of optical processing techniques. These include digital refocusing, aberration correction, three-dimensional reconstruction, and phase unwrapping. This capability allows for unprecedented

control and manipulation of optical images, leading to improved accuracy and versatility in imaging applications.

The emergence of phase-sensitive techniques has been made possible by significant advancements in ultra-fast detection schemes. In 2010, ultra-fast cameras were capable of achieving acquisition speeds of approximately 10,000 to 50,000 frames per second (fps) for 512x512 pixel frames. By 2023, technological progress had dramatically increased these speeds. Modern ultra-fast cameras can now capture 512x512 pixel frames at rates exceeding 100,000 fps, with some specialized models reaching up to 1,000,000 fps or more. This substantial improvement has greatly enhanced the ability to observe and analyze high-speed phenomena with much greater temporal resolution. In-vivo imaging of the human eye requires ultra-fast detection schemes due to the eye's constant movement. To achieve phase-sensitive resolution at the nanometer scale, it is essential to ensure that the observed structures remain stable at this level throughout the acquisition time. Consequently, lateral, axial, and temporal resolutions are inherently interconnected, and the development of higher-resolution techniques will inevitably be accompanied by advancements in ultra-fast detection schemes.

This thesis concentrates on Laser Doppler Holography (LDH), a novel, holographic technique, developed to image blood flow in the eye. The holographic detection scheme allows us to benefit from the domain of numerical processing. LDH is a technique which meets the existing demand for eye fundus imaging technologies and the newly emerging phase-sensitive detection. This manuscript is divided into two parts. In the first part of this manuscript - which consists of 3 Chapters - we will provide the context of this work. In Chapter 1, we will introduce the anatomy, physiology, and pathologies of the human eye. In Chapter 2, we will introduce digital holography and Doppler broadening measurement with basic concepts for image reconstruction in Laser Doppler Holography. Finally, in Chapter 3, we will describe previous works on LDH, discussing its capacities and limitations at the beginning of this thesis. The second part of the manuscript - consisting of five Chapters - will be dedicated to advancements in LDH technology resulting from my work. These can be divided into four main domains: modification of the optical setup, aberration compensation, blood flow quantification model, and retinal vessel elastography. With the exception of the first, all of these chapters begin with a discussion of the state-of-the-art and positioning of LDH. Finally, the manuscript ends with conclusions drawn from this work and the possible directions for improvements.

Part I
Context

Chapter 1

Human Eye

1.1 Introduction

The eye is a complete imaging system which allows the reconstruction of full-field, high resolution images of objects placed at different distances. The light arriving towards the eye first passes through the cornea with a refractive power of 43 diopters (D) (which corresponds to approximately $2/3$ of the total refractive power of the eye). It then crosses the anterior chamber filled with transparent aqueous humor to arrive on the iris which controls the amount of light which enters the rest of the eye. Next, it passes through the crystalline lens - an elastic tissue which enables the accommodation. The refractive power of the crystalline lens in the resting state (when the eye does not accommodate) is typically around 20-22 D, and it can increase by approx. 15 D when accommodating. Finally, the eye passes through the posterior chamber (filled with vitreous humor) and arrives at the retina, which acts as a detector. The visual axis of the eye is inclined with respect to the optical axis by 5° [1].

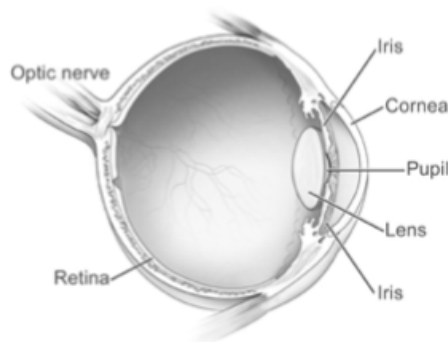


Figure 1.1: Credits the National Eye Institute, National Institute of Health. Cross-section view of the human eye representing the key eye structures in the anterior segment (iris, cornea, pupil, lens - which is also referred to as crystalline lens, and iris) as well as in the posterior segment (retina, optic nerve head).

The retina is a complex and delicate tissue lining the innermost layer of the eye. It comprises distinct layers that collectively enable the process of vision (Fig. 5.3). Beginning with the outermost layer, the retinal pigment epithelium (RPE) lies adjacent to the choroid, a vascular layer lying underneath the retina. The RPE plays a role in light absorption, nutrient transport, and the maintenance of photoreceptors. On top of the RPE lies the photoreceptor layer, consisting of specialized cells that capture light and initiate visual signals. Above the photoreceptor layer, there are several layers of neurons, which allow for pre-processing and transferring of the signal detected by the photoreceptors to the brain.

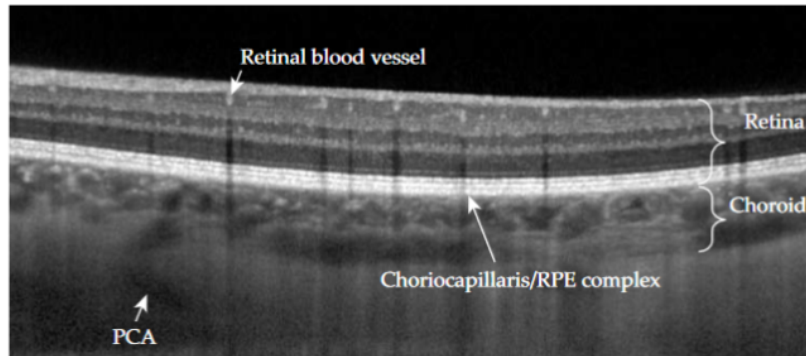


Figure 1.2: Figure adapted from [2]. The layered structure of the human eye fundus seen with OCT. The layers of the retina are well visible as well as some of its vessels. Underneath we can distinguish the choroid. The structures get considerably blurred closer to the sclera whose outline is effectively invisible. PCA refers to posterior ciliary arteries which are discussed in the following sections.

The human eye is equipped with two primary types of photoreceptor cells - rods and cones, each playing a crucial role in visual perception. Rods, abundant in the peripheral retina, are highly sensitive to low levels of light and facilitate vision in dim conditions, such as during night-time. They contribute to peripheral and low-resolution vision but cannot discriminate between colors. On the other hand, cones, concentrated in the fovea, are responsible for high-acuity and color vision. There are three subtypes of cones, each sensitive to different spectral ranges, allowing us to perceive a spectrum of colors.

The eye fundus is a term used to describe the interior part of the eye globe, which lies opposite to the iris. Different retinal structures can be identified such as optic disc, macula, fovea, and posterior pole (Fig.1.3). Different layers of the eye vary greatly in their properties depending on their position. For example, the fovea, which is the center of vision, has a higher density of cones and is vasculature-free. On the other hand, the cones in the periphery are more sparse, rods are the most common found type of photoreceptors in this region and the choroid layer lying beneath is full of large vessels.

1.2 Vasculature of the human eye

The blood supply of the human eye is provided by the ophthalmic artery which separates into central retinal artery (CRA), which enters the eye through optic nerve, and posterior ciliary arteries (PCAs) which penetrate the eye through the sclera (Fig. 1.4). These two branches create two distinct systems of blood vessels - retinal and choroidal - meaning that no exchange of fluids between the two systems takes place within the eye.

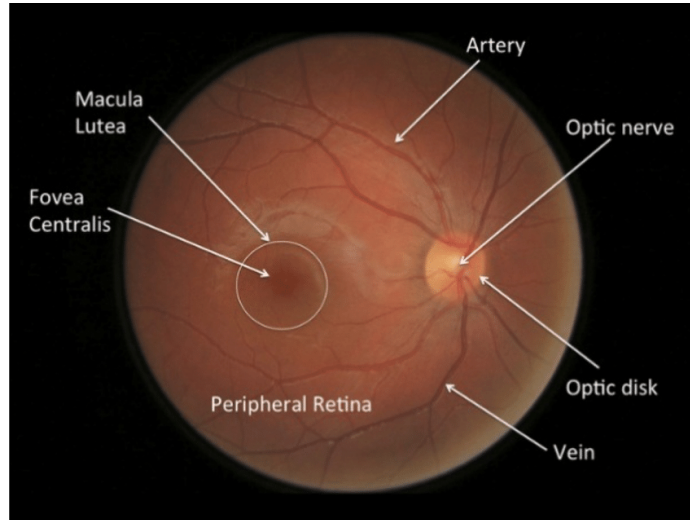


Figure 1.3: Figure adapted from [3] representing a photograph of the human eye fundus. Main areas of the retina, which are relevant throughout this manuscript are labeled. Optic nerve is also referred to as optic nerve head (ONH).

The intricate structure of the retina requires a specialized yet efficient blood supply system. Given that the retina can be classified as an extension of the brain, the preservation of the brain-blood barrier (BBB) is crucial. The photoreceptor layer is actively engaged in the energy-intensive processes of capturing and processing light, and thus exhibits a heightened need for oxygen and nutrients. To meet these demands, photoreceptors are strategically positioned directly on the RPE, which interfaces with the choroid (Fig. 1.5). Meanwhile, the inner layers of neurons receive nourishment through a distinct network of retinal vessels. The integrity of the Retina Blood Barrier (RBB) is maintained by the inherent structure of the vessel walls. A detailed description of the anatomy of the eye vasculature is given in the following paragraphs.

1.2.1 Retinal Vasculature Network

The retinal blood supply arrives from the central retinal artery (CRA) which enters the eye through the optic nerve, where it splits into two main branches (superior and inferior), which again split into two, thus creating four branches that supply blood for the four quadrants of the eye - superior temporal and nasal, and inferior temporal and nasal. For each part of the retina, the blood supply is provided uniquely by its associated arterial branch - retinal arteries form a terminal system. As a result, any blockage or malfunction of those branches compromises the blood supply to some part of the retina and therefore constitutes a serious health risk. In around 18% of cases, in the vicinity of the optic nerve head, there may be another artery - derived from choroidal vasculature - which emerges at the surface and contributes to the blood supply of the retina. Most of the main branches and divisions of arteries and veins of the retina are comprised in the NFL, and then they dive deep into retinal tissue to form two separate layers of capillaries in the ganglion cell layer and the other in the inner nuclear layer. The arterial and venous networks are interconnected by a system of uniformly distributed capillaries. There are three regions of the retina which are devoid of a capillary system : the fovea, the optic nerve head and the areas adjacent to the main arteries and

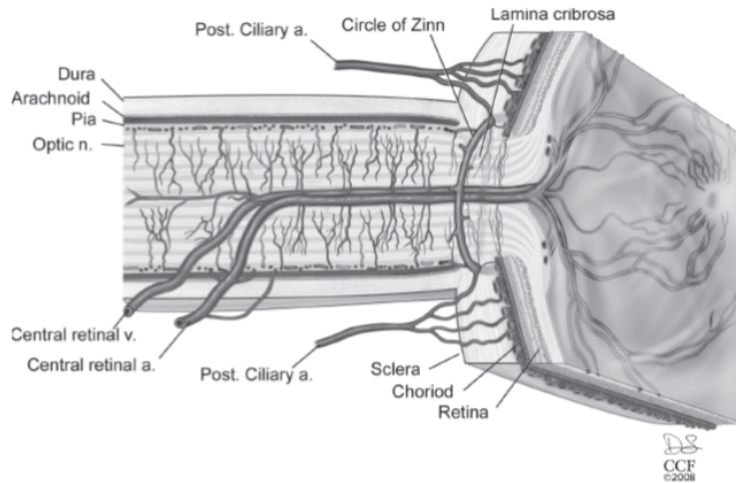


Figure 1.4: Drawings by Dave Schumick adapted from [4]. The blood supply is provided by CRA for the retina and multiple PCAs for the choroid.

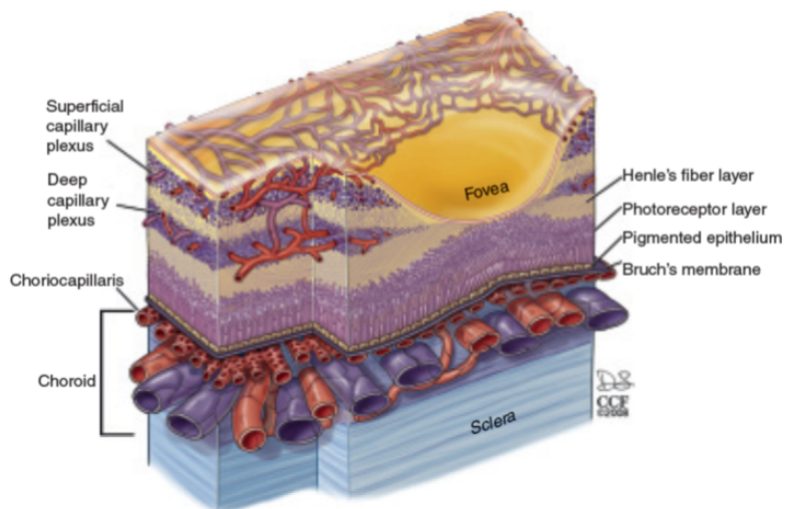


Figure 1.5: Drawing by David Schumick adapted from [4] representing layered structure of the eye fundus around fovea. Attention should be drawn to the distinctive layers of vasculature visible. In the retina there are two layers of capillary vessels referred to as superficial and deep capillary plexus. In the choroid vessels stack and form a thick sponge-like structure.

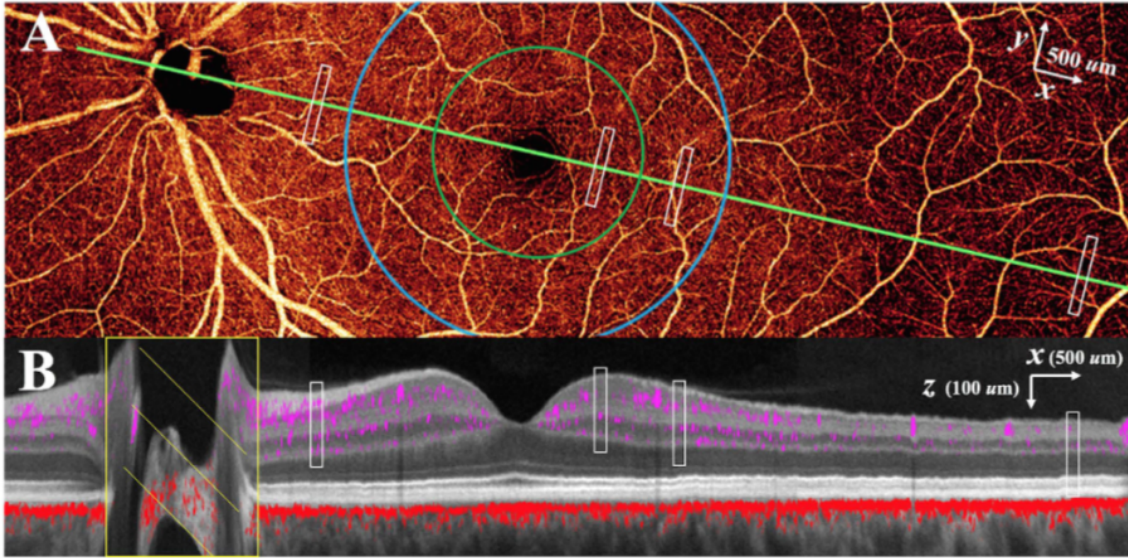


Figure 1.6: Image adapted from [5] representing the retinal vasculature. Images were obtained using OCT-A, subfigures A and B are en-face and B-section images respectively. We can clearly identify the two regions free of the retinal microvasculature: the first is fovea which is the centre of vision, the second one is the optic disc. We can also see that the areas in vicinity of the large vessels are avascular.

vein. The blood flow rate in the retina is considerably lower than that in the choroid. The arteries around the optic nerve head are of approximately $100\ \mu\text{m}$ diameter with $18\ \mu\text{m}$ wall thickness, and they steadily decrease in size, finally the size of the smallest capillaries have a lumen diameter of $3.5 - 6\ \mu\text{m}$ [4].

1.2.2 Choroidal Vasculature Network

The choroid provides almost the entire blood supply of the eye and extends to the level of the equator of the eye. The blood supply of the choroid is provided by between 10 and 20 short posterior ciliary arteries (SPCAs), which penetrate the sclera around the optic nerve head in varying distributions, in addition to two long posterior ciliary arteries (nasal and temporal), which provide blood flow to the anterior part of the choroid as well as the iris and ciliary body. After penetrating the sclera, the PCAs divide rapidly to form a capillary network—choriocapillaris—of freely anastomosing, fenestrated, single-layer vessels. This network is isolated from the RPE by Bruch's membrane, whose role is to regulate fluid flow. Unlike in the retina, the arteriovenous system in the choroid is asymmetrical. The outflow of blood in the choroid is centrifugal and is collected by large vortex veins (up to $300\ \mu\text{m}$) positioned far from the ONH. The blood flow velocities are approximately at least one order higher than those in the retina. Interestingly, the oxygenation difference between the veins and arteries in the choroid is only 5% compared to 40% in the retinal vasculature [6].

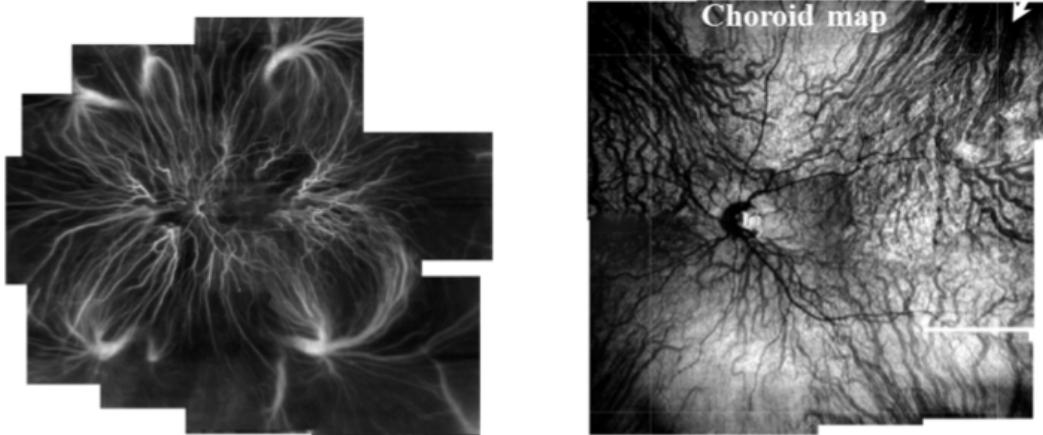


Figure 1.7: Figure adapted from [7]. On the left, we see stitched images of the late stage ICG angiography visualising retinal vasculature and choroidal veins, especially vortex veins providing drainage system. On the right, we can see stitched en-face images of OCT-A visualising the choroid vasculature. The total field of view of the ICG image montage is considerably bigger.

1.3 Blood flow dynamic

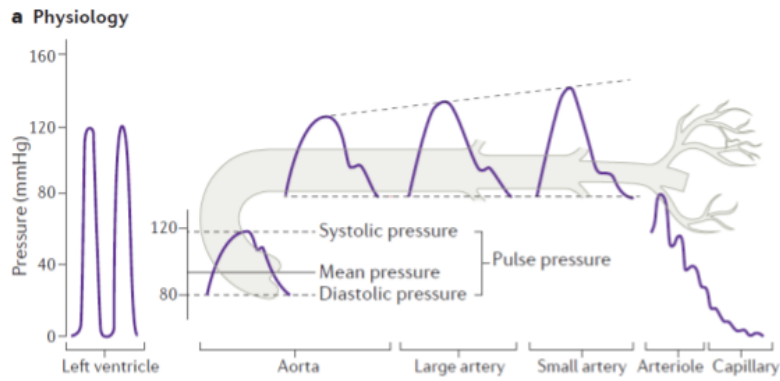
The role of vasculature is to transport and regulate the blood flow according to the needs of the organs it is delivered to. The flow rate is locally determined by a law analogous to Ohm's law in an electric circuit:

$$\Delta P = QR_h, \quad (1.1)$$

where ΔP is the pressure difference, Q is the flow rate, and R_h is the hemodynamic resistance, the origin of which is the friction on the vessel walls and the viscosity of the fluid. For laminar flow, the hemodynamic resistance can be calculated using Hagen–Poiseuille's law as:

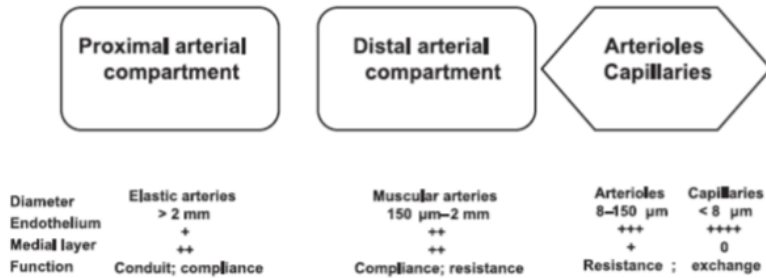
$$R_h = \frac{8\mu l}{\pi r^4}. \quad (1.2)$$

where μ is the blood viscosity and l, r stand for vessel's length and diameter respectively. The resistance is strongly dependent on the tube diameter. This property is employed by the organism to regulate the flow by changing the diameter of vessels. Flow dynamics are described by the waveform—flow rate as a function of time. The shape of the waveform changes greatly throughout the course of blood flow through the organism due to the varying properties of vessels (Fig. 1.8). The origin of flow is in the heart, from which a volume of blood gets ejected during muscle contraction into the vascular circuit. Pressure measured in the left ventricle as a function of time has a nearly rectangular form. The largest arteries are characterized by high compliance - meaning the capacity to dilate and shrink. The total volume of blood contained in those vessels can increase by 60% during systole. The result of this compliance is that it decreases the systolic pressure and induces a non-zero blood velocity during diastole, thus converting an intermittent pressure in the heart into a steadier flow. Moreover, this elastic dilation and shrinking gives rise to a pulse wave propagating along the arteries which is characterized by pulse wave velocity (PWV). As blood further propagates in the vascular tree into smaller arteries and arterioles, pressure decreases and the resistance plays a crucial role in controlling the level of flow. In the aim of creating a nearly steady flow - which



(a)

MACRO- AND MICROVESSELS



(b)

Figure 1.8: Figures adapted from [10, 8]. (a) graph describing the intermittent pressure variations in the left ventricle of the heart (left) and evolution of the waveform in vascular tree. (b) represents the classification of the arteries with corresponding parameters allowing to explain the change in the pulse waveforms.

promotes oxygen extraction - the arterioles increase in size during diastole to reduce the resistance. It is interesting to note that depending on the size of arteries and local pressure, the increase of diameter can either reduce or boost the blood flow.

So far, we have described the waveform with regards to the difference between systolic and diastolic flow. Another important characteristic is the presence of a secondary peak appearing after the systole, which is referred to as the dicrotic notch. Its presence can be explained by considering the pulse as a wave propagating through the vessels. This wave gets reflected at the sites of bifurcations due to the impedance mismatch. The wave reflections are considered to be the main reasons for differences between the pressure and flow rate functions [8].

There is relatively little information about the waveform in the retinal veins. Generally speaking, veins are believed to be non-pulsatile. However, the presence of a velocity wave has been observed in the central retinal vein using color Doppler imaging, indicating that the venous outflow is in fact pulsatile [9]. Moreover, it has been demonstrated that the measured waveform is synchronized with the intraocular pressure curve.

1.3.1 Ocular pathologies that modify blood perfusion

A number of pathologies result from or originate in abnormal blood perfusion of the eye, which can give rise to further problems due to a disturbed nutrient supply. We describe here the most common diseases linked to blood perfusion.

- **Glaucoma** is a group of diseases that affect the optic nerve head and cause vision loss. It is the second leading cause of blindness worldwide after cataracts. Glaucoma is considered to be linked to an increase in intraocular pressure (IOP); however, the optic nerve head can be affected even if the tension is at its normal level (normal-tension glaucoma). A hypothesis has been made linking high IOP with a blockage of the drainage system in the aqueous humor. One of the most common forms of the disease is open-angle glaucoma, which causes cupping of the ONH. Its first symptom is a loss of peripheral vision. As the retinal arteries are non-rigid, the increase in intraocular pressure influences the blood perfusion of the eye, making it more difficult for vessels to dilate and hence reducing blood flow. Multiple studies have demonstrated the link between glaucoma and modified blood flow in the eye [11, 12, 13, 14]. Furthermore, in some cases, a spontaneous pulsatility of the veins has been connected with glaucoma [15].
- **Diabetic retinopathy** is one of the leading causes of vision loss for patients with type 2 diabetes. The condition causes hyper-permeability of the retinal vessels, which can result in the formation of macular edemas and hard exudates. Unlike glaucoma, early-stage diabetic retinopathy does not change the patient's vision, and thus early detection is difficult. As a result, often, by the time it is detected, the damage to the retina is already considerable. In the late stage, vessel proliferation - that is, the apparition of new vessels - can be observed. Although the mechanisms behind this condition are not yet fully understood, a hypothesis has been made that retinal blood flow plays a role in the development of diabetic retinopathy [16, 17, 18].
- **Arterial stiffness** is a disease observed most often in the elderly and people suffering from arteriosclerosis. It is caused by a change in the viscoelastic properties of the arteries, which reduces the compliance of vessels and increases pulse wave velocity. As a result, the reflected wave gets superimposed with the forward propagation wave during the systolic peak rather than early diastole [8]. This means that the blood flow during systole is abnormally high and drops rapidly. Consequently, arterial stiffness modifies not only the total blood perfusion of the retina but also the waveform. The condition is directly linked with hypertension, which increases the risk of cardiovascular events. The detection of arterial stiffness is hence of great importance for their prevention.
- **Age-related Macula Degeneration (AMD)** is the most common cause of vision loss for people over 50 in the United States. It occurs in two forms - wet and dry. The wet form can be characterized by the abnormal proliferation of the choriocapillaris, which occasionally invades Bruch's membrane and causes the detachment of the RPE and a loss of central vision. The dry form of AMD, which represents 90% of cases, consists in the thickening of Bruch's membrane, which may cause the appearance of drusen - an accumulation of cellular material. Very often, the presence of drusen is asymptomatic, yet it can in some cases lead to the distortion or loss of vision. To this day, the explanation of the genesis of AMD is hypothetical as it is closely related to blood flow in the choroid, which is difficult to study. The main element that allows diagnosing it is the destruction of the RPE.

Layer	$L[\mu m]$	g	$l_s[\mu m]$
Neural Retina	200	0.97	49.4
RPE	10	0.84	6.3
choroid	100	0.94	20
sclera	700	0.9	18.2

Table 1.1: Table adapted from [?]. Optical parameters for eye fundus layer for a wavelength of 860 nm. L : the thickness of the layer, g : anisotropy factor, when equal to 1 the light is entirely forward scattered, when equal to 0 the scattering is fully isotropic, l_s : mean free path.

1.4 Model of the eye and light scattering in the eye fundus

For the purpose of conducting the measurements described in this manuscript, we use a simplified model of the eye. Firstly, for the estimation of the optical properties of the anterior segment of the eye, we use Emsley's model (Fig. 1.9). Furthermore, to describe light propagation and scattering

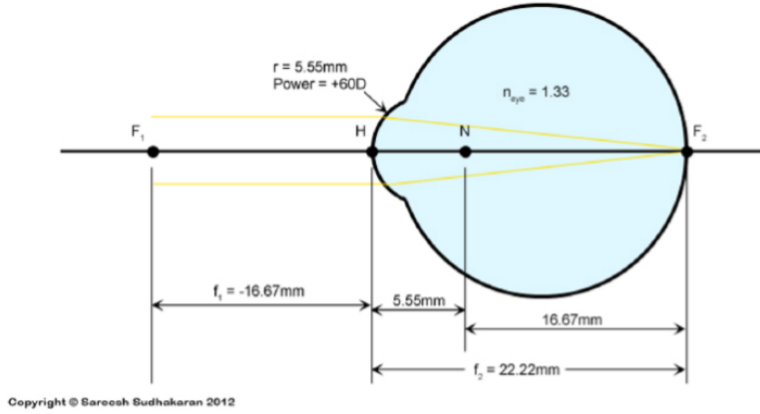


Figure 1.9: Figure adapted from [19]. Emsley model of the eye providing the distance between the cornea and both focal planes, refractive power, and refractive index inside the eye globe.

through the retina, we employ the results obtained by Léa Krafft in her thesis manuscript [19], by considering the eye fundus as a four-layer structure with the properties given in Tab. 1.1. Let us consider a beam of light that arrives at the eye fundus. The first layer encountered is the retina, which is mostly transparent. Occasional scattering is induced by red blood cells flowing within the vessels. The beam of light then arrives at the retinal pigmented epithelium (RPE). As mentioned in the introduction, it is a unicellular layer of highly pigmented skin cells. Here, the scattering is stronger, and part of the light gets absorbed; however, most of the light is still forward scattered. Deeper down, light crosses the choroid, where scattering is again induced by the red blood cells. Finally, it arrives at the sclera, which is a dense and highly scattering tissue. As a result, a small part of the incoming light is effectively back-scattered and once again travels through all the layers. We consider all throughout this manuscript that sclera acts as the secondary source of illumination [?, ?]

1.5 Ocular Aberrations

The cornea and the crystalline lens are not optically perfect and induce aberrations. Let us consider a light emitted by a punctual, monochromatic source at the fovea. In the absence of aberrations, the wavefront leaving the eye should be completely planar. The term "ocular aberration" refers to the difference between the ideal wavefront and the one which in reality emerges from the eye.

The functions typically used to describe aberration are Zernike polynomials, which can be divided into even and odd functions with respect to the azimuthal angle θ . The even polynomials are defined as:

$$Z_n^m(\rho, \theta) = R_n^m(\rho) \cos(m\theta) \quad (1.3)$$

and the odd ones as:

$$Z_n^{-m}(\rho, \theta) = R_n^m(\rho) \sin(m\theta) \quad (1.4)$$

Where $n \geq m \geq 0$. The $R_n^m(\rho)$ is a radial function which can be written as:

$$R_n^m(\rho) = \sum_{k=0}^{\frac{n-m}{2}} \frac{(-1)^k (n-k)!}{k! \left(\frac{n+m}{2} - k\right)! \left(\frac{n-m}{2} - k\right)!} \rho^{n-2k} \quad (1.5)$$

As one can see, Zernike polynomials are assembled into orders which are given by n . First and second rank have no impact on the quality of vision. The functions given by the second order are referred to as lower order aberrations. For $n > 2$ we talk about higher order aberrations. Alternatively, Zernike polynomials can be indexed linearly. The most common Zernike polynomials are represented in Tab. 1.2 along with the corresponding PSFs.

Damien Gatinel et al. [20] suggest that the Zernike polynomial basis has a drawback which is worth considering. It is argued that the faithfulness of representation of the physiopathology of refractive errors has been compromised for the orthogonality of the system. As an example one can take the 4th spherical aberration which is often associated with the keratoconus presence. To form an orthogonal basis, the polynomial is dependent on the radius (noted as ρ) not only to the power of 4 but also to the power of 2.

$$Z_4^0 = \sqrt{5} (6\rho^4 - 6\rho^2 + 1) \quad (1.6)$$

As a result, a typical aberrometer - projecting a wavefront on the basis of Zernike polynomials in the presence of 4th order dependency on radius - is also going to detect a very strong defocus. Whereas, in reality, it is possible that both contributions compensate. As a solution to that problem, the authors suggest conducting the projection on the Zernike basis rank by rank.

The most common eye pathology is hypermetropia, differently called near- or far-sightedness, which corresponds to the presence of defocus typically above 0.5 D. The prevalence of myopia and hyperopia in Europe is estimated at 27% and 23.1% respectively [21]. The world trends suggest a steady increase in the prevalence of myopia, particularly in China. The blurring caused by this aberration can be easily corrected with glasses or contact lenses.

The second most frequent ocular aberration is astigmatism, which can be seen as a difference of refractive index between different meridians of the eye. It can be induced by either the crystalline lens or cornea. We distinguish regular and irregular astigmatism. In the first case, the two meridians with maximal difference are perpendicular: in this case, the astigmatism can be corrected with glasses. In the case of irregular astigmatism, the two meridians are not perpendicular: this type of wavefront distortion is associated with higher order Zernike polynomials. The prevalence of astigmatism in Europe is estimated at 39.7% among adults [21], the corresponding values for other regions can be found in the Tab. 1.3.


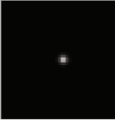

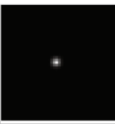
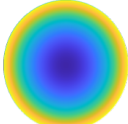
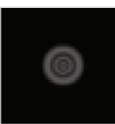
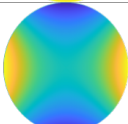

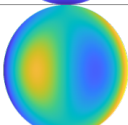

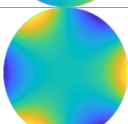

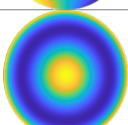
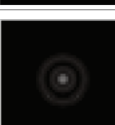
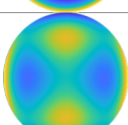
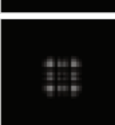
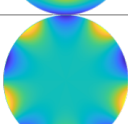

#	Zernike coefficient	Zernike orthogonal circle polynomial	Aberration name	WF map	PSF
1	Z_0	1	Piston		
2	Z_1^{-1}	$2\rho\cos\vartheta$	Tip/Tilt		
3	Z_1^1	$2\rho\sin\vartheta$			
4	Z_2^0	$3^{1/2}(2\rho^2 - 1)$	Defocus		
5	Z_2^2	$6^{1/2}(\rho^2\cos 2\vartheta)$	Astigmatism		
6	Z_2^{-2}	$6^{1/2}(\rho^2\sin 2\vartheta)$			
7	Z_3^{-1}	$8^{1/2}(3\rho^3 - 2\rho)\sin\vartheta$	Coma		
8	Z_3^1	$8^{1/2}(3\rho^3 - 2\rho)\cos\vartheta$			
9	Z_3^{-3}	$8^{1/2}(\rho^3\cos 3\vartheta)$	Trefoil		
10	Z_3^3	$8^{1/2}(\rho^3\cos 3\vartheta)$			
11	Z_4^0	$5^{1/2}(6\rho^4 - 6\rho^2 + 1)$	Spherical Aberration		
12	Z_4^{-2}	$10^{1/2}(4\rho^4 - 3\rho^2)\cos 2\vartheta$	Secondary Astigmatism		
13	Z_4^2	$10^{1/2}(4\rho^4 - 3\rho^2)\sin 2\vartheta$			
14	Z_4^{-4}	$10^{1/2}\rho^4\cos 4\vartheta$	Quadrafoil		
15	Z_4^4	$10^{1/2}\rho^4\sin 4\vartheta$			

Table 1.2: The first fifteen Zernike polynomials are given as a function of radius and azimuthal angle. In the column on the right, one can see associated PSFs which give an intuition about the impact of each aberration on the vision quality.

Estimated pool prevalence (EPP) of myopia, hyperopia, and astigmatism in children and adult by WHO regions.

Astigmatism	Astigmatism	Hyperopia	Myopia
	%EPP(95%CI); weight	%EPP(95%CI); weight	%EPP(95%CI); weight
Children			
Africa	14.2 (9.9–18.5); 10.33	3.0 (1.8–4.3); 10.57	6.2 (4.8–7.6); 16.48
Americas	27.2 (26–28.4); 2.11	14.3 (13.4–15.2); 4.14	8.4 (4.9–12); 6.09
South-East Asia	9.8 (6.3–13.2); 16.47	2.2 (1.2–3.3); 20.89	4.9 (1.6–8.1); 8.52
Europe	12.9 (4.1–21.8); 6	9 (4.3–13.7); 1.04	14.3 (10.5–18.2); 16.04
Eastern Mediterranean	20.4 (14.5–26.3); 29.11	6.8 (4.9–8.6); 30.75	9.2 (8.1–10.4); 26.69
Western Pacific	12.1 (8.4–15.8); 35.98	3.1 (1.9–4.3); 32.59	18.2 (10.9–25.5); 26.18
All	14.9 (12.7–17.1); 100	4.6 (3.9–5.2); 100	11.7 (10.5–13.0); 100
Adult			
Africa	11.4 (2.1–20.7); 8.85	38.6 (22.4–54.8); 6.54	16.2 (15.6–16.8); 2.01
Americas	45.6 (44.1–47.1); 2.95	37.2 (25.3–49); 13.05	22 (16.4–27.7); 7.98
South-East Asia	44.8 (36.6–53.1); 17.58	28 (23.4–32.7); 21.79	32.9 (25.1–40.7); 18.02
Europe	39.7 (34.5–44.9); 8.82	23.1 (6.1–40.2); 4.36	27 (22.4–31.6); 29.99
Eastern Mediterranean	41.9 (33.6–50.2); 29.39	33 (26.9–39); 19.54	24.1 (14.2–34); 13.98
Western Pacific	44.2 (30.6–57.7); 32.41	28.5 (20.1–37); 34.73	25 (20–30.1); 28.01
All	40.4 (34.3–46.6); 100	30.9 (26.2–35.6); 100	26.5 (23.4–29.6); 100

EPP: Estimated pool prevalence.
 CI: Confidence interval.

Table 1.3: Figure adapted from [21] representing the estimated prevalence for most common ocular aberrations. The data is grouped by regions. Distinctions are made between adults and children. The numbers were obtained by analysis of international databases for studies conducted between 1990 and 2016.

Castejon - Mochon et al. report that statistically only 9% of total RMS corresponds to the higher order aberrations [22]. The presence of other pathological conditions such as keratoconus - which is caused by thinning of the cornea - can induce elevated levels of coma and irregular astigmatism. Pathologies inducing higher order aberrations are considerably more difficult to treat as they cannot be corrected using glasses because lenses designed to correct aberrations of higher order on the optical axis would necessarily induce higher order aberrations in all other directions [23].

The level of aberration, especially of higher order, depends on the pupil size. Its diameter varies typically between 2-8 mm depending on the level of illumination. In the case of a perfect optical system, the PSF should decrease with the pupil dilatation and improve the resolution. However, usually, the presence of higher order aberrations jeopardizes this effect (Fig. 1.10). The wavefront error induced by the human eye is dynamic [24, 25]. Its variations can be associated with: the presence of the tear film, cardiac pulses and fixational eye movements.

1.6 Eye Movements

Eyeball position is maintained by six extraocular muscles. Eye movements can be divided into voluntary and involuntary. Firstly, let us discuss the movements which occur during fixation. Their role is to prevent the fading out of the image at fovea, which would happen due to the neural adaptation. We distinguish three main components of fixation movements [27]:

- **tremor** - small sinusoidal oscillations, with small amplitude (similar to the cone diameter) and high frequency (≈ 90 Hz),
- **drift** - slow curvilinear movements of approximately $0.5^\circ/s$, which gets superimposed to the tremor and drives the eye away from the fixation target,

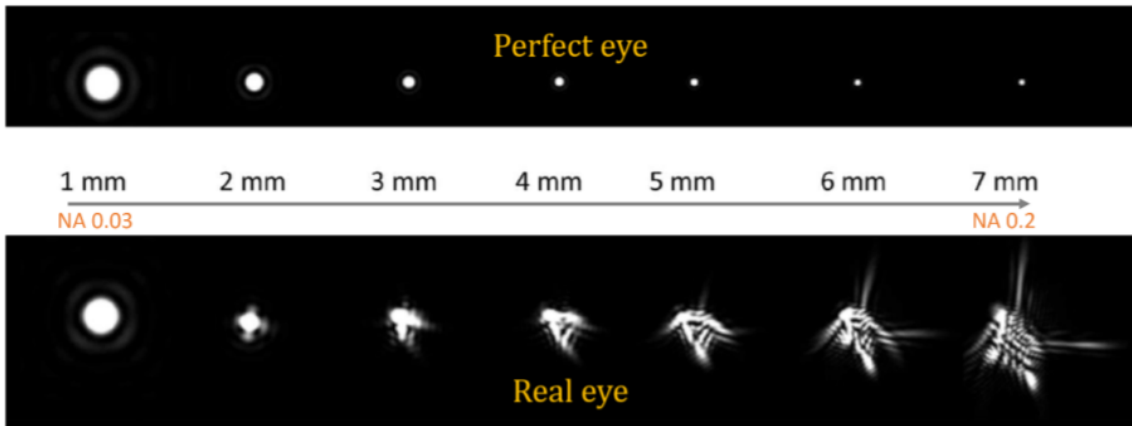


Figure 1.10: Figure adapted from [26]. The comparison between the PSF for the perfect and real eye depending on pupil size is made. In a perfect optical system, increasing pupil size should lead to decreasing the diffraction-limited focal spot. However, in the case of the eye this is not the case and the best resolution is obtained for a relatively small pupil diameter.

- **micro-saccades** - fast (from 20 to 100 °/s), jerk-like movements which probably occur to compensate for the displacement caused by drift.

Additionally, the eye is in constant axial movement, which is induced by head and body movements or physiological factors such as cardiac cycle, blood pressure, or respiration [28]. In conclusion, the movements are omnipresent and can represent a real challenge when trying to image the retina.

Chapter 2

Digital Holography and Doppler Broadening

2.1 Principles

The principle of digital holography is to record interference between the object and the reference beam whose wavefront is known, and then numerically propagate the field recorded to recover information about the scattering object. We can express the intensity recorded in the camera plane:

$$I(t) = \frac{1}{2} \epsilon_0 c \left(|E(t)|^2 + |E_{LO}(t)|^2 + E_{LO}(t)E^*(t) + E_{LO}^*(t)E(t) \right), \quad (2.1)$$

where E and E_{LO} correspond to the electric field of the sample and reference arm respectively. Often, holography is performed in off-axis configuration, which enables separating the terms in Eq. 2.1 as they have different supporting spatial frequencies. However, this results in a trade-off on the field of view obtained [29].

In Laser Doppler holography, the interferometer is aligned in on-axis configuration, and separation between different terms is obtained thanks to Doppler broadening induced by the object imaged. Under the hypothesis that the intensity of reference beam is considerably higher than that of the sample arm, we can write that :

$$|E_{LO}|^2 \ll |E_{LO}^*E| = |E_{LO}E^*| \ll |E|^2 \quad (2.2)$$

The object term in the equation Eq. 2.1 can be neglected due to its low intensity. To reveal the cross terms, the image of the reference arm has to be removed. This can be done by temporal filtering as the spectrum of object field is broader than that of the reference arm, due to the Doppler effect. In consequence, the crossed terms intensity oscillates thanks to the frequency mismatch, whereas the intensity of the reference image remains constant. Applying a high-pass temporal filtering to the signal enables rejection of the reference image. As of now, we are capable of retrieving the two interferometric terms. Finally, the numerical propagation allows focusing one of those terms while blurring the other. For a sufficiently large propagation distance, the energy distribution of the twin image is homogenous across the field of view. In the end, the calculated image contains both phase and amplitude information about the scattering object.

It is worth noticing that it is possible to obtain Laser Doppler Holography images in the configuration where the image plane is conjugated with the camera plane, however this does not provide

phase information about the image.

In the rest of this chapter we will assume that the recording condition provides a direct access to the field scattered by the object that is to be revealed. The following calculations are based on "Introduction to Fourier Optics" by Joseph W. Goodman [30].

2.2 Fresnel propagation

The electromagnetic field in a plane z can be calculated using the Fresnel Kirchoff equation if we know the field which was diffracted in the aperture plane ($z = 0$). The formula goes as follows:

$$E(x', y', z) = \frac{i}{\lambda} \iint E(x, y, z = 0) \frac{\exp(-ik\rho)}{\rho} dx dy, \quad (2.3)$$

where ρ is the distance between a point in the aperture and the chosen plane, which can be written as :

$$\rho = \sqrt{z^2 + (x - x')^2 + (y - y')^2}. \quad (2.4)$$

We can use the Taylor expansion and neglect the terms of order higher than 2 under the hypothesis that:

$$\rho = z + \frac{(x - x')^2}{2z} + \frac{(y - y')^2}{2z} - \frac{[(x - x')^2 + (y - y')^2]^2}{8z^3} + \dots, \quad (2.5)$$

$$\frac{[(x - x')^2 + (y - y')^2]^2}{8z^3} \ll 1. \quad (2.6)$$

Finally, the field can be written as:

$$E(x', y', z) = \frac{i}{\lambda z} \exp(-ikz) \iint E(x, y, 0) \exp\left(\frac{-ik}{2z} [(x - x')^2 + (y - y')^2]\right) dx dy \quad (2.7)$$

If we expand the quadratic terms in the integral we can reveal the underlying Fourier transform:

$$E(x', y', z) = \frac{i}{\lambda z} \exp(-ikz) \iint E(x, y, 0) \exp\left(\frac{-ik}{2z} [(x^2 + y^2) + (x'^2 + y'^2) - (2xx' + 2yy')]\right) dx dy \quad (2.8)$$

Now, omitting the phase term, which has no impact on intensity recorded, we can obtain:

$$E(x', y', z) \propto \mathcal{F}\{E(z = 0) \times \frac{1}{i\lambda z} \exp\left[\frac{2i\pi z}{\lambda} + \frac{i\pi}{\lambda z} (x^2 + y^2)\right]\} \quad (2.9)$$

Which means that the field at distance z from the sensor array can be calculated as a Fourier transform of the detected field multiplied by the free-space propagation impulse response, which in the discrete basis of the sensor array can be expressed as:

$$h_{m,n} = \frac{1}{i\lambda z} \exp\left[\frac{2i\pi z}{\lambda} + \frac{i\pi}{\lambda z} (m^2 d^2 + n^2 d^2)\right] \quad (2.10)$$

Where m, n are pixel indexes in x and y directions, and d is the pixel pitch of the sensor array. This propagation method can be limited by Moire's effect deforming the kernel calculated, which occurs

when interfringe in a part of the image is smaller than twice the pixel pitch. To make sure that the kernel is correctly sampled, the propagation distance z has to obey:

$$\frac{\pi}{\lambda z} (n^2 d^2 - (n-1)^2 d^2) < 2\pi \quad (2.11)$$

Which under the assumption that number of pixels $N \gg 1$ leads us to:

$$\frac{Nd^2}{\lambda} < z \quad (2.12)$$

Fresnel propagation hence corresponds to multiplication by a phase mask, and a Fourier transform. The sampling step (pixel pitch in the reconstructed image) changes with reconstruction

$$\Delta x' = \frac{\lambda z}{Nd}, \Delta y' = \frac{\lambda z}{Md} \quad (2.13)$$

where N and M stand for number of pixels in x and y directions respectively.

2.3 Angular spectrum domain

Alternatively, the propagation can be considered in terms of evolution of the spatial frequencies of the field.

$$\hat{E}(f_x, f_y, 0) = \iint E(x, y, 0) \exp[-2i\pi(f_x x + f_y y)] dx dy, \quad (2.14)$$

$$E(x, y, 0) = \iint \hat{E}(f_x, f_y, 0) \exp[2i\pi(f_x x + f_y y)] df_x df_y. \quad (2.15)$$

Now lets consider the Helmholtz equation along the z direction:

$$\nabla_z^2 E + k_z^2 E = 0. \quad (2.16)$$

If we now substitute (2.15) in (2.16), we can obtain that:

$$\frac{d^2}{dz^2} \hat{E}(f_x, f_y, z) + (1 - f_x^2 - f_y^2) \hat{E}(f_x, f_y, z) = 0. \quad (2.17)$$

An elementary solution of this equation is:

$$\hat{E}(f_x, f_y, z) = \hat{E}(f_x, f_y, 0) \exp\left(2i\pi z \sqrt{1 - f_x^2 - f_y^2}\right). \quad (2.18)$$

Finally, in the direct space it can be written :

$$E(z) \propto \mathcal{F}^{-1}\{\mathcal{F}\{E(z=0)\} \times H(z)\}, \quad (2.19)$$

which in the discrete numerical corresponds to:

$$H_{m,n}(z) = \exp\left[\frac{2i\pi z}{\lambda} \sqrt{1 - \left(\frac{m\lambda}{Md}\right)^2 - \left(\frac{n\lambda}{Nd}\right)^2}\right] \quad (2.20)$$

The limit of this method is given by the discrete sampling in the angular space. The phase difference between two consecutive pixels cannot be higher than 2π , this gives a condition :

$$\sqrt{1 - \left(\frac{n\lambda}{Nd}\right)^2} - \sqrt{1 - \left(\frac{(n-1)\lambda}{Nd}\right)^2} < \frac{\lambda}{z} \quad (2.21)$$

Using second order Taylor expansion we obtain a good approximation for:

$$z < \frac{Nd^2}{\lambda}. \quad (2.22)$$

As one can see, these two methods have no theoretical limitations in terms of position of scattering object with respect to the camera (except Eq. 2.6). The only restrictions on their applicability lies in the system sampling capacities, which dictate the range of propagation distance. Moreover, the two methods are complementary and employed together allow to reconstruct the image at any distance from the sensor array.

The pixel pitch in angular spectrum propagation method does not change. In consequence, the size of the image reconstructed also remains equal to the size of the sensor array for all z . For the Fresnel propagation, the size of the pixels in the reconstructed image changes and so does the extension of the field sampled. This phenomenon is illustrated by the diagram in Fig. 2.1.

It has to be however kept in mind that those considerations are true as long as the magnification of the image remains constant, which is the case of the lensless. However, in the case of our optical setup this is not the case (see Chapter: Laser Doppler holography).

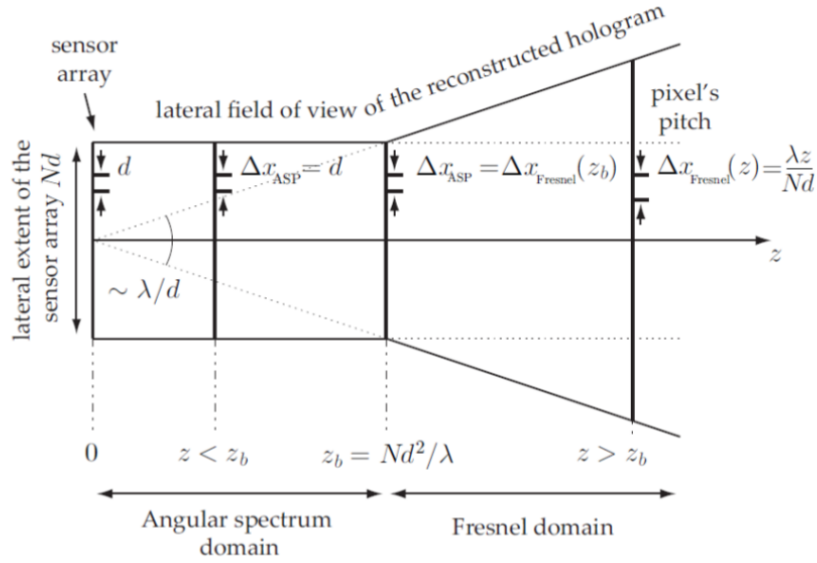


Figure 2.1: Diagram adapted from [2] representing the evolution of the pixel size in reconstruction, and in effect the field of view obtained for angular spectrum and Fresnel propagation.

2.4 Circular convolution and angular composition of the holograms

As mentioned above, the angular spectrum propagation method can be seen as a convolution of the recorded field by $H(z)$. If we calculate the angular propagation using the Eq. 2.19, the interferogram will be effectively periodically repeated before the convolution. This may result in parts of the field being reconstructed in false parts of the image.

To avoid this problem the interferogram should be zero-padded (in practice it is better to pad with a constant value equal to the average intensity of the interferogram) and multiplied with a kernel calculated over the same number of pixels. As a result, the field of view of the hologram can be effectively extended above the size of the sensor array. Theoretically, to make sure that no features are misplaced, it would be necessary to use the size of padding equal to the size of interferogram. However, this is computationally very expensive and might not be necessary, as the extended field of view might be limited by the pupil size (Fig. 2.3).

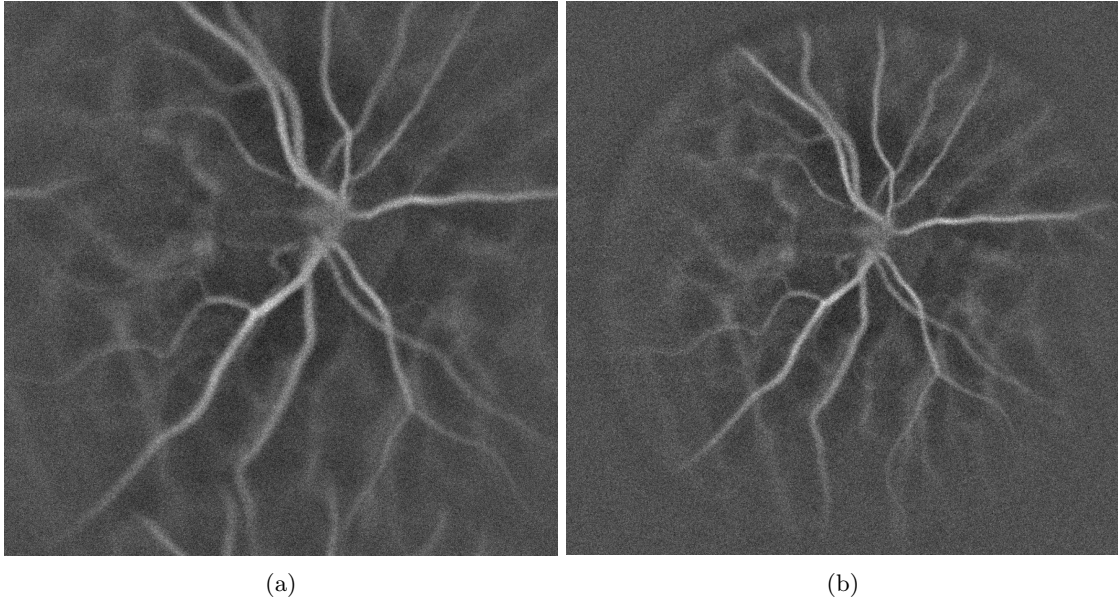


Figure 2.2: Laser Doppler holography images of the optic nerve head of a volunteer reconstructed using none (a) and with 25% (b) (lateral extension of field of view) padding of the interferograms.

2.5 Coherent detection acceptance angle

In holography, the maximal angle of coherent detection is determined by our capacity to correctly sample the interference fringes, which could be jeopardized if the difference between two consecutive fringes is lower than twice the pixel pitch. In the Fresnel propagation regime, where waves are considered plane at the sensor array, the maximal angle for which we can correctly sample the interferences is simply given by $\lambda/2d$, where λ is the wavelength and d is the pixel pitch. In the case of the angular spectrum propagation, this approximation is no longer valid and the limit angle cannot be easily deduced. To see how the acceptance angle varies with the propagation distance,

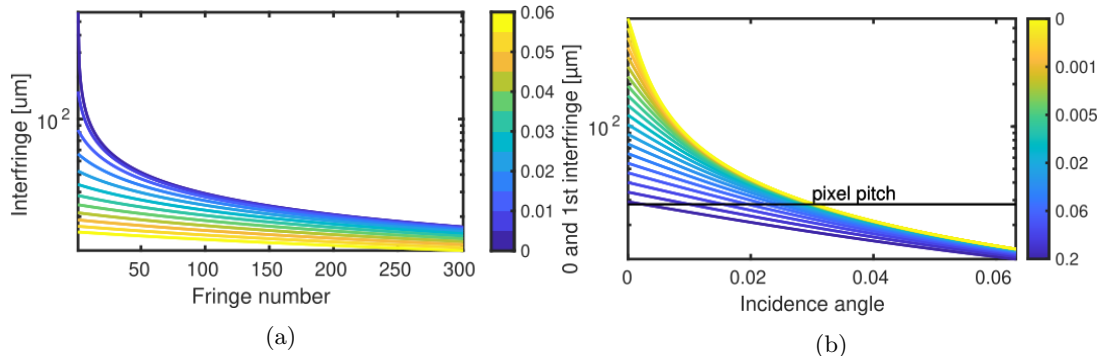


Figure 2.3: (a) Plot of interfringe as a function of the fringe number for different angles, calculated for the propagation distance of 20 cm. The colorbar gives the value of the incidence angle in radians. In the plot on the right (b) the length of the first interfringe is plotted in function of the incidence angle. The color encodes the propagation distance (in meters).

we have conducted a numerical simulation. Let us consider a source point placed at the distance $z = 0.2$ m above the center of sensor array, which emits spherical waves. We plot the interfringe in function of fringe number for different incidence angles.

Next, we try to determine for which angles at least one set of fringes is correctly sampled. To answer this question, we plot the size of the first interfringe in function of incidence angle for different propagation distances. The results suggest that the dependency between the two very quickly becomes linear.

Finally, we can plot the acceptance angle in function of propagation distance (Fig. 2.4). As one can see, for propagation distances larger than 2 cm, the coherence acceptance angle is the same as for the Fresnel regime.

2.6 Doppler effect and spectrum broadening

As mentioned above, the field scattered by the moving objects can be distinguished from the reference as its wavelength is modified by the Doppler effect. The frequency shift induced by scattering on an object moving at velocity \vec{v} is given by the formula:

$$\Delta\omega = (\vec{k}_s - \vec{k}_i) \cdot \vec{v} \quad (2.23)$$

It has been demonstrated in laser Doppler velocimetry, that the spectrum of an initially monochromatic beam scattered by the vessels of the retina is broadened, rather than just shifted (Fig. 2.5). This statistical effect is explained by the distribution of scattering particles velocity as well as variety of incidence angles. According to Bonner and Nossal [31], it is highly probable that, as RBC constitute a small part of the total number of particles in the human retina, light scattered by RBC has also been scattered - before or after - by static diffusers. This also accounts for the fact that laser Doppler flowmetry allows to image in-plane vessels which are seemingly perpendicular to the optical axis of the instrument.

All throughout this manuscript we will consider that moving RBC are the sole source of contrast in images obtained. This assumption is not entirely true as the surrounding tissue is also in constant movement, but its velocity is considerably lower, and hence can be neglected.

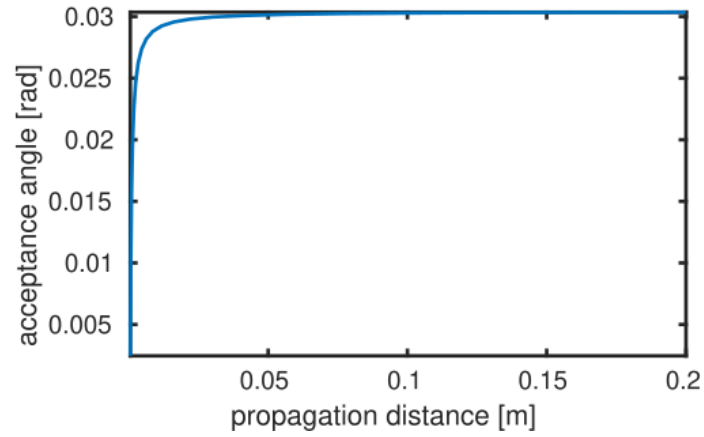
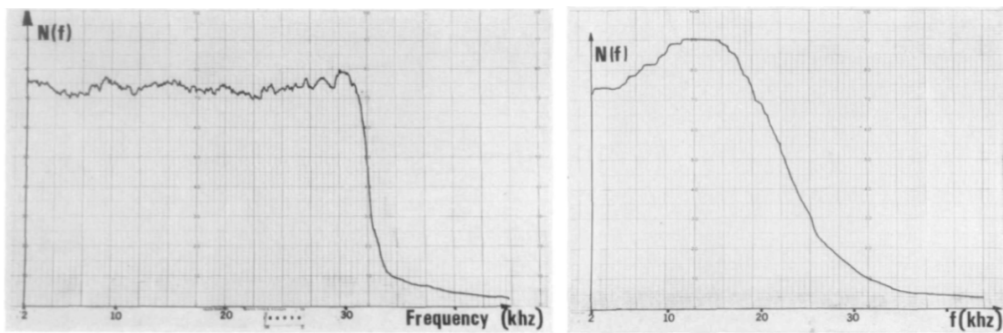


Figure 2.4: The plot of the maximal acceptance angle in function of the propagation distances for the angular spectrum representation.



(a) The power spectrum $N(f)$ of light scattered by a dilute suspension of polystyrene spheres in water flowing through a capillary tube. (b) The power spectrum $N(f)$ of light scattered by whole blood flowing through a capillary tube.

Figure 2.5: Figures adapted from [32]. A frequency shift distribution for a steady flow in tube with polystyrene spheres suspended in it 2.5a and for a blood flow in a capillary tube in vitro 2.5b

Chapter 3

Laser Doppler Holography

3.1 Introduction

In the recent years we have observed a strong development of holographic detection schemes in the field of retinal imaging with techniques such as full-field swept-source OCT, full-field time domain OCT or off-axis holographic line-field en-face OCT. Their common characteristic is that they allow direct or indirect encoding of the phase information about the scattered field. As a result, new possibilities - such as numerical offline processing - are opened. However, measurement of the phase requires stability during the acquisition time. In biological samples - such as the human eye - the time of phase stability is relatively short. As a result, the emergence of these techniques would not be possible without the apparition of ultra-fast, high resolution cameras.

Laser Doppler holography is a technique which employs a holographic detection scheme and combines it with Doppler measurements as a contrast agent. The advantages of using holographic detection are:

- separation of the cross terms of the interference and thus allowing the determination of the axial direction of the flow,
- numerical offline processing such as aberration correction (which will be discussed in depth in the following chapters),
- increase of the SNR thanks to the strong intensity of the reference arm which multiplies the sample signal.

The basic processing that enables image reconstruction consists of: field propagation to the focal plane, passing to the time frequencies domain (FFT) and integration in the chosen band. The first demonstration of results obtained in vivo on humans dates back to 2018 [33]. In this chapter, we will discuss the design and performances which characterizes LDH before the start of my thesis.

3.2 Optical setup

The optical setup of LDH for clinical use is based on the Mach-Zehnder interferometer depicted in Fig. 3.1. An infrared $\lambda = 785$ nm diode laser (Newport SWL-7513-H-P) is used as a source of illumination, which is split using a fibre coupler into 10% for the reference arm and 90% for the object arm. Both beams are collimated and polarized in orthogonal directions. The illumination beam is

directed towards the eye using a polarizing beam-splitter, which reflects polarized light to illuminate the retina and transmits the cross-polarized component present in the multiply scattered light returning from the eye. This configuration rejects specular reflections from the optical components or the cornea. Finally, this cross-polarized component is combined with the reference beam using a non-polarizing beam-splitter and directed toward two cameras used for detection. The first one is referred to as the slow CMOS camera (Ximea - xiQ, frame rate 80 Hz, 2048×2048 pixels, 8-bit pixel depth, pixel size $5.5 \mu\text{m}$), and is used for real-time monitoring and alignment of the subject. The second camera - the fast CMOS camera (Ametek - Phantom V2511, frame rate up to 75 kHz for a 512×512 format, quantum efficiency 40%, 12-bit pixel depth, pixel size $28 \mu\text{m}$) - is used for offline rendering of the videos, providing the dynamics of the blood flow. All of the components described above constitute the core of the optical setup, still to this day. The changes applied will be discussed in depth in the second part of the manuscript. The illumination beam in the configuration from 2018 was focused in front of the eye so that the light impinging on the retina was approximately collimated and covered an area between $3 - 6 \text{ mm}^2$ with constant exposure of 1.5 mW .

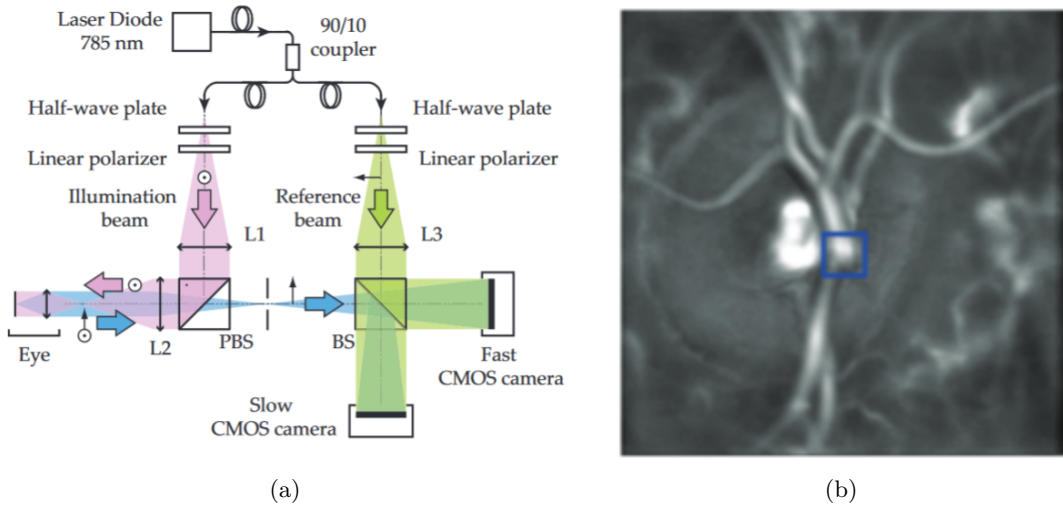


Figure 3.1: Figures adapted from [2]. (a) The optical setup of LDH. (b) Associated image obtained, centred on the optic nerve head. L1, L2, L3 denote lenses, BS and PBS stands for beam-splitter and polarizing beam splitter.

3.3 Digital image rendering

From the initial stream, a batch of N_t consecutive interferograms is extracted. The number N_t has to be chosen as a compromise between the SNR and temporal resolution. The frame rate of the resulting video will then be: $\text{fps} = f_s \times N_t$, where f_s stands for sampling frequency of the camera. The entire batch is numerically propagated using one of the methods described in Chapter: Digital Holography (Fig. 3.2). The propagation distance z is chosen by visual assessment as a plane in which the features are best resolved. Puyo et al. proposed applying a spatio-temporal filtering prior to the temporal Fourier analysis and Doppler broadening measurement allows to reject noise which can be caused by specular reflections, global movements of the tissue or camera jitter [34]. Let us

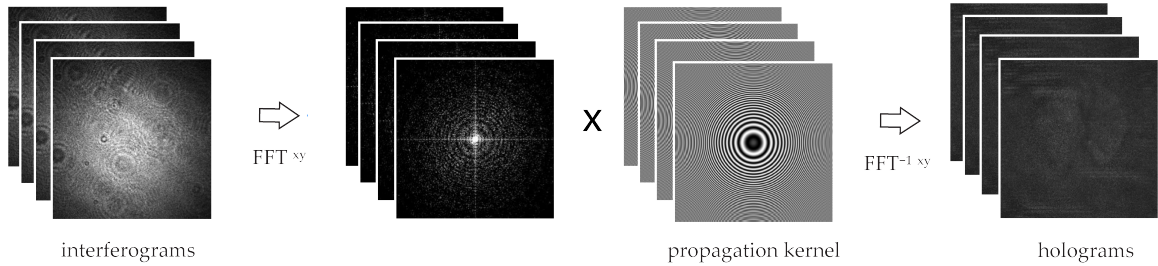


Figure 3.2: A diagram of the angular spectrum propagation algorithm.

consider a matrix A where each column represents a 2D image at a moment t_i . The size of matrix H is $N_x N_y \times N_t$. A singular values decomposition (SVD) of the matrix H can be written as:

$$H = U \Delta V^\dagger \quad (3.1)$$

where Δ is a diagonal matrix, with real, positive elements. To calculate the SVD one proceeds by calculating the covariance matrix COV of the matrix H , which is then diagonalized. This allows finding the matrix V present in the Eq. 3.1.

$$H * H^\dagger = COV = V * D * V^\dagger \quad (3.2)$$

Furthermore, the diagonal matrix D holds the same eigenvalues as the matrix Δ , although the dimensions of matrices differ. Unlike diagonalization, SVD can be applied to rectangular matrices. One can see this procedure as decomposition of the signal into patterns, whose covariance matrix is diagonal, which means that the spatio-temporal signals of the new basis are orthogonal. As a result, the eigenvalues represent auto-correlation values, which correspond to the energy contained in spatial pattern associated with one temporal and one spatial singular vector. It is expected that spatio-temporal patterns associated with the highest energies reveal the global movements of the tissue, as well as reflections or camera jitter [35]. In conclusion, SVD filtering consists in rejecting the patterns corresponding to the highest eigenvalues.

Finally, the FFT is calculated along the time direction of the filtered holograms. To quantify the Doppler broadening, the first and second moments of the spectrum are integrated over chosen frequency bands. The final images are calculated by summing or subtracting moments for the positive and negative parts of the spectrum.

$$M_0^\pm = \int_{\pm f_2}^{\pm f_1} S(x, y, f) df \quad (3.3)$$

$$M_1^\pm = \int_{\pm f_2}^{\pm f_1} S(x, y, f) f df \quad (3.4)$$

The parameters f_1, f_2 will have a crucial impact on the results. Fig. 3.3 illustrates images obtained by integrating chosen bands of the spectrum (with and without prior SVD filtering). One can see that the lowest frequencies, up to 0.2 kHz, are dominated by the image of the reference arm. The 0.2 - 1 kHz band contains an “inverse contrast” image (where vessels appear darker than the background) of the largest vessels where the blood flow velocity is the highest. In the range of 1 - 3 kHz, we obtain an image that contains the previously inversely contrasted largest vessels, but this time appearing thinner (the velocity in the centre of the vessels is the highest) as well as correctly

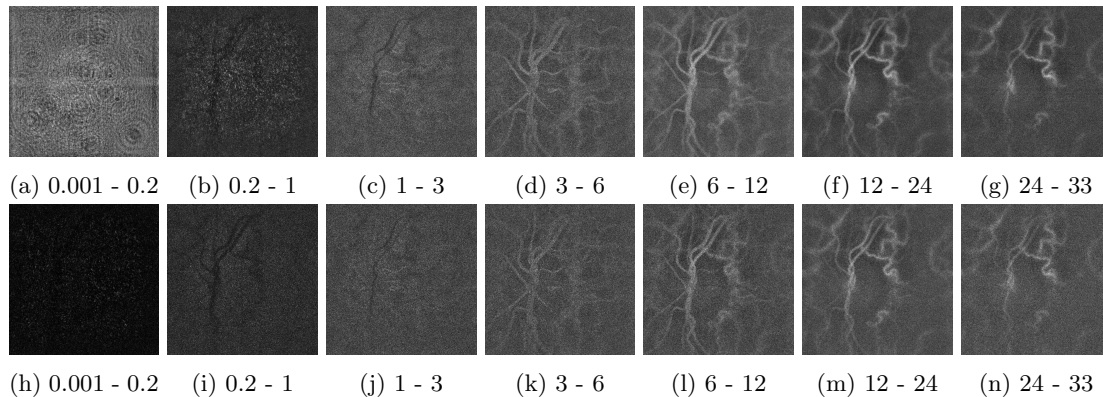


Figure 3.3: Images obtained from hologram integration in chosen bands of frequency. Upper line without prior SVD filtering, lower with.

contrasted smaller vessels (particularly visible around the ONH) [36]. The 3 - 6 kHz frequency band represents all the vessels in correct contrast, but they all appear quite flat—the intensity of the vessels is homogeneous regardless of their size. In the following frequency bands, we can see that vessels with too low blood flow will gradually disappear, and only areas with the highest velocity will remain. As a result, integrating frames between 3 - 33 kHz gives an impression of the vessels’ 3D form.

The last step of the image rendering process is the flat field correction, which consists in dividing the image by the same image with a Gaussian filter applied. The parameter of “blur” describing width of the Gaussian filter is chosen experimentally. We ensure that the total energy of the image remains constant before and after division. The video obtained can also be registered to compensate for eye movement. Respective shifts of the images are measured using a cross-correlation function.

3.3.1 Doppler broadening measurements and sampling frequency

The sampling frequency of the camera used will modify the images obtained, although it should be kept in mind that the roles of sampling and filtering frequencies are not the same. In principle, to respect the Nyquist theorem, we should make sure that the sampling frequency is at least twice the largest difference between the reference and sample arm frequencies. However, in reality, the frequency mismatch follows a distribution with long but quickly decreasing tails. We will consider that if the sampling rate is considerably higher than the variance of the frequency distribution recorded, the spectrum is correctly sampled. However, if the sampling rate is lower, frequency wrapping can corrupt the signal detected. As represented in Fig. 3.4, the highest frequencies can get aliased - i.e, shifted to the lower negative frequency.

3.4 Blood flow analysis in retinal and choroidal vessels of the human eye fundus

One of the principal applications of LDH is to enable the characterization of blood flow dynamics in the human retina. A first analysis of the measurements taken with LDH on human subject was reported by Leo Puyo et al. in 2018 [33], and the results obtained will be discussed in the following

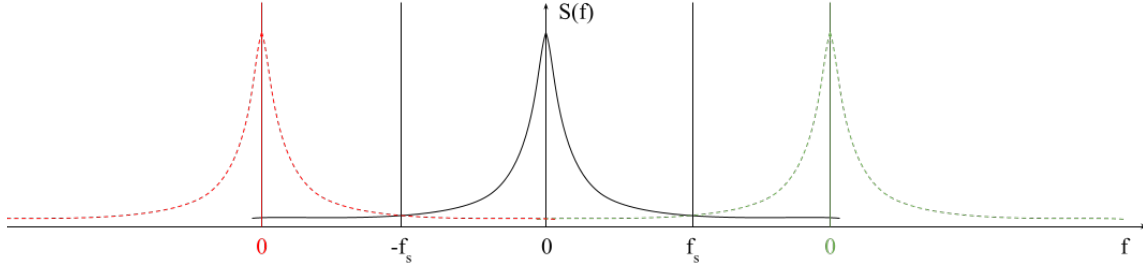


Figure 3.4: A schematic representation of the effect undersampling has on spectrum measured

paragraphs.

3.4.1 Signal analysis for the retinal vessels

Retinal vessels are considered. The videos studied are centered on the optic nerve head of the volunteer. A comparison is made between the signal calculated using M_0 (referred to as power Doppler), which is interpreted as holding information about the blood volume, and f_{mean} calculated as follows:

$$f_{mean}(x, y, t_n) = \frac{M_1(x, y, t_n)}{M_0(x, y, t_n)} \quad (3.5)$$

This equation yields the average Doppler frequency shift and thus is supposed to assess the average velocity. M_0 and f_{mean} are integrated between different frequency ranges, typically chosen as $[10 - f_s/2 \text{ kHz}]$ and $[0.5 - f_s/2]$ respectively. Both images reveal retinal vessels, yet they provide different temporal signatures (Fig. 3.5). The signals are extracted from three regions of interest (ROI): retinal artery (RA), retinal vein (RV), and background (B). The authors of the paper conclude that the M_0 signal should be chosen over f_{mean} for waveform analysis as it is less corrupted by noise.

We can immediately see that the B trace is pulsing and similar in form to the signal from other areas. This suggests that contributions from unresolved vessels in the background are important. To validate this hypothesis, an additional comparison is made between the raw signal and the spatial average subtracted signal, which can be written as $M_0 = M_0 - \langle M_0 \rangle_{xy}$ and $f_{mean} = f_{mean} - \langle f_{mean} \rangle_{xy}$. It is expected that this subtraction allows distinguishing the respective contributions to the Doppler broadening. After the subtraction of the averaged signal, the signal in the arteries changes in terms of absolute values but remains the same in terms of the waveform shape. On the other hand, the signal in veins and in the background is considerably changed.

Veins are characterized by an oscillation with a period corresponding to the cardiac cycle. The minimum of the venous signal coincides with the maximum of artery signal. A de-phasing between the two is studied to verify if this feature is not an artefact induced by the subtraction of the average signal. If that were the case, the minimum of the vein signal would rather coincide with the maximum of the background signal, which is slightly delayed with respect to the artery signal. However, the strict correlation with the arterial signal suggests that the origin of pulsation is physiological.

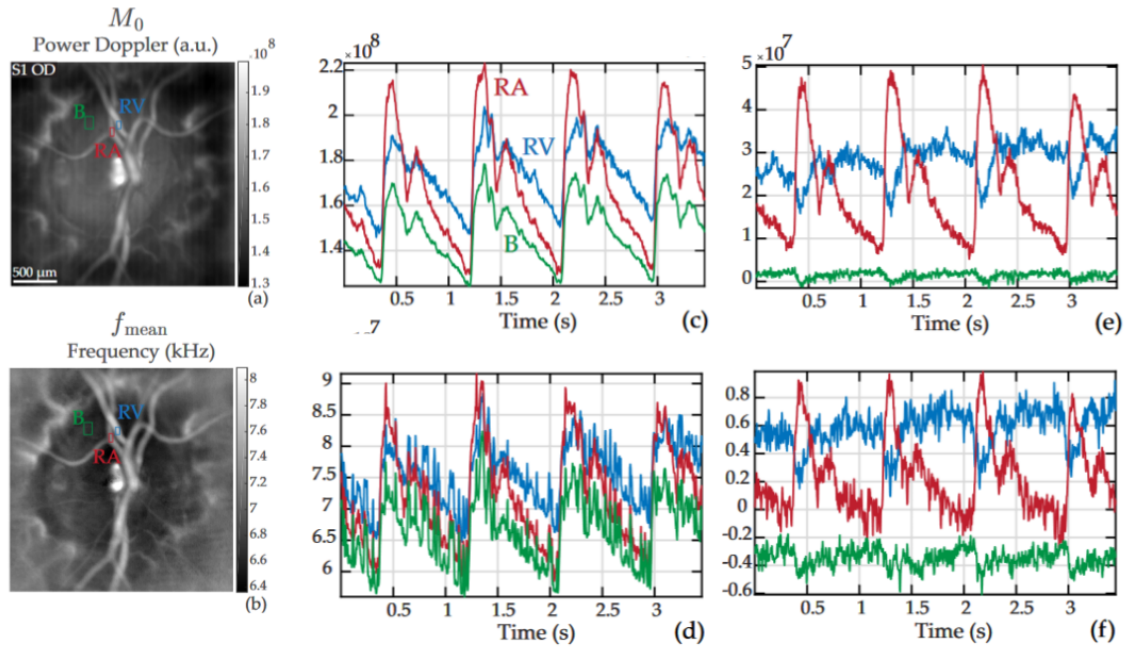


Figure 3.5: Figure adapted from [37]. A comparison between M_0 (top) and f_{mean} (bottom) signals in three ROI: retinal artery (RA), retinal vein (RV) and background. Two types of processing are considered: taking directly the values measured (c, d) and subtracting the signal averaged over the entire field of view is from the initial values in ROI (e, f).

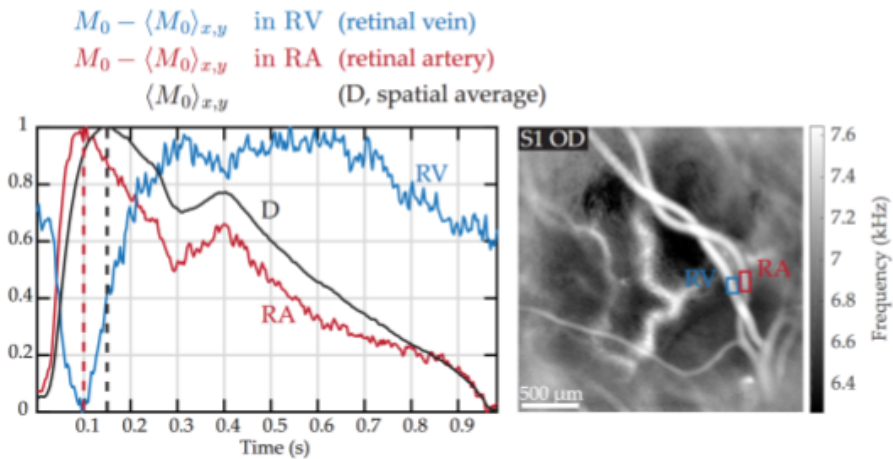


Figure 3.6: Figure adapted from [37]. Graph representing normalised signals in artery, vein and background. The dashed lines correspond to the position of peak in artery and background traces, revealing that the minimum in the vein signal is correlated to the peak in the artery signal.

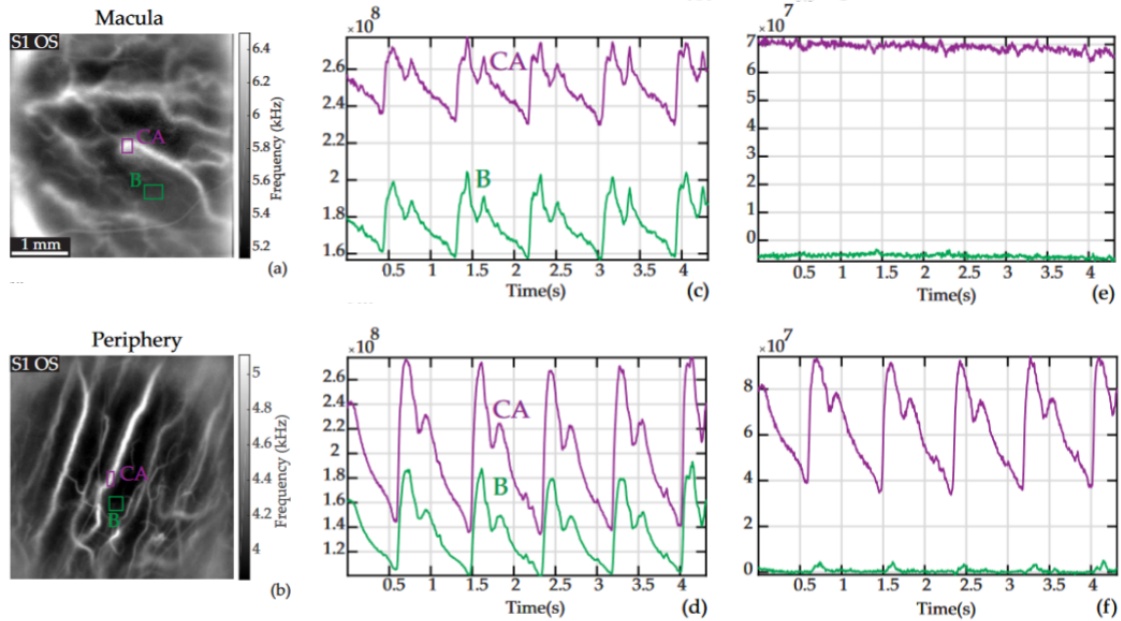


Figure 3.7: Figure adapted from [37]. Power Doppler signals from choroidal artery in macula (a, c, d) and periphery (b, d, f), as well as neighbouring backgrounds are calculated. The raw signals (c, d) and with spatial average subtracted (e, f) are considered. The comparison suggests the density of photoreceptors has an impact on LDH measurements in the choroid.

3.4.2 Signal analysis for the choroidal arteries

A separate analysis is made for the signal in the choroid. On the one hand, blood flow velocities in this layer are expected to be much higher than those in the retina. On the other hand, the choroid lies underneath RPE layer, which is a highly scattering structure, resulting in the "blurring" of the detected signal. As a result, the analysis of blood flow dynamics is more difficult in the choroid than in the retina. To assess the impact that the density of photoreceptors can have on blood flow dynamics, two regions of the eye fundus were studied: the macula, where the density of photoreceptors is the highest, and the periphery, where they are more sparse. The results were analyzed similarly to those from the retina. The absolute signals were measured in the choroidal arteries (CA) and in the background (B), an area free of distinctive vessels. Then, the same signals were plotted with the subtracted spatial average.

In the case of the periphery, the results are similar to those obtained for the retinal vessels. The subtraction of the signal averaged across the field of view alleviates the time dependency of the B signal, yet the waveform shape in the CA remains visible. However, in the macula, the subtraction seems to alleviate the pulsatile character of the signal. This result can be explained by the presence of a large artery in the lower-left corner of the image, whose signal can be very strong and thus dominates the spatial average.

To conclude, it is possible to retrieve information about the blood flow dynamics in the choroid. However, the analysis of the signal is complex due to the non-trivial effect that the scattering structures overlaying the choroid have on Doppler broadening. One conclusion that can be made with certainty is that the blood velocities in the choroid are significantly higher than those in the

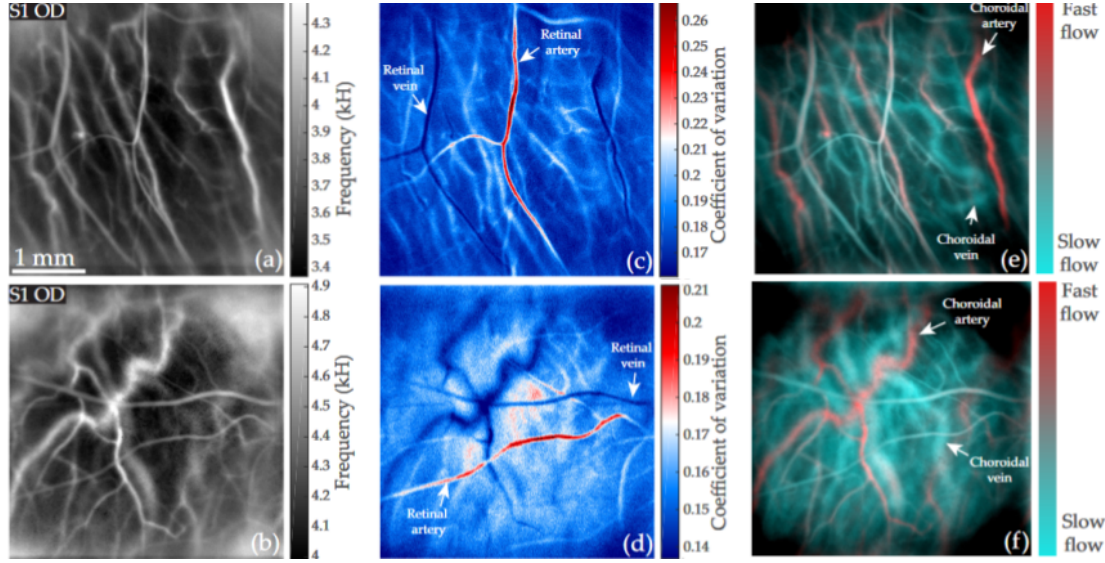


Figure 3.8: Figure adapted from [37]. Comparison of power Doppler (a, b), coefficient of variation (c,d) and colour composite (e,f) images in two areas (top, bottom) of the eye fundus. The interpretation of these images allows distinguishing veins from arteries in both choroid and retina.

retina, which is consistent with what we know about the physiology of the eye fundus. This, however, means that the Doppler broadening induced can be above 30 kHz, and thus correct measurements require the use of ultra-high frame-rate cameras.

3.4.3 Characterization of the Doppler waveform

As mentioned in the Chapter: Human Eye, the role of the vascular system is to transport blood and buffer the intermittent variations in pressure, converting them into a steadier flow. This is achieved by the elastic properties of the larger arteries and by the resistance at the level of arterioles situated at the ends of vascular trees. The blood flow velocity is limited by friction on the vessel walls, blood viscosity, and the total cross-section of the arterial bed. All of these characteristics impact the shape of the wavefront and can hence be deduced from it. Puyo et al. proposed the use of two metrics. The first one is the Pourcelot or resistivity index (RI), defined as:

$$RI_g(x, y) = \frac{g(x, y, t_{sys}) - g(x, y, t_{diast})}{g(x, y, t_{sys})} \quad (3.6)$$

where g is the signal measured, and t_{sys} , t_{diast} correspond to the times of systole and diastole, respectively. The index ranges between 0 and 1. Increase of arterioles resistivity considerably lowers the blood velocity during diastole, when the pumping pressure is too low to counterbalance the resistance. As a result increased arterioles resistivity increases Pourcelot index. However, it must be noted that upstream arterial flow influences the arterial waveform in the retina and thus its variations can corrupt the results obtained. As a result, the two are coupled and cannot be directly deduced from the resistivity index.

The second metric, the coefficient of variation, is calculated as follows:

$$CV_g(x, y) = \frac{\sigma_g(x, y)}{\mu_g(x, y)} \quad (3.7)$$

where $\sigma_g(x, y)$ and $\mu_g(x, y)$ denote the standard deviation and the mean value, respectively. The CV index, like the RI, aims at revealing the areas where the depth of signal modulation is the greatest.

3.4.4 Vessel identification

The metrics described in the section above are mainly used to identify pathological cases where the blood flow is abnormal. However, they can also be employed to identify the vessels. In Figure 3.8, two parts of the retina are represented in power Doppler (a, b), CV (c, d), and colour composite images (e, f). The latter is obtained by splitting the signal at low and high frequencies into blue and red channels of an RGB image. In power Doppler images, all vessels appear white. In the CV maps, retinal arteries appear strong red, whereas the veins are dark blue. However, the choroidal arteries are confused with retinal veins. Finally, in the colour composite images, the choroidal arteries appear red and can be distinguished from the retinal veins due to their higher Doppler broadening. In conclusion, the proposed processing allows identifying retinal arteries, veins, and choroidal arteries.

3.5 Image of the choroid vasculature

LDH has proven to be a valuable instrument for the study of the choroid vasculature. A comparative analysis between the stitched LDH images and those obtained with commercially available devices was conducted by Puyo et al. [38]. Measurements were taken on the same subject. The first comparison is made with panoramas obtained using ICG-A, a contrast agent-based technique typically used for choroid imaging, and SLO, which reveals only retinal vessels, thus allowing discrimination of which structures imaged with LDH belong to the choroid. The first observation is that contrasts obtained with ICG-A and LDH are very different. For example, choroidal arteries lying below the macula are barely visible with ICG-A, yet they appear very bright on LDH images. This can be explained by the fact that contrast in ICG-A images does not directly depend on the velocity of blood flow, and signal attenuation is related to the density of scattering structures covering the area of interest. On the other hand, in LDH, frequency filtering partially alleviates this effect; however, it makes the detection of vessels with low blood flows, such as macular veins, more difficult.

Accurate information about the anatomy of the tissues can be retrieved from 3D reconstruction of SS-OCT scans and B-scans from SD-OCT. Two distinctive planes are considered: deep choroid and the sclera. Comparison with previously studied images validates the previous observation that ICG-A and LDH reveal different vessels. Moreover, OCTs allow identification of the SPCAs (short posterior ciliary arteries) penetrating the sclera, which can also be visible with LDH.

In conclusion, all three techniques for imaging the choroid have important advantages and drawbacks. Firstly, ICG-A is very valuable as it allows "tracking" the contrast agent travelling through the blood circuit, and consequently distinguishes arteries from veins. Moreover, it is the sole device that can reveal leakage from the vessels. However, it is an invasive technique, potentially dangerous for patients, and the examination itself requires the presence of two specialists and is time-consuming and complicated. OCT has the advantage of providing complete information about the structure of the eye with axial sectioning, which is lacking in other devices. Its two main disadvantages are that it

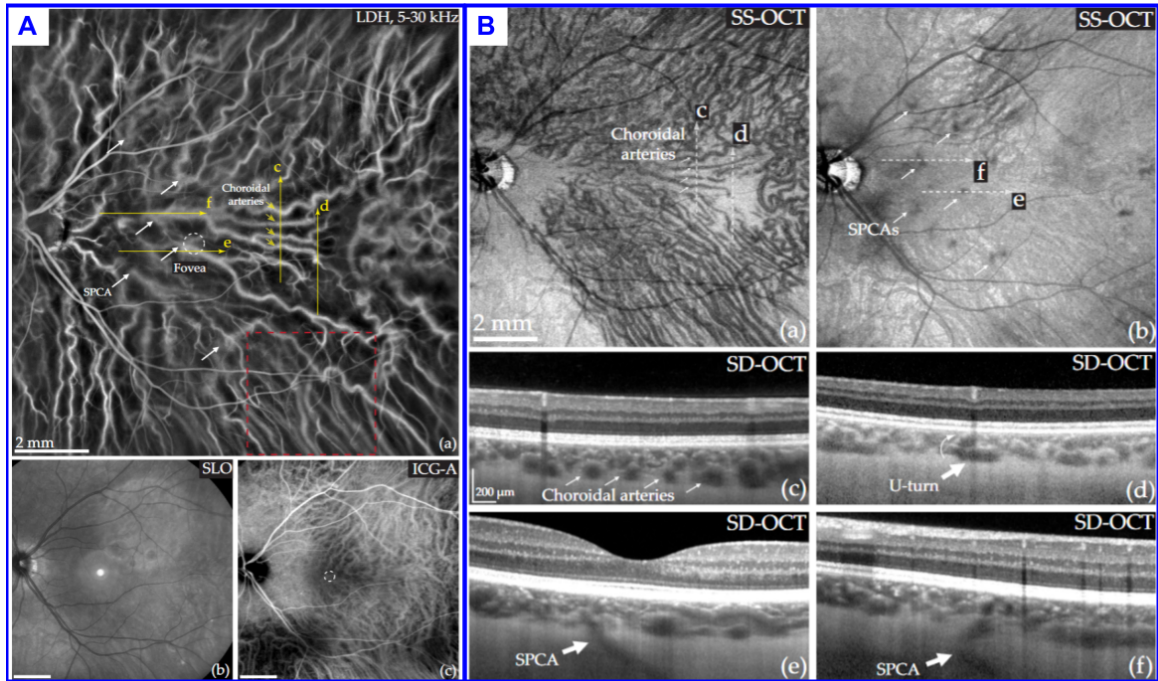


Figure 3.9: Figure adapted from [38]. The wide-field image of the choroid obtained with LDH (A.a) was compared first with SLO (A.b) and ICG-A (A.c). Secondly, the images were compared with the SS-OC C-scans at deep choroid (B.a) and sclera (B.b) levels, and SD-OCT B-scans (B.(c-f)) at four positions which are indicated at the images above.

does not give any information about blood flow dynamics and that in the volumes obtained, arteries and veins are indistinguishable. Finally, LDH can provide some insight into blood flow dynamics and allows primary identification of arteries and veins (although the success rate is not 100%). The main issue with this technique is that the results depend on a subtle analysis of the spectrum, and thus do not seem fully reliable. However, as Puyo et al. suggest in article [38], the information retrieved from LDH combined with OCT can provide important insights into the physiology of the choroid.

3.6 Passive retinal Arteries Elastography

LDH was equally used to extract information about the mechanical properties of retinal arteries. G. Laloy-Borgna and S. Catheline demonstrated the existence of an asymmetrical wave propagating in the vessels with a velocity considerably lower than that of the symmetrical wave, making it detectable using LDH signals [39].

The velocity can be estimated indirectly for each frequency by measuring the wavelength. The signal along a chosen artery is extracted, with each point corresponding to a signal averaged over the section of the vessel. Subsequently, the Fourier transform is performed along the temporal direction for each point of the curve. The amplitude of the signal for each frequency is set to 1—only the phase is considered. This allows "whitening" of the spectrum and normalizing it along the artery. Then, for each frequency, the monochromatic focal spot can be calculated using the following formula:

$$C_f(r) = \left\langle \cos \left(\arg \left(\hat{\phi}_s(f) \right) - \arg \left(\hat{\phi}_{s+r}(f) \right) \right) \right\rangle_s, \quad (3.8)$$

where $\arg \left(\hat{\phi}_s(f) \right)$ is a phase of the signal for point with curvilinear coordinate s at frequency f . The cosine functions are averaged over all points along the curve separated by r . The wavelength can be measured by fitting a sinusoid to the central peak of C_f (Fig. 3.10). If this procedure is repeated for multiple frequencies, we can retrieve the dispersion curve for the chosen artery. The slope of the curve obtained corresponds to the group velocity along the artery. Alternatively, the group velocity can be estimated using a more classical approach—by following the wavefront displacement over time. This is achieved by calculating the cross-correlation functions according to the formula:

$$\mathcal{T} \circ \mathcal{F}(\Delta x, \Delta t) = \left\langle \phi_{x_0}(t) \underset{\Delta t}{\oplus} \phi_{x_0+\Delta x}(t) \right\rangle_{x_0} \quad (3.9)$$

In the presence of dispersion, the correlation in distance-time space will present inclined fringes. Measurement of their slope allows quantification of the wavefront velocity.

The formula describing pulse wave velocity (PWV) was first proposed by Moens-Korteweg at the end of the 19th century and then accepted by the community. The vessel is modelled as a tube of diameter d and wall thickness h with fluid inside it, but the soft tissue surrounding the vessel is not taken into account.

$$PWV = \sqrt{\frac{h}{d}} \sqrt{c_s} \quad (3.10)$$

This formula is generally used for waves propagating in large vessels such as the aorta, but it was never applied to describe the elasticity of retinal vessels, as it yields unrealistic values of velocity for the bending waves propagating in soft tissue. To overcome this issue, Laloy-Borgna and Catheline applied the model proposed in 1959 by Gazis [40] and then calculated numerically among others by Nishino et al. in 2001 [41] to find the relation between phase velocity and the shear velocity $c_s = \sqrt{\frac{\mu}{\rho}}$, where μ and ρ stand for shear modulus and specific mass, respectively, for two modes predicted:

$$v_{F(1,1)} \cong \sqrt{\frac{\pi f d c_s}{\sqrt{3}}}, \quad v_{L(0,1)} \cong \sqrt{3} c_s \quad (3.11)$$

where f is the frequency and d is the diameter of the vessel. This model predicts the existence of both modes mentioned above and the dispersive character of the bending waves. To verify the agreement between the model and measurements conducted with LDH, the velocity was plotted against the product of $f \times d$ on a log-log scale for nine different arteries of one volunteer. The diameter was estimated directly from the laser Doppler measurements. A linear fit to the total of points has a slope of 0.84.

As discussed by Gabrielle Laloy-Borgna in her thesis, both theories remain insufficient for an exhaustive description of wave propagation in retinal vessels. Moreover, it is noted that LDH does not measure the displacement of vessels but the impact of movement on the effective velocity of red blood cells, which is an indirect measurement of the wavelength. It is also argued that other techniques, such as angiography, already in clinical use, could be adapted for similar measurements.

One limitation of the method is that it does not allow measuring the longitudinal wave due to the low frame rate (38 Hz) and field of view (5.3 mm) of the video treated.

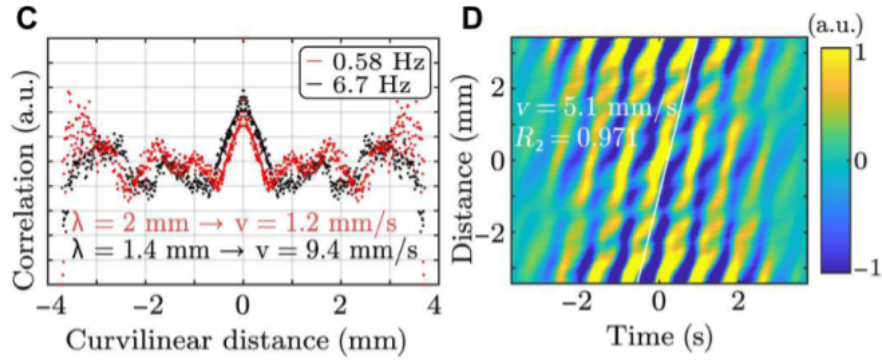


Figure 3.10: Figure adapted from [42]. The phase velocity can be calculated indirectly by measurement of wavelength using passive spectroscopy for different frequencies using formula in Eq. 3.8 (left). A completely independent measurement of group velocity can be made from the signal without decomposing it spectrally. It amounts to estimating the time of flight using the formula in Eq. 3.9. The velocity is given by the slope of the fringes in spatio-temporal space (right).

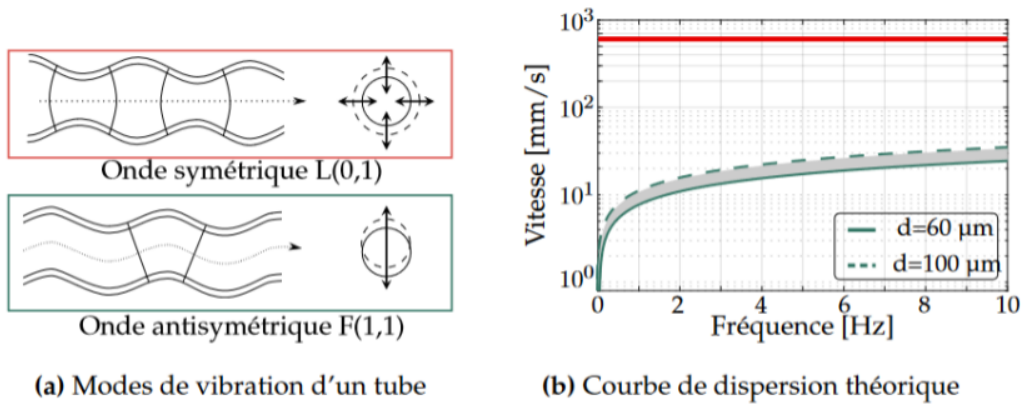
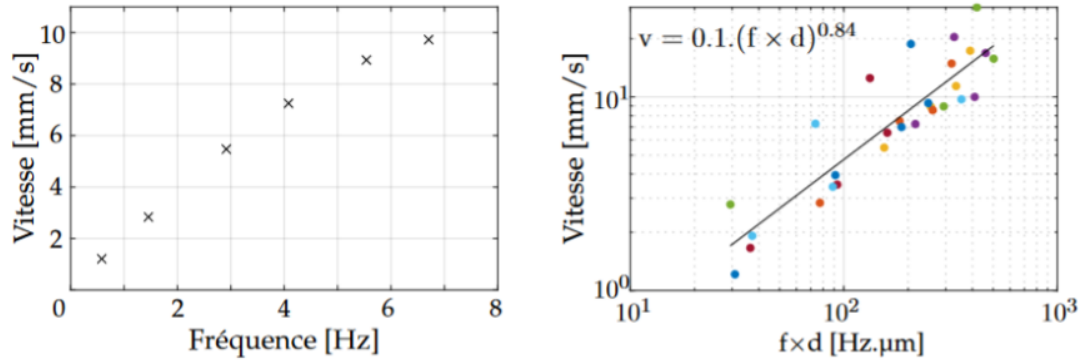


Figure 3.11: Figure adapted from [42]. A model proposed by Gasiz for guided waves in a tube predicts the existence of two modes: symmetrical (L(0,1)) and anti-symmetrical (F(1,1)) (left). The L(0,1) is non-dispersive and velocity associated is in order of hundreds of mm/s. The F(1,1) is dispersive and in the range of small frequencies the velocities associated correspond to several mm/s, and thus are 100 times smaller than for the symmetrical mode (right).



(a) Courbe de dispersion dans une artère (b) Sur plusieurs artères d'un même volontaire

Figure 3.12: Figure adapted from [42]. The dispersion curve of the anti-symmetrical mode measured for one artery (left). The phase velocity measured for multiple arteries plotted in function of frequency multiplied by the vessel diameter in the log-log scale (right). The linear fit is used to evaluate the accordance of the measurements with the model.

3.7 Limitations and unresolved problems of LDH

As we have seen in the sections above, LDH is a promising technique for the visualization and measurement of blood flow in the eye fundus. However, deploying this technique in clinical use requires further improvements in the accuracy of the data it provides. So far, the measurement of blood flow remains qualitative, which is a serious drawback. It is especially difficult to interpret the signal from the choroid, even though LDH reveals the velocity distribution in the choroid, which can provide valuable information.

LDH measurements have been taken, to date, on around 600 volunteers. The robustness and versatility of the method are very promising, and it is crucial for clinical studies that all of these data can be exploited. One issue worth addressing concerns ocular aberrations present in a significant fraction of subjects, which could be compensated by adaptive optics or a numerical aberration correction strategy.

Another aspect that limits the applicability of LDH is the relatively small field of view of a single image compared with clinical devices. This means that for some applications, it is necessary to stitch multiple videos, which has been performed case-by-case. However, this makes the acquisition longer and more complicated, as the overlap between the imaged areas must be sufficient for correct alignment.

Finally, it must be ensured that every step of the proposed processing can be automated. In the current state, extracting blood flow profiles in different areas of interest has been performed manually. The size of the areas of interest has been small compared to the totality of data present in the video. Proper extraction of all acquired information requires proposing a treatment strategy. The aim of this thesis is to resolve existing problems of LDH, alleviate some of the existing limitations of the technique and bring it closer to clinical use.

Part II
Results

Chapter 1

Wide-field imaging

1.1 Introduction

Upon my arrival in the team of Michael Atlan, the LDH was already a functioning technique. The only modifications proposed for the optical setup aimed at extending the field of view at the retina. A detailed description of the new optical setup as well as its advantages were thoroughly described in the paper which was preprinted on Arxiv.

1.2 Article

Diffuse laser illumination for Maxwellian view Doppler holography of the retina

Zofia Bratasz,¹ Olivier Martinache,¹ Yohan Blazy,¹ Angèle Denis,¹ Coline Auffret,¹ Jean-Pierre Huignard,¹ Ethan Rossi,² Jay Chhablani,² José-Alain Sahel,² Sophie Bonnin,³ Rabih Hage,³ Patricia Koskas,³ Damien Gatinel,³ Catherine Vignal,³ Amélie Yavchitz,³ Ramin Tadayoni,³ Vivien Vasseur,³ Claire Ducloux,⁴ Manon Ortoli,⁴ Marvin Tordjman,⁴ Sarah Tick,⁴ Sarah Mrejen,⁴ Michel Paques,⁴ and Michael Atlan¹

¹*Centre National de la Recherche Scientifique (CNRS) UMR 7587, Institut Langevin. Paris Sciences et Lettres (PSL) University, Sorbonne Université (SU). École Supérieure de Physique et de Chimie Industrielles (ESPCI) Paris - 1 rue Jussieu. 75005 Paris. France*

²*University of Pittsburgh, 203 Lothrop Street, Suite 800, Pittsburgh, PA, 15213, USA.*

³*Rothschild Ophthalmologic Foundation, Clinical studies department, 75019, Paris, France*

⁴*Quinze-Vingts National Eye Hospital, DHU Sight Restore, Sorbonne Université, INSERM-DGOS CIC 1423, CNRS, 28 rue de Charenton, Paris, 75012, France.*

(Dated: December 29, 2022)

We describe the advantages of diffuse illumination in laser holography for ophthalmology. The presence of a diffusing element introduces an angular diversity of the optical radiation and reduces its spatial coherence, which spreads out the energy distribution of the illumination beam in the focal plane of the eyepiece. The field of view of digitally computed retinal images can easily be increased as the eyepiece can be moved closer to the cornea to obtain a Maxwellian view of the retina without compromising ocular safety. Compliance with American and European safety standards for ophthalmic devices is more easily obtained by preventing the presence of a laser hot spot observed in front of the cornea in the absence of a scattering element. Diffuse laser illumination does not introduce any adverse effects on digitally computed laser Doppler images.

I. INTRODUCTION

Optical holography methods increasingly leverage the use of laser radiation for coherent, phase-resolved computational imaging in ophthalmology from camera recordings of interference patterns of the light backscattered by the retina beating against a separate reference beam. This imaging scheme is highly suited to the computation of local optical Doppler contrasts [1] and permits imaging of both the anterior and posterior segments of the eye from the same recorded data set of raw interferograms [2]. Yet for the particular case of retinal imaging, extending the field of view of the computed images used to be avoided to prevent high local irradiance of the cornea beyond permissible laser exposure recommendations from American and European ophthalmic safety norms. In previous work, the eye was typically illuminated with 2 mW or less of constant exposure to near infrared laser light focused in front of the cornea, at a distance either equal to or greater than the eye focal length, depending on the desired field of view [2]. When focusing exactly in the eye front focal plane, the obtained field of view has, at most, a similar extension for the iris and retina. The iris acts as an image field diaphragm instead of an aperture stop, which prevents wide-angle imaging. For instance, the construction of a full image of the posterior pole of the retina (the portion centered on the macula that includes the optic nerve) required image rendering and stitching from numerous sequential acquisitions [3].

In this letter, we report on the use of diffuse laser illu-

mination to increase the field of view of digital holography up to a Maxwellian view of the retina, which consists in illuminating and collecting light from a large retinal area by a converging beam focused near the eye's nodal point, approximately 17 mm in front of the retina [4]. The proposed optical arrangement avoids the need for eye dilation for wide-field holographic imaging of the retina.

II. EXPERIMENTAL SETUP

The experimental setup is based on a Mach-Zehnder inline interferometer (Fig. 1). The near-infrared radiation from a diode laser (Thorlabs FPV852P, wavelength : $\lambda = 852$ nm, model 40750) is split 10% - 90% respectively into linearly-polarized reference and illumination arms, emerging from polarization-maintaining fibers (Thorlabs PM780-HP, numerical aperture : $NA \sim 0.12$). The illumination beam passes through an engineered diffuser (Thorlabs ED1-C20-MD SM1-Threaded Mount, diameter : 1", 20° circle tophat engineered diffuser) and an eyepiece made of two biconvex lenses of 60 mm focal length each, with an effective focal length of ~ 33 mm. Two cameras are used to record interferograms of the cross-polarized backscattered light component with respect to illumination. One is used for real-time preview (Adimec Quartz Q-2HFW-Hm/CXP-6-0.5 camera, pixel pitch : $12 \mu\text{m}$), and another one is used for offline image rendering (Ametek Phantom V2012, frame rate: 35 kHz, pixel pitch : $d = 28 \mu\text{m}$, frame size : $N_x \times N_y = 768 \times 768$ pixels). The latter is used for all the interference pattern measurements used for image rendering. The retina of

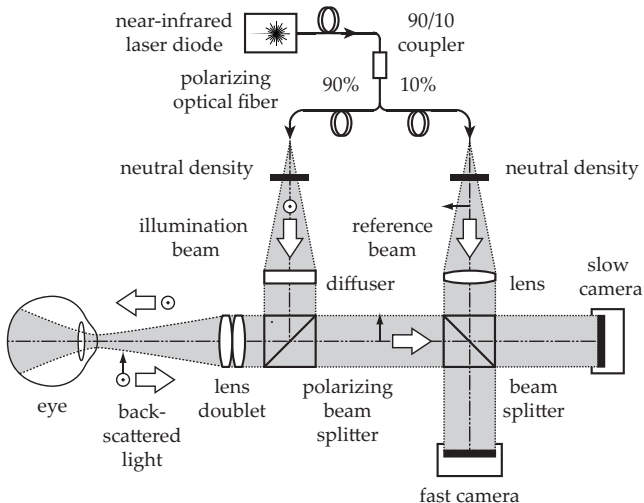


FIG. 1. Sketch of the optical configuration. An inline Mach-Zehnder near-infrared laser interferometer mixes the light backscattered by the eye fundus of a volunteer with a separate reference beam. Two cameras are set to record output optical interference patterns. The most significant difference with previously reported arrangement [1] is the presence of an optical diffuser that scatters the illumination beam. The diffuser-to-eyepiece center distance is ~ 100 mm.

a volunteer is illuminated with a continuous-wave laser beam focused through the eyepiece in three distinct layouts sketched in Fig. 2 :

- the illumination beam was focused at the natural focus point of the eye (Fig. 2(a)), in the absence of diffuser.
- the illumination beam waist was homogeneously spread by introduction of a diffuser. No change of relative position between the cornea and the lenses of the eyepiece was made (Fig. 2(c)),
- the cornea-to-eyepiece distance was reduced in the presence of the diffuser in order to increase the field of view (Fig. 2(e)).

Informed consent was obtained from the subject, experimental procedures adhered to the tenets of the Declaration of Helsinki, study authorization was obtained from the appropriate local ethics review boards - Personal Protection Committees (CPP Sud-Est III: 2019-021B) and National Agency for the Safety of Medicines and Health Products (ANSM No. IRDCB : 2019-A00942-55); the clinical trial was registered under the reference NCT04129021. The patient positioning was monitored by real-time computation and visualization of clutter-free inline digital holograms of the eye fundus from an input stream of 16-bit, 1024-by-1024-pixel interferograms recorded at 800 frames per second with the Adimec Quartz camera. This was done by Fresnel transformation and principal component analysis of stacks of 64 consec-

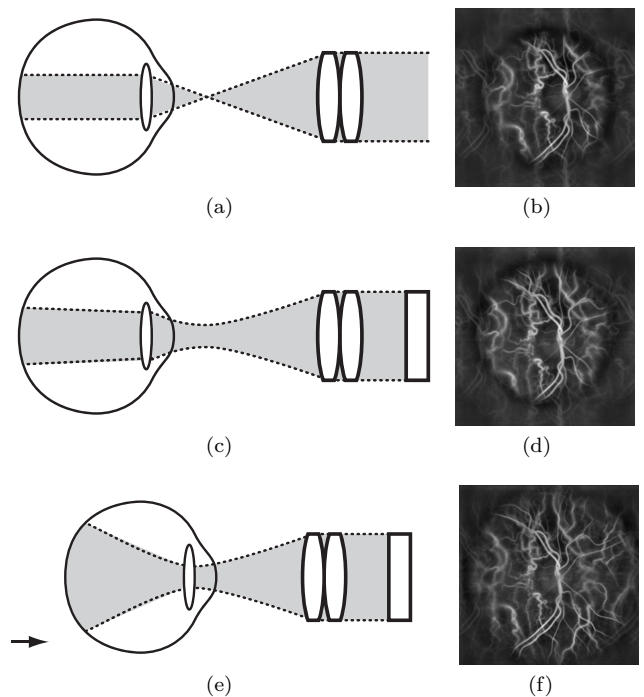


FIG. 2. When the diffuser is not present (Fig. 2(a)), a hot spot (high local optical power density, narrow beam waist) is created at the laser focus in front of the cornea, and the iris acts as an image field diaphragm (Fig. 2(b)). When the diffuser is present (Fig. 2(c)), the input beam waist is large enough and spatially homogeneous to prevent any security hazard. This configuration offers the same field-of-view (Fig. 2(d) vs. Fig. 2(b)). The cornea of the patient's eye can be positioned in the focal region of the illumination beam (Fig. 2(e)), which increases the field of view (Fig. 2(f)) and the iris no longer acts as a field diaphragm.

utive holograms [5], with the digital hologram streaming software [holovibes](#).

III. OPTICAL CONFIGURATION. INTERFERENCE PATTERN MEASUREMENT

Fig. 4 illustrates the optical configuration used for interference pattern measurement, from which image rendering is made. The focal length of one imaging lens is 60 mm (Thorlabs LB1723-B; N-BK7 bi-convex lens, diameter : 2", $f = 60.0$ mm, Anti-reflective coating: 650-1050 nm). The doublet has a focal length of $f' \sim 33$ mm, for a distance between its composing lenses of about 1 cm, according to Gullstrand's formula. The optical conjugate of the sensor plane is set in front of the cornea, at a distance ~ 33 mm from the center of the doublet. At this distance, the sensor-to-cornea magnification ratio is $M = 33/280 \sim 0.118$. To calculate the sensor to retina magnification ratio of the digitally rendered image, the optical system of the eye must be considered.

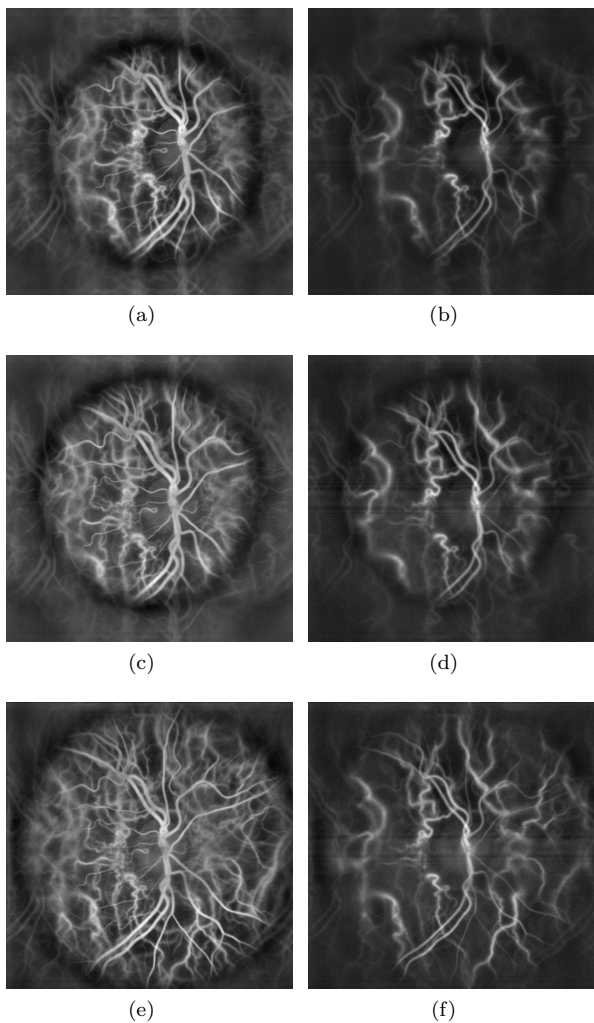


FIG. 3. Doppler fundus images from the broad fluctuation frequency band between 2 kHz and 17 kHz (left column) and from the high frequency band from 12 kHz to 17 kHz (right column). These images were computed from raw interferograms acquired in the three layouts of Fig. 2. Top row images (a,b) were obtained without diffuser, with the configuration sketched in Fig. 2(a). Center row images (c,d) were obtained from diffuse illumination, with the configuration sketched in Fig. 2(c). The cornea-to-eyepiece distance is the same as the one used for obtaining (a,b). This configuration offers approximately the same field-of-view as Fig. 2(a). Bottom row images (e,f) were obtained from diffuse illumination, with the configuration sketched in Fig. 2(e), in which the cornea of the patient’s eye was positioned in the focal region of the diffuse illumination beam to increase the field of view.

In the thin lens approximation (first-order properties of the optical system of the eye), light rays passing close to the optical center are not deflected. The sensor to retina magnification ratio of the digitally rendered image M' can therefore be estimated. For an average axial length of the eye of 25 mm, $M' = (33 + 25)/280 \sim 0.207$. The pixel pitch of the rendered image with the angular spec-

trum propagation method for numerical reconstruction distances $z < N_x d^2/\lambda \simeq 0.71$ m from the cornea to the retina has a constant value for a given magnification ratio. The image pitch in the iris and the retina plane are $Md \sim 3.3 \mu\text{m}$, $M'd \sim 5.8 \mu\text{m}$ respectively. The lateral field of view of the rendered image in the iris and retina planes are $N_x Md \sim 2.5$ mm and $N_x M'd \sim 4.4$ mm respectively; the former typically fits within the normal pupil size in adults which varies from 2 to 4 mm in diameter in bright light to 4 to 8 mm in the dark [6]. The lateral field of view at the iris plane is of the order or smaller than the typical iris aperture, whereas the field of view in the eye fundus is maximized. This configuration can be adapted by changing : 1- the cornea-to-eyepiece distance, 2- the focal length of the eyepiece, 3- the sensor-to-eyepiece distance.

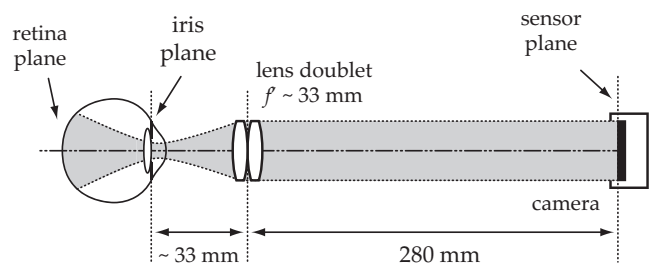


FIG. 4. illustrative optical configuration for Maxwellian view (wide-field) holographic imaging of the eye fundus with diffuse laser illumination.

IV. DIGITAL IMAGE RENDERING

Offline computation and registration of high-quality Doppler images from 12-bit, 768-by-768-pixel interferograms recorded at 35,000 frames per second by the Ametek Phantom V2511 camera was done by angular spectrum propagation [1], singular value decomposition filtering and short-time Fourier transformation [3] with the image rendering software *holowaves*. Numerical rendering of Doppler fundus images from the broad fluctuation frequency band between 2 kHz and 17 kHz and from the high frequency band from 12 kHz to 17 kHz are displayed in Fig. 3. These images were computed from raw interferograms acquired in the three layouts of Fig. 2.

V. RADIOMETRIC MEASUREMENTS AND IRRADIANCE ESTIMATION

The maximum allowable exposure of the eye to optical radiation is dictated by power areal density (irradiance) limits. To estimate the irradiance of the optical illumination of both segments of the eye, we measure cross-section distributions and profiles, and the total power of the near-infrared laser beam used for eye illumination.

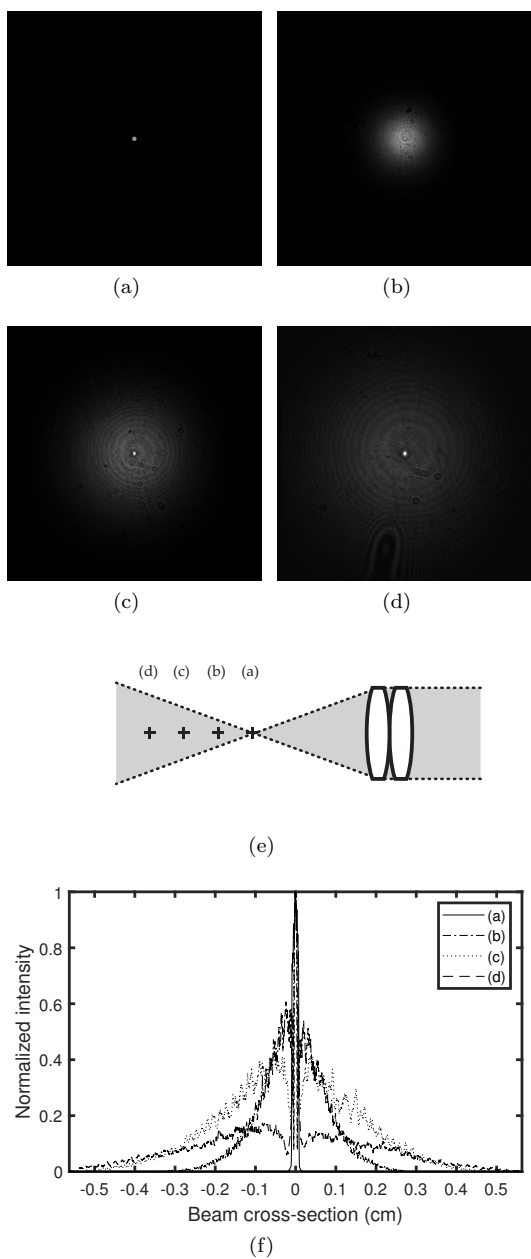


FIG. 5. Intensity distribution (irradiance) at different planes from the illumination beam waist without diffuser, towards the eye : 0.0 mm (a), 7.5 mm (b), 15 mm (c), 22.5 mm (d). Sketch of measurement locations (e). Radial cross section profiles (f).

A. Optical power

The measurements of the optical power of the illumination beam were carried out using a photodiode associated with a portable digital console for measuring optical power and energy (Thorlabs S121C & PM100D). The optical power of the laser beam was measured in the waist plane of the laser, over an active detection area of 9.7

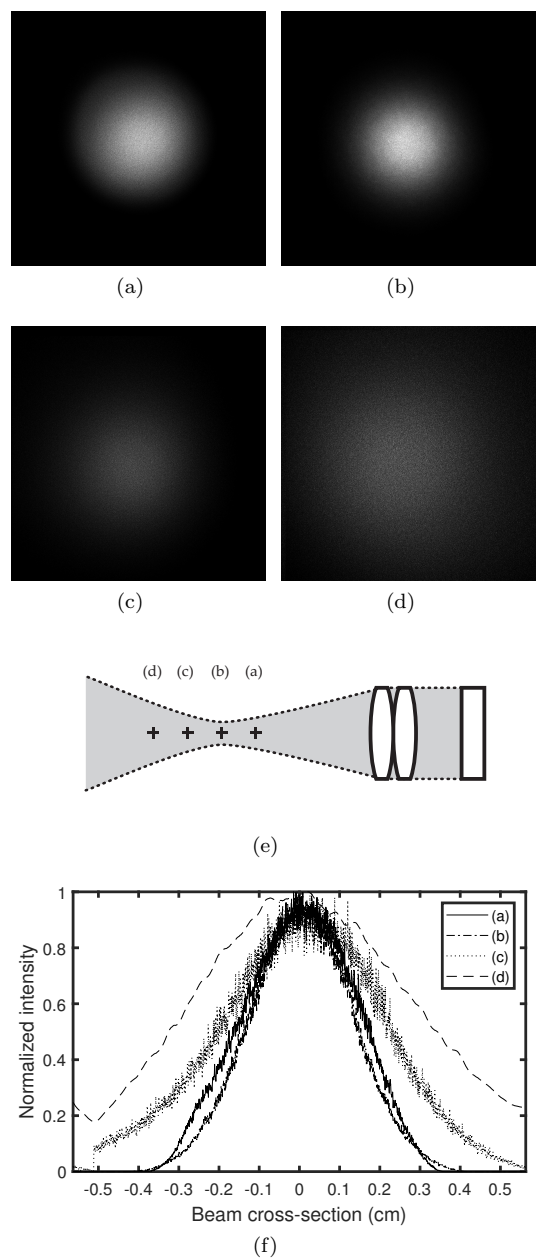


FIG. 6. Intensity distribution (irradiance) at different planes from the non-diffuse beam waist, for diffuse illumination, towards the eye : 0.0 mm (a), 7.5 mm (b), 15 mm (c), 22.5 mm (d). Sketch of measurement locations (e).

mm \times 9.7 mm with an entrance aperture diameter of 9.5 mm.

B. Beam cross section

The irradiance distribution of the optical radiation at the cornea is evaluated with and without diffuser in Fig. 6 and Fig. 5, respectively. The measurements were taken

at different distances from the focal plane to evaluate the beam cross-section distribution with the bare sensor array of a camera (XIMEA XIQ model MQ042xG-CM, 2048-by-2048 pixel frame; pixel pitch : $5.5 \mu\text{m}$). The horizontal cross section profiles in Fig. 5(f) and Fig. 6(f), averaged over ~ 165 microns vertically around the center of the distribution describe the radial distribution of the light intensity around the cornea. A quantitative irradiance map was assessed at the waist of the laser beam in diffuse illumination configuration in Fig. 7, from the measured irradiance distribution, for a total illumination power of 22 mW.

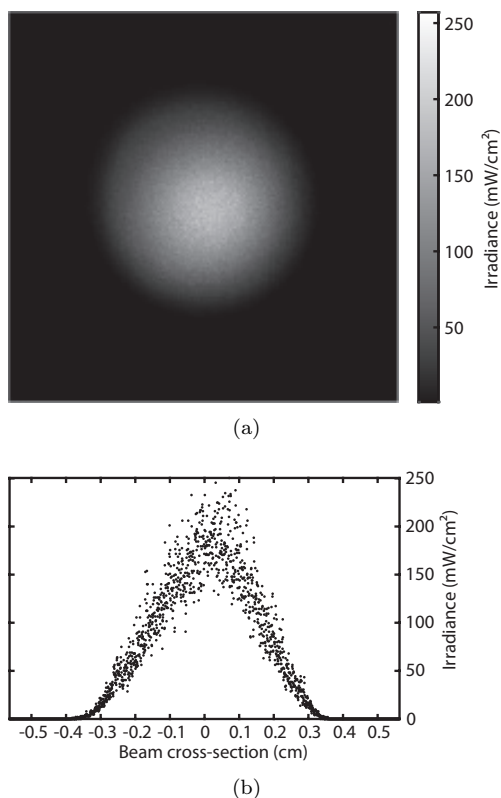


FIG. 7. Irradiance map (a) and mid horizontal cross-section (b) assessed at the waist of the laser beam in diffuse illumination configuration, onto each camera pixel, for a total optical power of 22 mW.

VI. EUROPEAN SAFETY LIMITS STANDARD

The European standard [ISO 15004-2:2007](#) specifies fundamental requirements for optical radiation safety for ophthalmic instruments and is applicable to all ophthalmic instruments that direct optical radiation into or at the eye and for which there is a specific light hazards requirement section. It is also applicable to all new and emerging ophthalmic instruments that direct optical radiation into or at the eye. Ophthalmic

instruments are classed into either group 1 or group 2 in order to distinguish instruments that are non-hazardous from those that are potentially hazardous. The proposed instrument can belong to group 1 as long as it complies with the maximum permissible exposure of the anterior and posterior segments, reported hereafter.

A diffuse laser beam is focused in front of the eye and then transmitted inside the eye, according to Fig. 2. When the anterior segment of the eye is in the focal region of the illuminating beam (Fig. 2(e)), wide-field Maxwellian view of the retina [4] is made possible. Under the eye illumination conditions illustrated in Fig. 2(c) and Fig. 2(e), the smallest of the retina and corneal surfaces exposed to the light beam is that of the cornea. Beam cross-section measurements and radial illumination profiles are plotted in Fig. 6, for a ~ 33 mm effective focal length eyepiece.

A. MPE of the retina (ISO)

According to the ISO 15004-2 (2007) standard [8], in order to avoid thermal hazard, in conditions of continuous-wave, monochromatic illumination of the retina, the maximum permissible exposure (MPE : irradiance E in W/cm^2) weighted by the thermal hazard factor R must not exceed the value (Eq. 5.4.1.6.a from Table 2 in [8])

$$R \times E = 0.7 \text{ W}/\text{cm}^2 \quad (1)$$

where E and R are the monochromatic irradiance, and the thermal hazard weighting factor. For an illumination wavelength λ between 770 nm and 1400 nm, the weighting factor R varies monotonously between $R(\lambda = 770 \text{ nm}) = 0.72$ and $R(\lambda = 1400 \text{ nm}) = 0.2$ (Table A.1 in [8]). The value $R = R(\lambda = 850 \text{ nm}) = 0.5$ is chosen for the calculations. From Eq. 1, the maximum permissible exposure of the retina is $\text{MPE} = E = 0.7/0.5 \sim 1.4 \text{ W}/\text{cm}^2$. According to the ISO norm guidelines, this limit should be assessed in a local 0.03 mm-radius ($7.0 \times 10^{-6} \text{ cm}^2$ -area) disc in the retina plane where the irradiance is maximum. Because of the high-contrast speckle illumination, it is safe to divide this irradiance value by a factor 2 ; hence $E = 700 \text{ mW}/\text{cm}^2$.

The measurement of the illumination beam cross-section is done according to the procedure described in section VB. The narrowest radial illumination distribution in Fig. 6(f) measures the minimum beam spread at its waist (line b); it is flat in its center within a disc of ~ 1 mm of radius. Let's consider that the total optical power limit P should pass through a 1 mm-radius circular aperture of area $A_0 = 3.14 \times 10^{-2} \text{ cm}^2$. We have $P = E A_0 = 700 \times 3.14 \times 10^{-2} = 22.0 \text{ mW}$.

In diffuse Maxwellian illumination conditions, the actual beam cross section profile cannot be more narrow in the retina plane than the distribution in Fig. 6(b) that is measured at the beam waist plane, at position (b) in Fig. 6(e). The irradiance distribution in this plane at each pixel location (pitch : $5.5\ \mu\text{m}$, pixel area : $3.03 \times 10^{-7}\text{cm}^2$) is assessed for a total input power of 22 mW. This total impinging optical power limit of 22 mW distributed according to Fig. 6(b) results in an irradiance map reported in Fig. 7. The maximum local irradiance in the map is about $252\text{mW}/\text{cm}^2$.

That maximum local irradiance is assessed over an area of one pixel, which is smaller than the one mentioned by the ISO norm for the retina ($7.0 \times 10^{-6}\text{cm}^2$), so that exposure compliance with the norm is always ensured. Hence, the highest irradiance E received on a 0.03 mm -radius disk at the level of the retina satisfies $E = 700\text{mW}/\text{cm}^2 \gg 252\text{mW}/\text{cm}^2$, for a total illumination power $P = 22.0\text{ mW}$. This limit is assessed for the optical configurations sketched in Fig. 2(c) and Fig. 2(e).

B. MPE of the cornea (ISO)

1. Divergent illumination of the cornea

According to Eq. 5.4.1.4 in table 2 of the ISO 15004-2 (2007) standard [8], the irradiance must be evaluated by taking the average of the highest localized radiation power received on a disc 1 mm in diameter at the level of the cornea, i.e. an area of $\sim 7.9 \times 10^{-3}\text{cm}^2$, and should not exceed $E = 20\text{mW}/\text{cm}^2$. The narrowest radial illumination distribution in Fig. 6(f) measures the minimum beam spread impinging on the cornea; it is flat in its center for more than 1 mm . A luminous power $P = 2.5\text{ mW}$ distributed spatially according to this distribution is of the order of a uniform irradiance integrated on a disk of 2.0 mm radius and $A = 0.125\text{cm}^2$ area, i.e. we can estimate the irradiance : $E = P/A = 2.5/0.125 = 20\text{mW}/\text{cm}^2$. Under these conditions, the highest average surface power of radiation received on a disk of 1 mm in diameter at the level of the cornea is $E = 20\text{mW}/\text{cm}^2$, for a total illumination power $P = 2.5\text{ mW}$. This limit is for the optical configurations sketched in Fig. 2(a) and Fig. 2(c).

2. Convergent illumination of the cornea

The maximum exposure limit for convergent illumination of the cornea is given by Eq. 5.4.1.5 in table 2 of the ISO 15004-2 (2007) standard [8]. The maximum permissible irradiance must be evaluated by taking the unweighted average of the highest localized radiation power received on a disc 1 mm in diameter at the level of the cornea. The irradiance of the cornea and of the crystalline lens within a 1 mm aperture shall not exceed

$$E = 4\text{ W}/\text{cm}^2.$$

Let's consider that the total optical power limit P should pass through this 1 mm -diameter aperture of area $A_0 = 7.85 \times 10^{-3}\text{cm}^2$. In order to mitigate the issue of the presence of any local speckle variation - i.e. constructive or destructive interference, this limit value is divided by 2. This sets the optical power limit to $P = EA_0/2 = 4.0 \times 7.85 \times 10^{-3}/2 = 15.7 \times 10^{-3}\text{W}$. The narrowest measured radial illumination beam profile in Fig. 6(f) defines the minimum possible beam extension, which can be minimized by a disc of 2 mm -diameter. A total luminous power $P = 15.7\text{ mW}$ distributed spatially with a flat distribution bounded by this disc results necessarily in an irradiance much lower than E .

A flat illumination of total power P concentrated within a disk of 2.0 mm -diameter and area $A = 31 \times 10^{-3}\text{cm}^2$, defines an irradiance level $P/A = 15.7/0.031 = 506\text{mW}/\text{cm}^2$ which complies with the MPE of the cornea. The highest irradiance P/A received on a 1 mm -diameter disk at the level of the cornea satisfies $P/A = 506\text{mW}/\text{cm}^2 \ll E = 4\text{ W}/\text{cm}^2$, for a total illumination power $P = 15.7\text{ mW}$. This limit is for the optical configuration sketched in Fig. 2(e).

VII. AMERICAN SAFETY LIMITS STANDARD

The American standard ANSI Z136.1-2014 specifies fundamental requirements for optical radiation safety for ophthalmic instruments. Within the retinal hazard region of the optical spectrum, for wavelengths from 400 nm to 1400 nm , optical sources are considered either point or extended. Point sources subtend a visual angle less than or equal to $\alpha_{\min} = 1.5\text{ mrad}$ (section 8.1 in [9]). Extended sources subtend an angle greater than α_{\min} . The MPEs for extended sources are listed in Table 5e and Table 5f in [9]. The MPEs are expressed relative to the limiting aperture area and, therefore, a limiting aperture or limiting cone angle shall be used for measurements or calculations with all MPEs. The limiting aperture is the maximum circular area over which irradiance or radiant exposure shall be averaged. (section 8 in [9]).

A. MPE for a point source (ANSI)

The maximum permissible exposure (MPE, in W/cm^2) for a point source ocular exposure for an exposure duration from 10 to $30,000$ seconds is

$$\text{MPE} = C_A \times 10^{-3} \quad (2)$$

(from Table 5c in [9]), where the correction factor for radiation wavelengths between 700 and 1050 nm is

$$C_A = 10^{0.002(\lambda - 700)} \quad (3)$$

(from Table 6a in [9]), where λ is the radiation wavelength expressed in nm. For $\lambda = 852$ nm, $\text{MPE} = 2.01 \text{ mW/cm}^2$. This value for the MPE is given only for comparison purposes with the relevant MPEs for the retina and the cornea calculated for an extended source hereafter.

B. MPE of the retina for an extended source (ANSI)

The maximum permissible exposure of the retina (MPE, in W/cm^2) for an extended source ocular exposure for an exposure duration from T_2 (Eq. 6) to 30,000 seconds is

$$\text{MPE} = 1.8 C_A C_E T_2^{-0.25} \times 10^{-3} \quad (4)$$

(from Table 5f in [9]), where the value of T_2 is given by Eq. 6, the correction factor C_A for radiation wavelengths between 700 and 1050 nm is given by Eq. 3, and the correction factor C_E for an extended source is

$$C_E = \frac{\alpha^2}{\alpha_{\max} \alpha_{\min}} \quad (5)$$

(from Table 6b in [9]), where the angular parameters α , α_{\min} , and α_{\max} are the source angle (expressed in mrad), and the lower and upper bounds $\alpha_{\min} = 1.5$ mrad, $\alpha_{\max} = 100$ mrad. The angular subtense, α , is based on an effective Gaussian image at $1/e$ of peak irradiance points, and C_E , T_2 are determined from the equations in Table 6b and Table 6c in [9]. When computing T_2 , dimensions less than α_{\min} are set equal to α_{\min} , and values greater than 100 mrad are set equal to 100 mrad. The angular parameter α estimated from Fig. 6 by using a 4.0 mm distance at $1/e$ of peak irradiance points of the narrowest effective Gaussian irradiance distribution in Fig. 6(f), and a typical axial length of the eye of 25 mm : $\alpha \sim 4/25 = 0.16$; hence $C_E \sim 171$. The correction time T_2 for an extended source is

$$T_2 = 10^{1+(\alpha-1.5)/98.5} \quad (6)$$

(from Table 6b in [9]), where the angular parameter α is set to the upper limit value $\alpha_{\max} = 100$ mrad because diffuse laser illumination satisfies the required conditions for an extended source; hence $T_2 = 100$ s. For a radiation wavelength of $\lambda = 852$ nm, the maximum permissible exposure of the retina calculated from Eq. 4, is $E = 1.8 \times 2.0137 \times 171 \times 0.31623 = 196 \text{ mW/cm}^2$. In the most restrictive case (i.e. minimum extent of the irradiance at the retina), this value is reached outside of Maxwellian view conditions, where the total optical power P would be distributed according to the narrowest irradiance profile from Fig. 6 within the retina, which is approximated by a uniform irradiance integrated on a disk of 2.0 mm radius and $A = 0.125 \text{ cm}^2$ area. In that case, $P \sim E \times A = 196 \times 0.125 = 24.5 \text{ mW}$.

As recommended in [9], the MPE for sources larger than α_{\max} are based on retinal irradiance or retinal radiant exposure, yet additional MPE of the anterior segment guidelines for the Maxwellian view of the retina are given specifically and analyzed hereafter.

C. MPE of the anterior segment for an extended source (ANSI)

The irradiation of the anterior segment in Maxwellian view is the subject of additional guidance (section 8.3.4 in [9]) : irradiation of large retinal areas (“Maxwellian View”) may result in high irradiances of the anterior segment of the eye. If the iris is not exposed, the irradiance of the cornea and of the crystalline lens within a 1 mm aperture shall not exceed $25 t^{-0.75} \text{ W/cm}^2$ for an exposure time $t < 10$ s, and 4 W/cm^2 for $t > 10$ s. The most restrictive irradiance limit is $E = 4 \text{ W/cm}^2$. This limit is the same as the one treated in section VIB 2 for the ISO norm, which gives the same estimated value for MPE of the cornea : 506 mW/cm^2 , reached for a total laser power of 15.7 mW impinging on the cornea.

D. MPE of the iris for an extended source (ANSI)

Exposure of the iris shall not exceed five times the MPE’s of the skin (see 8.4 and Table 7). For hazard analysis of the iris, the limiting aperture for corneal exposures for wavelengths 1200 nm to 1400 nm (see Table 8) shall be used for all wavelengths

VIII. DISCUSSION

In the absence of diffuser (Fig. 5), the illumination pattern in the neighborhood of the beam focal plane has a very energetic central bright spot (hot spot, Fig. 5) that should be removed to comply with both ISO and ANSI exposure safety norms. The use of an engineered diffuser that scatters all the input laser beam and filters non-diffracted light (Fig. 6) has several benefits : the issue of the presence of a hot spot is alleviated and the cornea-to-eyepiece distance can be reduced to increase the lateral field of view of the reconstructed eye fundus image. The field of view of the eye fundus image for a given iris aperture is much wider with than without diffuser, as shown in Fig. 3.

The quantitative estimates for the maximum permissible exposure (MPE) of the eye to a continuous-wave, extended near infrared laser source by Maxwellian-view holography with diffuse illumination, from our interpretation of European and American safety standards, are the following :

- MPE of the retina (ISO) : maximum local irradiance of 252 mW/cm^2 over a 0.03 mm-radius disc

for a total laser power of 22.0 mW impinging on the retina.

- MPE of the cornea (ISO) for divergent illumination : 20 mW/cm², reached for a total laser power of 2.5 mW impinging on the cornea.
- MPE of the cornea (ISO) for convergent illumination : 506 mW/cm², reached for a total laser power of 15.7 mW impinging on the cornea.
- MPE of the retina (ANSI) : 196 mW/cm², reached for a total laser power of 24.5 mW impinging on the retina.
- MPE of the cornea (ANSI) : 506 mW/cm², reached for a total laser power of 15.7 mW impinging on the cornea.

The proposed optical arrangement sketched in Fig. 1 and Fig. 4 can be used effectively for Maxwellian view (wide-field) holography of the human retina. Eye dilation is usually rendered unnecessary for imaging the posterior pole of the retina. Strict adherence to ISO and ANSI exposure safety standards is enforced in the described optical setup based on convergent diffuse laser illumination, for a total laser power of 15.7 mW impinging on the cornea. This exposure compliance should be reassessed for other eyepieces and optical configurations.

In the particular case of focused light impinging on the retina, i.e. for small-field retinal imaging, the proposed diffuse laser illumination scheme will prevent the formation of a laser hotspot in the posterior segment of the eye, so that the irradiance received by the retina stays compliant with safety limitations. In that regard, diffuse illumination acts as and improves the function of the long multimode fiber with a small core used to reduce the spatial coherence of the laser to image the cornea without causing risk to the retina [10]. That is highly valuable for high resolution retinal imaging configurations, because it decreases dramatically the local laser irradiance, and hence circumvents the issue of viewing a laser from within a collimated beam that produces a small (~ 20 to $30 \mu\text{m}$)

or nearly diffraction-limited retinal image, which will be nearly a point source, and subject to restrictive guidelines regarding maximum permissible exposure, listed in Table 5a, Table 5b, Table 5c, and Table 5d in [9]. Thorough investigation of high resolution laser Doppler imaging of the retina with diffuse illumination will be the subject of another study.

IX. CONCLUSION

Diffuse laser illumination has several important benefits in holographic imaging for ophthalmology. 1- Compliance with American and European security safety limits for ophthalmic devices is more easily achieved than with standard laser illumination of the eye, by alleviating the issue of the presence of a laser focal spot at the cornea or at the retina. 2- The irradiance level compliance with the maximum permissible exposure of the cornea and the retina can be achieved for any cornea-to-illumination focus plane distance, which enhances eye safety during patient positioning. 3- The field of view of retinal images computed numerically can be increased because the illumination and collection focus of the imaging optics can be brought closer to the cornea, allowing Maxwellian view of the retina without compromising safety. 4- Eye dilation is made unnecessary for entire posterior pole imaging. 5- No detrimental effect on Doppler images of blood flow is observed.

The authors declare that the research was conducted in the absence of any commercial or financial relationship that could be construed as a potential conflict of interest.

X. ACKNOWLEDGEMENTS

This work was supported by the IHU FOrESIGHT (ANR-18-IAHU-01), the European Research Council, the Sesame program of the Region Ile-de-France (4DEye, ANR-10-LABX-65), and the French National research agency (ANR LIDARO).

-
- [1] L. Puyo, M. Paques, M. Fink, J.-A. Sahel, and M. Atlan. In vivo laser doppler holography of the human retina. *Biomedical Optics Express*, 9(9):4113–4129, Sep 2018
- [2] Puyo, Léo, Clémentine David, Rana Saad, Sami Saad, Josselin Gautier, José Alain Sahel, Vincent Borderie, Michel Paques, and Michael Atlan. "Laser Doppler holography of the anterior segment for blood flow imaging, eye tracking, and transparency assessment." *Biomedical optics express* 12, no. 7 (2021): 4478-4495.
- [3] Léo Puyo, Michel Paques, and Michael Atlan, Spatio-temporal filtering in laser Doppler holography for retinal blood flow imaging, *Biomed. Opt. Express* 11, 3274-3287 (2020)
- [4] Sliney, David, et al. "Adjustment of guidelines for exposure of the eye to optical radiation from ocular instruments: statement from a task group of the International Commission on Non-Ionizing Radiation Protection (IC-NIRP)." *Applied optics* 44.11 (2005): 2162-2176.
- [5] Puyo, Leo, Loic Bellonnet-Mottet, Antoine Martin, Francois Te, Michel Paques, and Michael Atlan. "Real-time digital holography of the retina by principal component analysis." *arXiv preprint arXiv:2004.00923* (2020).
- [6] Robert H. Spector *Clinical Methods: The History, Physical, and Laboratory Examination*

- tions 3rd edition, Chapter 58 : The pupils
<https://www.ncbi.nlm.nih.gov/books/NBK381/>
- [7] William F Ganong and Kim E Barrett. *Review of medical physiology*, volume 22. McGraw-Hill Medical eNew York New York, 2005.
- [8] AFNOR *European Standard for Safe Use of Lasers ISO*, 2007.
- [9] Laser Institute of America *American National Standard for Safe Use of Lasers ANSI Z136.1-2014*.
- [10] Egidijus Aukorius, Dawid Borycki, and Maciej Wojtkowski, "Multimode fiber enables control of spatial coherence in Fourier-domain full-field optical coherence tomography for in vivo corneal imaging," *Opt. Lett.* 46, 1413-1416 (2021)

1.3 Optical configuration

The new setup yields to a new optical configuration. The numerical aperture of the system for digital holography can be limited by one of the three factors listed below. To compare between them and choose the effective NA of the system it is necessary to calculate limiting angles in one plane. In this case we will compare them in the focal plane of the image.

- **the pupil of the eye** as mentioned in Chapter 1 is typically of 5 mm diameter. As the pupil size remains unchanged by the lenses present in the system, the effective acceptance half angle is of 0.075 rad.
- **size of the sensor array** : the number of pixels taken varies between the acquisitions. Let us consider a square sensor array of 512 x 512 size, the pixel pitch is of 28 μm , the effective half angle is then equal to 0.028 rad.
- **coherence acceptance angle of the pixels**, half angle can be calculated as $\frac{\lambda}{2d}$ where d is the pixel pitch, and is equal to 0.015 rad.

One can see that the coherence acceptance angle of the pixels is much smaller than the other two and is going to determine the effective NA in all of the configurations considered. The field of view obtained on the other hand is limited by the size of the sensor array. Other limitations can arise from insufficient illumination, which needs to be maximally extended.

1.4 Conclusions

Introducing a diffuser into the optical setup significantly expanded the field-of-view. Additionally, it created a fully secure system where, even if the acquisition process does not strictly follow the recommendations, there is no risk to the patient. We have also confirmed that the variability of angles induced by the diffuser does not compromise the detected signal. Consequently, we have addressed one of the existing challenges in the LDH acquisition process. As we can now capture wide field-of-view images, our next step is to ensure that their resolution remains uncompromised by any potential aberrations.

Chapter 2

Aberration correction

2.1 Introduction

For many imaging techniques, wavefront distortion presents an important challenge compromising the accuracy of images obtained. It can be induced by either the medium in which the signal propagates, like in the case of stellar imaging where aberrations are induced by turbulence, or by the inhomogeneous sample of varying optical index. In the case of the eye fundus imaging the aberrations are mostly induced by the anterior segment of the eye. One of the main difficulties in removing ocular aberrations results from the fact that the wavefront distortion is dynamic and changes rapidly in the course of measurements due to the accommodation and eye movements. The techniques developed to measure and compensate for the dynamic aberrations are referred to as Adaptive Optics (AO) - as they contain an element which enables the modification of optical elements in the system and, as a result, the control of the wavefront.

2.1.1 Adaptive Optics (AO)

Adaptive optics were first introduced in 1953 by Horace W. Babcock [43] to compensate for the wavefront distortion caused by the turbulence in stellar imaging. In 1997 Liang et al. coupled an AO system with a flood-illumination ophthalmoscope and used it to image the retina [44]. This invention enabled, for the first time, the identification of individual photoreceptor cells, which was so far impossible due to inaccuracy of the images. Thanks to AO, observing the mosaic pattern of cone photoreceptors has become possible, allowing investigation of their density and distribution in both healthy and diseased retinas [45]. Furthermore, AO has enabled: imaging of RPE cells, which play a crucial role in the health and function of photoreceptors, tracking of the inflammatory cells migration, observing the deposition of extracellular material in retinal degenerative conditions [46], and revealing of cell transport in the capillary structure around the fovea [47]. In conclusion, the introduction of AO to visual science has enabled detailed analysis and monitoring of numerous phenomena crucial for diagnosing and understanding various types of diseases.

The AO systems are typically composed of three key elements [48]:

- **a sensor** that measures the wavefront deformation, that is, the path difference between each point of the pupil and a plane orthogonal to the propagation direction. The most commonly used wavefront sensor is referred to as Shack-Hartmann (SH). It is composed of a lenslets array and a camera placed in the focal plane of the latter (Fig. 2.1). The SH wavefront measurement

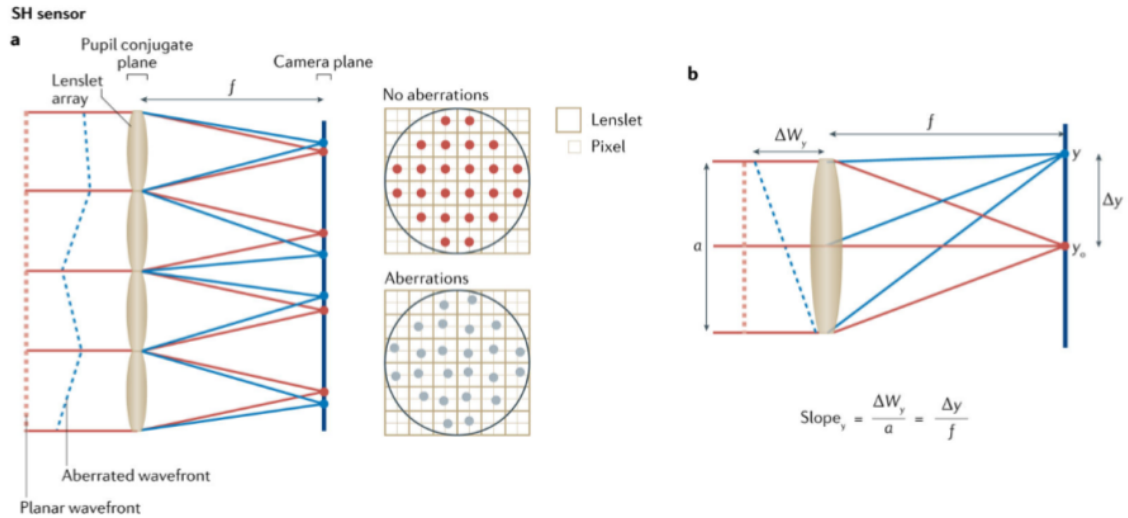


Figure 2.1: Figure adapted from [48]. Shack-Hartmann wavefront sensor is composed of a lenslets array conjugated with the pupil, and a camera placed behind it at the distance corresponding to the focal length of the lenslets. Diagram on the right demonstrates how the local slope in the pupil plane corresponds to the shift in the direct space.

relies on projection of a point on the retina which will act as a secondary source of light, which is performed before the actual image acquisition. There exist other wavefront sensors which can be used instead of SH, such as the pyramid wavefront sensor or the Roddier test.

- **a corrector** that can compensate for aberrations, that is, add a varying delay to the wavefront. Fig. 2.3 shows the principle of functioning for the three main types of wavefront correctors.
- **a controller** that converts the signal measured by the sensor to the delays imposed by the corrector.

Alternatively it is possible to omit the sensor and search for the best resolution of the image as a function of the correction imposed. In such a case, one can either use a model describing aberrations with a finite number of parameters (such as Zernike basis) or use a model-agnostic approach.

One can identify three main characteristics defining the inherent efficiency of the AO systems [48]:

- **dynamic range of correction:** it is a limit of maximal deformation which the corrector can impose on the wavefront. As eye aberrations have typically the peak-to-valley value of around $11 \mu\text{m}$, that is the minimum dynamic range which is required for retinal imaging.
- **number of corrected modes:** it is effectively a number which describes the precision of the measurement, is limited by the number of degrees of freedom of the sensor (for example lenslets in SH) and number of corrector elements (of the deformable mirror for example).
- **response time:** it is the time that the deformable mirror takes to converge to the desired position

Moreover, AO represents a cumbersome and expensive addition to imaging devices. The complexity and cost of implementing AO systems can limit their accessibility and widespread adoption in clinical settings. Consequently, the methods for digital aberration correction have been

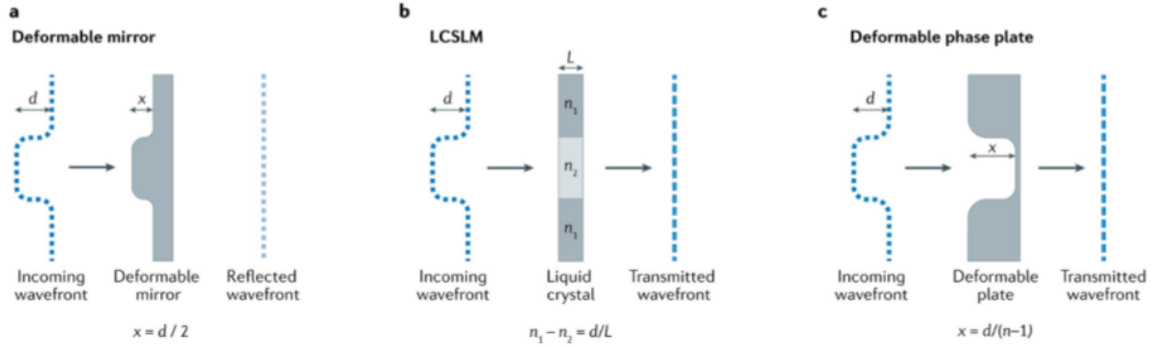


Figure 2.2: Figure adapted from [48]. Three most common types of wavefront correctors.

intensely searched and thoroughly investigated. Digital correction methods aim to mitigate aberrations through advanced image processing algorithms, offering a more practical and cost-effective alternative. These methods have shown promise in improving image quality without the need for physical modifications of the imaging system.

2.1.2 Digital aberration correction (DAO)

Aberrations can be corrected digitally, provided that the imaging technique enables stable phase measurement across the field of view. Similar to hardware-based AO, the solution may or may not involve wavefront measurements. The sensorless approach typically involves solving an optimization problem where the aberration phase is described by a set of analytical functions. It has been demonstrated that this technique enables the correction of high-order aberrations and significantly improves the resolution of volumetric images of the human retina [50, 51]. In these studies, image sharpness metric was employed as a gain function and wavefront distortion was approximated as a linear combination of Zernike polynomials. An example of results obtained is represented in Fig. 2.4.

A different approach based on wavefront measurement has been proposed by Abishek Kumar et al. [52]. This technique can be seen as a numerical version of the Shack-Hartmann wavefront sensor, employing the cross-correlation of reduced-field images for the shifts assessment. It was first demonstrated on non-biological samples that this approach can be used for numerical re-focalization in full-field swept-source OCT, allowing for sharper images at a larger depth of field (DOF) than previously possible (Fig.2.5). In 2017, Laurin Ginner et al. applied this technique to in-vivo line-field spectral-domain OCT imaging of the human retina [53]. One of the main problems encountered was the ambiguous distribution of the cross-correlation function due to the low SNR of a single en-face image. To mitigate this issue, the proposed strategy was to first correct for the second rank of Zernike polynomials, then use photoreceptors as “guide stars” for shifts in subapertures assessment and correct for higher-order aberrations in this layer exclusively. An example of results obtained are represented in Fig. 2.6.

In 2011, Changgeng Liu and Myung K. Kim proposed combining digital holography with AO for ocular imaging, leveraging the fact that holographic detection acts effectively as a wavefront sensor [49]. First, a spot is projected on the retina using a fine-size laser to create a “guide star,” similar to an SH wavefront sensor. The field detected, corresponding to the aberrations imposed by the system, is stored in memory. The second step involves recording the actual full-field image and correcting it numerically using the previously saved phase function. In later works, the system was extended to incoherent source imaging [54], and an algorithm allowing the combination of aberration

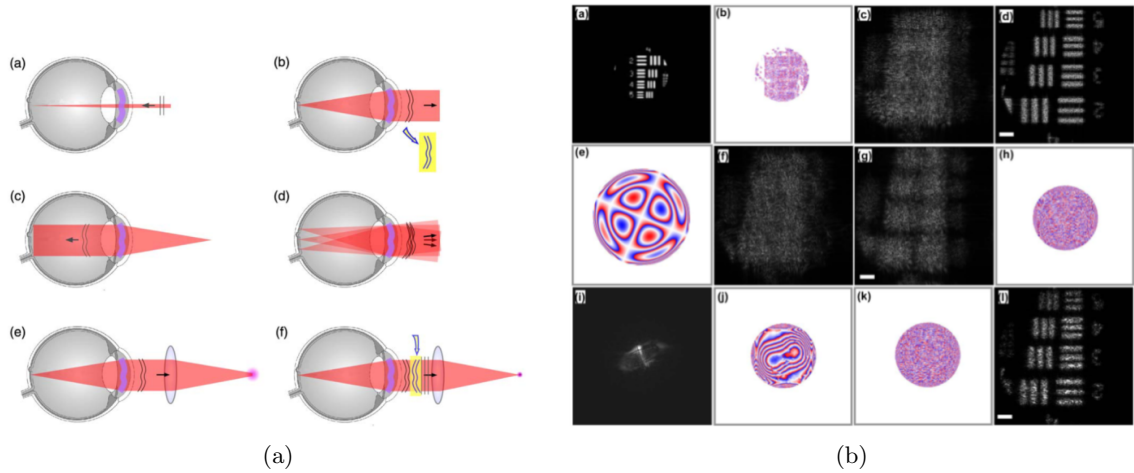


Figure 2.3: Figures adapted from [49]. The principle of AO in holography of the human eye (a) (detailed description in text). (b) The simulation results obtained using the "guide star" field for both aberration correction and digital propagation of the holograms. (b.a) target image, (b.b) associated phase, (b.c) optical field obtained in the camera plane, (b.d) focused image of (b.c), (b.e) aberrating phase, (b.f) optical field in the camera plane with aberrations, (b.g) refocused image of (b.f), (b.h) phase of the image with aberrations in the pupil plane, (b.i) hologram of the "guide star", (b.j) FT of (b.i), (b.k) corrected field (b.h), (b.l) corrected image.

correction from a field emitted by a "guide star" with simultaneous hologram propagation was proposed and successfully applied [55].

Amaury Badon et al. presented a different approach for matrix imaging [56]. The sample is illuminated at many different angles and the complex field backscattered for each of them is recorded separately. After removing the geometric components from the detected phase functions, the latter are assembled into a distortion matrix. This matrix represent the deviation from the ideal case without aberrations. Calculating SVD of this matrix allows extracting the common phase, representing the system's aberrations. The main draw back of this technique lies in the size of the array which needs to be diagonalised, and hence the size of the memory required for the calculations.

2.1.3 Aberration correction for LDH

As discussed above, there are multiple approaches for aberration correction for the imaging of the human eye. The choice of the most appropriate strategy depends on the imaging technique used. Let us compare here the impact of aberrations on the signal detected for FF-OCT and LDH, which will highlight the importance of adapting the AO approach to the imaging technique used.

The two main sources of artifacts in FF-OCT are: ocular aberrations and the presence of multiply scattered photons in the field detected. To reject the latter coherence "gating" can be employed. By decreasing the coherence of the illumination beam we can reduce the contributions of non-ballistic photons to the interferometric signal. However, as a result, aberrated photons - the ones for with the optic path was extended due to the wavefront distortion - are also rejected. In consequence, no digital aberration correction can compensate for this effect as the aberrated photons were simply not detected. For this reason hardware-based AO (HAO) is currently the most commonly used technique for OCT. It is also worth noticing that in the case of OCT any axial motion will have the same

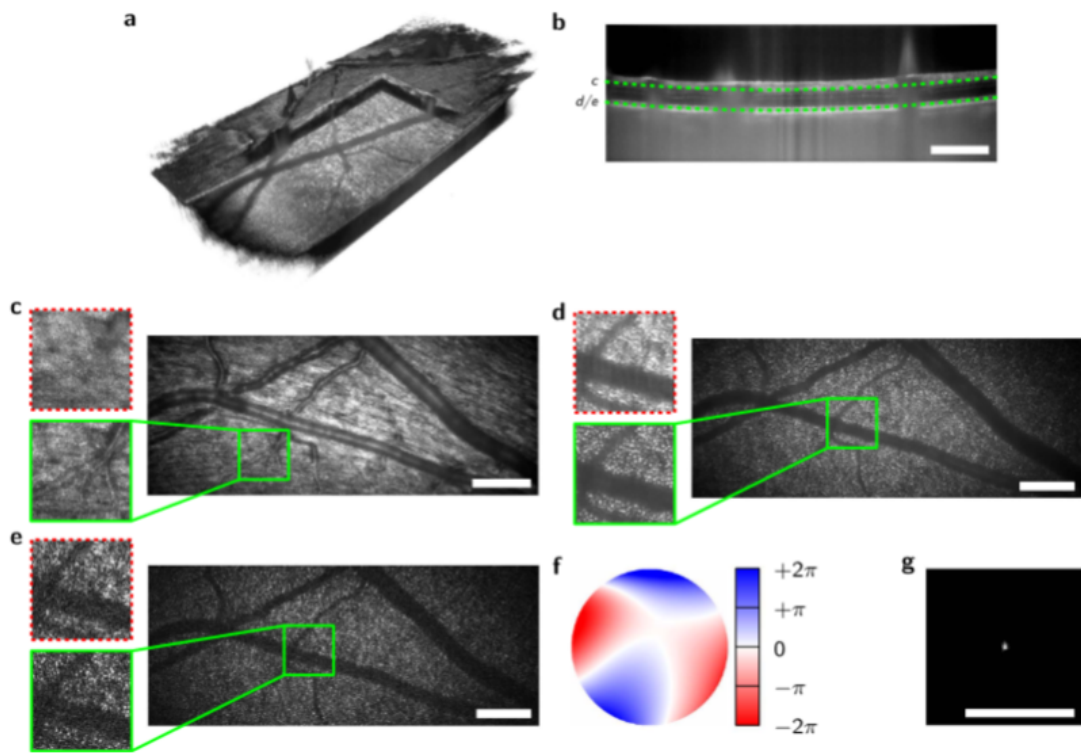


Figure 2.4: Figure adapted from [50] illustrating the results obtained with iterative aberration correction. (a) 3D reconstruction of the retinal area imaged, (b) corresponding cross-section with layers of interest in dashed-lines, (c,d,e) areas of interest, zoomed uncorrected and corrected images in red-dashed and green frame respectively. (f) wavefront used for correction, (g) PSF obtained after aberration removal.

Defocus correction algorithm	Processing time (s)*		Performance (Improvement)		Comments
	2-D	3-D	SNR	DOF	
FM	0.01	0.17	20 dB at $z = 1.5\text{mm}$, 5 dB at $z = 2.5\text{mm}$	7x	Fastest among the three, same performance as IS
IS	0.20	4.97	20 dB at $z = 1.5\text{mm}$, 4 dB at $z = 2.5\text{mm}$	7x	Computationally expensive, achieves same performance as FM
DAO	0.22	5.54	25 dB at $z = 1.5\text{mm}$, 17 dB at $z = 2.5\text{mm}$	11x	No knowledge of system parameters required, works better for inhomogeneous sample, computationally expensive

Figure 2.5: Figure adapted from [57]. Table comparing different focusing algorithms for FF-SS-OCT. FM - forward model, IS - inverse scattering.

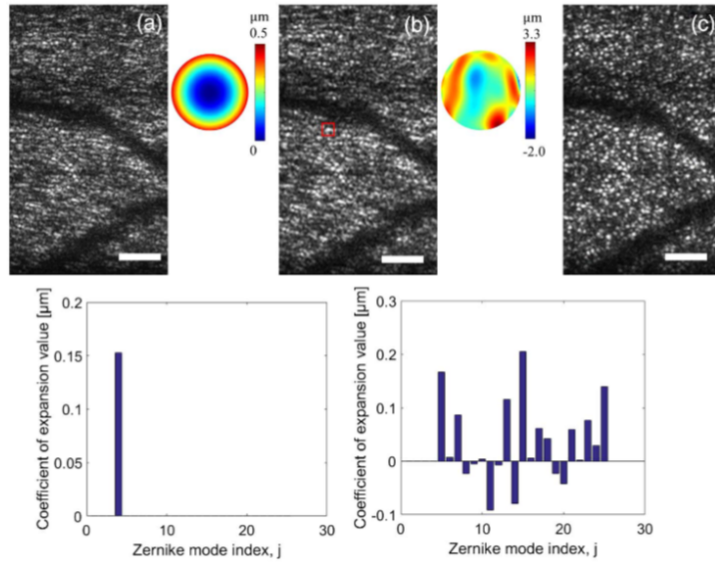


Figure 2.6: Figure adapted from [53]. Photoreceptor images were obtained using line-scanning SD-OCT and corrected using numerical Shack-Hartmann method. (a) image with aberrations uncorrected, (b) image with only defocus corrected, (c) image with high-order aberrations corrected with the photoreceptor in red frame used as a “guide star.”

effect as imposing a defocus and can hence be seen as an aberration as long as the displacement is not too important. In the opposite case, it is necessary to move the reference arm accordingly [28]. Nonetheless, like all techniques, HAO has its shortcomings and its performance is limited especially for patients with complex ocular aberrations. A possibility of performing both HAO and CAO has been investigated [58]. The conclusion, which can be made from this article, is that CAO allows further resolution improvement of the retinal images acquired with HAO.

In LDH, as mentioned in the Chapter 3, the coherence length is very high. As a result, all photons are detected. The only “gating” or “tagging” present is based on the spectrum widening which acts as a contrast agent and depends on the velocity of the flow and, as a result, also on the size of the vessel. It is difficult to define precisely what is the smallest spectrum widening LDH is capable of detecting in the human eye and whether the sensitivity varies with the absolute value of the flow. The numerical aperture of LDH is low compared to other retinal imaging devices. As a result, on the one hand the resolution of the device is by principle worse than that of the OCT and, on the other hand, the impact of higher order aberrations on the images is less critical. Axial motion in LDH does not represent a significant issue as the propagation distance is anyway chosen empirically. Nonetheless, for long videos rendering the propagation distance can vary slightly and effectively act like defocus. In conclusion, the resolution of the LDH is limited by two key factors: precision of the spectrum broadening measurement and low-order ocular aberrations. Additionally, the SNR is limited by presence of multiply scattered photons, which can be also seen as lack of any axial sectioning.

The ideal aberration compensation technique for LDH should principally correct low-order distortions in wide range of magnitudes with the time high resolution. Firstly, we eliminate the hardware based AO, which is judged a too complex and expensive approach, especially given that we do not encounter the problem of undetected photons. The pros and cons of three digital approaches mentioned above were considered:

- **sensorless iterative approach** allows to efficiently assess higher order aberrations but requires long computation time, especially if the magnitude of the aberrations is very high
- **distortion matrix approach** is based on the presence of multiple acquisitions for different illumination angles, which we do not have access to. However we have access to a supplementary degree of freedom - time - which could be potentially employed for the distortion matrix approach. Unfortunately for now the memory required for SVD calculations of the matrix of this size is beyond our capacities.
- **subaperture correlation** has limited precision due to the uncertainty relationship between the size of the subapertures and the precision of the shift assessment. However, it operates in one-shot and one has a full control on the computing regardless of the magnitude of the aberrations found.

Due to the reasons mentioned above it was decided that the sub-aperture correlation-based aberration correction was the most suitable and pragmatic approach for this thesis.

2.2 Aberration compensation in Doppler holography of the human eye fundus by sub-aperture signal correlation

This section features an article titled “Aberration Compensation in Doppler Holography of the Human Eye Fundus by Sub-Aperture Signal Correlation,” which has been accepted for publication

in Biomedical Optics Express. In this paper, we have demonstrated for the first time that the numerical Shack-Hartmann algorithm can be applied to LDH data to measure and correct the distorting wavefront, thereby improving the resolution of the images obtained.

Aberration compensation in Doppler holography of the human eye fundus by subaperture signal correlation

ZOFIA BRATASZ,^{1,2,*} OLIVIER MARTINACHE,^{1,2} JULIA SVERDLIN,^{2,3}
DAMIEN GATINEL⁴ AND MICHAEL ATLAN^{1,2}

¹*Institut Langevin, ESPCI Paris, PSL University, CNRS, 75005 Paris, France*

²*Quinze-Vingts National Eye Hospital, 28 rue de Charenton, Paris, 75012, France*

³*Essilor Instruments. France*

⁴*Rothschild Ophthalmologic Foundation, Clinical studies department, Paris, 75019, France*

**zosiabratasz@gmail.com*

Abstract: The process of obtaining images of capillary vessels in the human eye's fundus using Doppler holography encounters difficulties due to ocular aberrations. To enhance the accuracy of these images, it is advantageous to apply an adaptive aberration correction technique. This study focuses on numerical Shack-Hartmann, which employs sub-pupil correlation, as the wavefront sensing method. Application of this technique to Doppler holography encounters unique challenges due to the holographic detection properties. A detailed comparative analysis of the regularization technique against direct gradient integration in the estimation of aberrations is made. Two different reference images for the measurement of image shifts across subapertures are considered. The comparison reveals that direct gradient integration exhibits greater effectiveness in correcting asymmetrical aberrations.

1. Introduction

The prevalence of astigmatism, hyperopia and myopia among adults is estimated at 40.4%, 30.9% and 26.5%, respectively [1]. Hence, high-resolution imaging of the human eye fundus, particularly in clinical applications, requires a robust aberration correction technique. Many techniques currently employed benefit from regularization with a Zernike polynomials basis which accurately describes the aberration wavefront over the circular pupil. Moreover, the second radial order of Zernike polynomials statistically represents around 91% of the total root-mean-square wavefront error [2]. As a result, determining only 3 parameters considerably improves the resolution of the images obtained. Furthermore, Zernike polynomials up to 4th describe above 99% of the total root-mean-square wavefront error [2].

Since wavefront distortion is a common problem in imaging, various compensation techniques have been developed to compensate for it. Several of them have been successfully adapted to ophthalmic devices. One of the most frequently used solutions is based on adaptive optics designed for stellar imaging [3–5]. Several reviews have treated the topic of adaptive optics applied to high resolution imaging [6–8]. Alternatively, the aberration compensation can be made by deconvolution of the total measured field [9, 10]. However, for some ophthalmic applications, the guide star approach may be cumbersome. To overcome this issue, digital wavefront estimation in sub-pupils [11–14], and blind iterative phase compensation based on the quality of image features [15–17] were investigated for digital holographic imaging. The main limitation of wavefront sensing is the compromise between the area of wavefront sampled and the precision of slope estimation [17]. On the other hand a blind iterative approach has a longer computation time.

In this paper, it is demonstrated that digital wavefront estimation in subapertures [11], which is referred to as the numerical Shack-Hartmann method, can be applied to laser Doppler holography (LDH) [18] to improve resolution and reveal retinal capillaries. The numerical Shack-Hartman

approach based on sub-pupil correlation is used to measure local slopes of the aberration wavefront. The estimation of the aberration wavefront from measured local gradients can be done by projection on a chosen finite basis. The authors of [11], in their initial paper, proposed using a Taylor monomials basis. However, for applications in the in-vivo imaging of the human retina with optical coherence tomography, a Zernike polynomial basis was chosen as a regularization technique [17, 19]. Alternatively, the aberration wavefront can be estimated from the measured local slopes by direct gradient integration [20]. A comparative analysis between regularization via projection onto Zernike polynomials and direct gradient integration for aberration estimation is performed. The results obtained indicate that the latter is more robust in compensating asymmetrical aberrations in Doppler holography.

2. Experimental setup

The optical configuration of the experimental device used for Doppler holography of the human retina is based on a Mach-Zehnder in-line interferometer [21] (Fig. 1). A laser beam is split into reference (10% of the optical power) and object arms (90% of the optical power). The latter passes through a diffuser (Thorlabs ED1-C20-MD, circle pattern engineered diffuser) and is focused by a lens (Thorlabs LB1630-B, focal length $f = 100$ mm) in front of the eye to maximise the area of the retina that is illuminated. The diffuser-to-eyepiece centre distance is ~ 100 mm. The geometry of the system is based on two beam-splitting cubes, one of which is polarizing which enable the rejection of specular reflections. The reference beam passes through a lens (Thorlabs LB1676-B, focal length 100 mm) that shapes its wavefront in the detection (camera) planes to benefit from homogenous illumination across the sensor, and increase the blur rate of the twin holographic image in the numerical reconstruction. Two cameras are used to record the sequence of interferometric patterns: one serving for real-time preview (Ametek Phantom S710, frame rate: 5 kHz, pixel pitch: $20 \mu\text{m}$), the second for offline rendering (Ametek V2012, frame rate: 33 kHz, pixel pitch: $28 \mu\text{m}$). The sampling frequency is well above the established requirements for the phase stability in the human eye [22]. The most significant difference with previously reported configurations [18] is the presence of the optical diffuser that scatters the illumination beam.

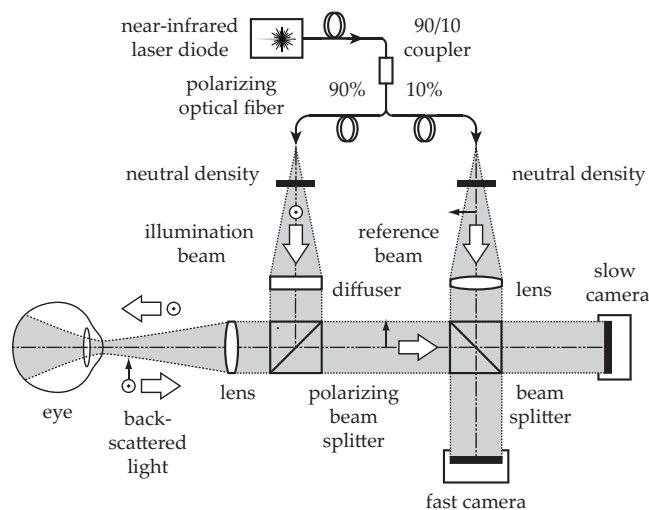


Fig. 1. Sketch of the optical configuration. An inline Mach-Zehnder near-infrared laser interferometer mixes the light backscattered by the eye fundus with the reference beam. Two cameras record the optical interference patterns.

The wavelength of the near infrared laser is $\lambda = 852 \text{ nm}$, the pixel pitch of the offline camera used to sample all the frames used as raw data in this study is $d = 28 \mu\text{m}$, the average distance between the volunteer's cornea and retina $d_{\text{eye}} = 25 \text{ mm}$, the number of lateral pixels of the sensor frame in each direction is $N_x = 768$. The subject's pupil is located at a distance of approximately 80 mm from the eyepiece (Fig. 2). The image of the retina is formed with a $M = f/d_{\text{eye}} = 100/25 = 4$ magnification ratio, at $\approx 260 \text{ mm}$ from the camera. The pixel pitch of the numerically rendered image in the sensor plane via the angular spectrum propagation method for reconstruction distances $z < N_x d^2/\lambda \approx 0.71 \text{ m}$ has a constant value of $28 \mu\text{m}$. The resulting field of view in the retina plane is equal to $N_x d/M = 5.375 \text{ mm}$, which corresponds to the field of $\approx 12^\circ$.

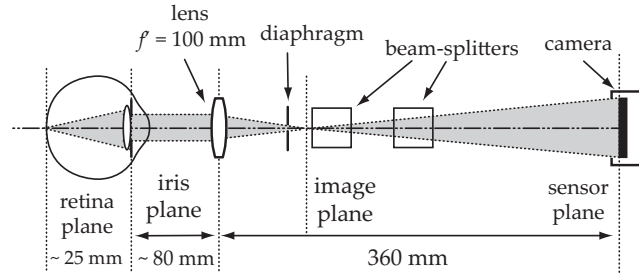


Fig. 2. Scheme of optical configuration for holographic imaging of the eye fundus with diffuse laser illumination, including approximate optical conjugations. The field of view is given primarily by the magnification of the lens but can be affected by the image of the pupil acting like a field diaphragm.

3. Digital image rendering

A 512-frame sequence of 12-bit, 768-by-768-pixel interferograms recorded at a rate of 33,000 frames per second, is numerically propagated using of the angular spectrum method [18] to reconstruct holograms of the eye fundus with a distance parameter $z \sim 0.35$. After singular value decomposition filtering, applied to reject the principal components of largest intensity [23], the power Doppler signal in the band 3-16.5 kHz is calculated using short-time Fourier transformation with a cutoff frequency of 3 kHz. This standard image rendering procedure is performed with the open-source image rendering software [Holowaves](#) (branch : master, commit : 17df875).

Four image aliases may appear at horizontal and vertical offsets as seen in Fig. 3a due to the excessive difference between curvatures of the reference and object optical waves interfering at the sensor array. To filter out their presence in post-processing, the following procedure is carried on. Firstly, the position of replica is determined by the local maxima of the cross-correlation function of the rendered image (Fig. 3b). Next, a basis of images shifted to the positions of the replicas is created (Fig. 3c). A singular value decomposition of this basis creates a set of eigenvectors that carry the spurious image features to be removed (Fig. 3b). We subtract from the images with shifted features the first eigenvector of the SVD, and we sum them up to create the image to be removed (Fig. 3e) from the original. Finally, we obtain an image where replicas intensity is attenuated (Fig. 3f). The attenuation can be quantified by comparing the ratio of secondary peaks with respect to the maximal value of the cross-correlation function before and after correction. Using this method we can evaluate that the intensity of top and left replicas initially represented 7.85% of the main features and decreased 2.75 times. The bottom and right replicas had an initial intensity of 3.76% (with respect to the main features) which decreased

2.08 times. The code used to obtain those results can be found in the open-source repository [ImageReplicaRemoval](#) (branch : master, commit : 9481839).

4. Numerical estimation of the aberration via subaperture signal correlation

4.1. Method

The combination of the recording system and signal processing performed in LDH [18] enables the extraction of the complex object field information from optically-acquired on-axis interferograms. The algorithm of numerical phase correction for interferometric full-field imaging systems based on subaperture correlation [11] can hence be used in Doppler image rendering routines to perform aberration correction.

Let $A_0(x, y, z)$ and $A(x, y, z)$ stand for the wavefront function in the Fourier plane before and after deformation. Using isoplanatic approximation, that wavefront can be expressed as:

$$A(x, y) = A_0(x, y)e^{i(\Phi(x, y) - \Phi^{\text{corr}}(x, y))} = A_0(x, y)e^{i\Phi^{\text{res}}(x, y)} \quad (1)$$

where $\Phi(x, y)$ is the initial phase in the pupil plane with aberrations, $\Phi^{\text{corr}}(x, y)$ is the wavefront corrector and $\Phi^{\text{res}}(x, y)$ is referred to as the residual phase. The error of the aberration estimation can be assessed by calculation of the variance of residual phase. The subaperture images correlation algorithm [11] finds the $\Phi^{\text{corr}}(x, y)$ function in the pupil plane, by approximating the wavefront with a finite number of inclined plates (Shack-Hartmann wavefront sensing method). Additional regularization can be performed assuming that the aberration phase can be represented as a linear combination of a series of known functions, for instance:

$$\Phi^{\text{corr}}(x, y) = \sum_j c_j Z_j(x, y) \quad (2)$$

where Z_j are Zernike polynomials.

4.2. Implementation

The digital optical field in the image plane is obtained by angular spectrum propagation from each recorded interferogram (Fig. 4a). This field is then propagated to the reciprocal plane of the reconstructed image by spatial Fourier transformation and divided into regularly-spaced square apertures. Within each subaperture, the local wavefront distortion is approximated by a plane, tilted phase. The signal from each subaperture is processed separately to obtain an image by spatial Fourier transformation, singular value decomposition filtering [23], and short-time Fourier transformation over the 512-frame sequence to reveal a power Doppler image in the band 3-16.5 kHz (Fig.4b), whose field of view corresponds to that of the initial image but its resolution is decreased due to the support reduction in the aperture plane. In the first approximation, the aberration wavefront modifies images by shifting them respectively according to local phase tilts. Those translations are quantified using the cross-correlation function (Fig.4c) between reconstructed images from subapertures. A subpixel precision of shift estimation is achieved by fitting a parabola to the peak found. Additionally, when working with data with low signal-to-noise ratio, it can be advantageous to reject certain subapertures over which the cross-correlation peak value remains under the chosen threshold, meaning that resemblance between the features is low. In the end, the aberration wavefront is assessed from the measured vector of shifts from each subaperture (Eq.4), where x and y dimensions are processed independently.

To express the aberration wavefront as a linear combination of p first Zernike polynomials, a matrix of transition between two bases is calculated. Each Zernike polynomial is split into subapertures, over which the local gradient is calculated. Obtained shifts in the subapertures are assembled to form a $n \times p$ matrix \mathbf{M} (Eq.3) representing p Zernike polynomials in the base of n couples of horizontal and vertical shifts between the subimages. Due to the circular vignetting of

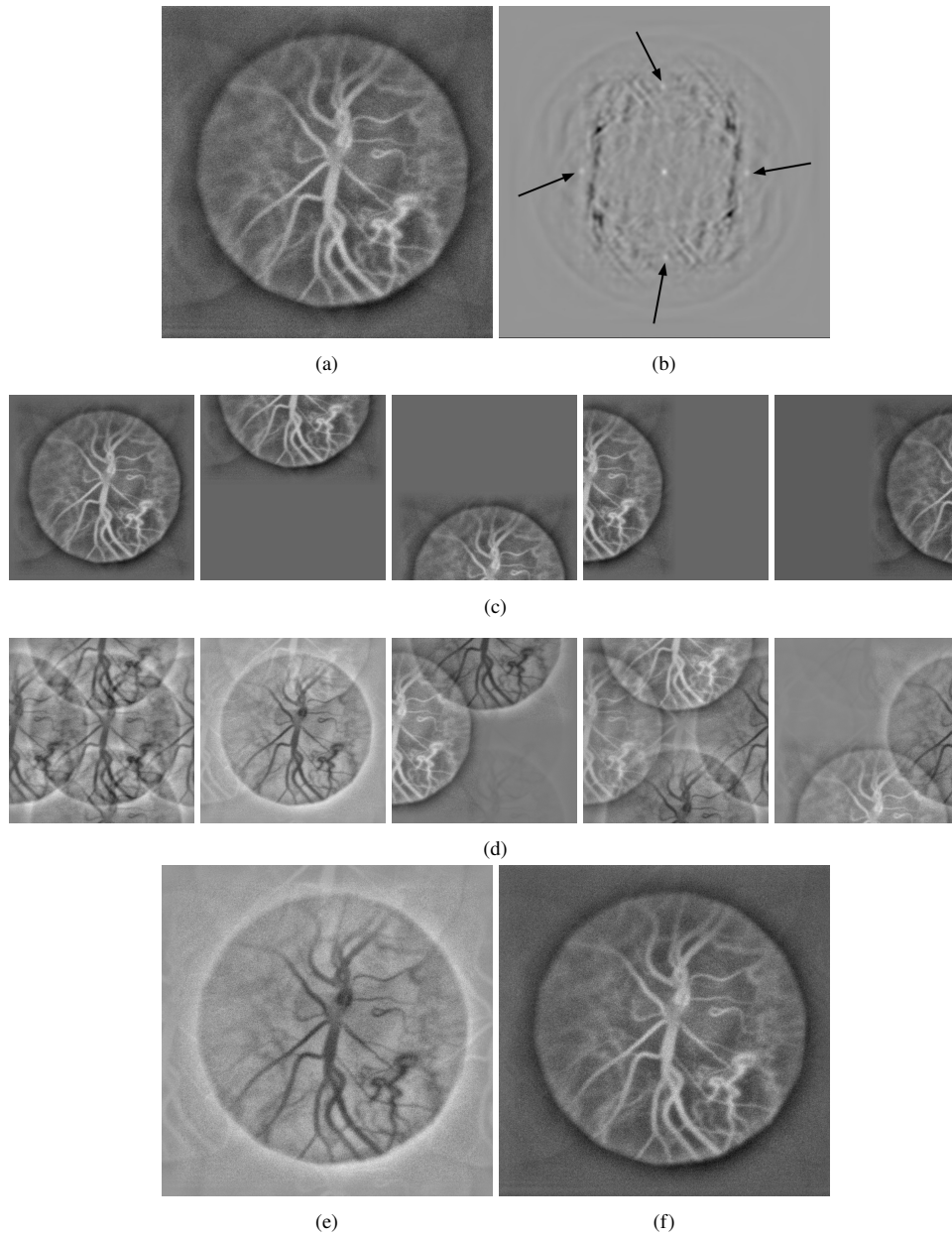


Fig. 3. 3a Image of the eye fundus with ghost images in four directions. 3b Cross-correlation function of the initial image allowing to find replicas positions. 3c Basis of images shifted to the position of the replicas. 3d SVD decomposition of the previous basis. 3e Replica image to be subtracted. 3f The same image with replicas attenuated using singular values decomposition approach.

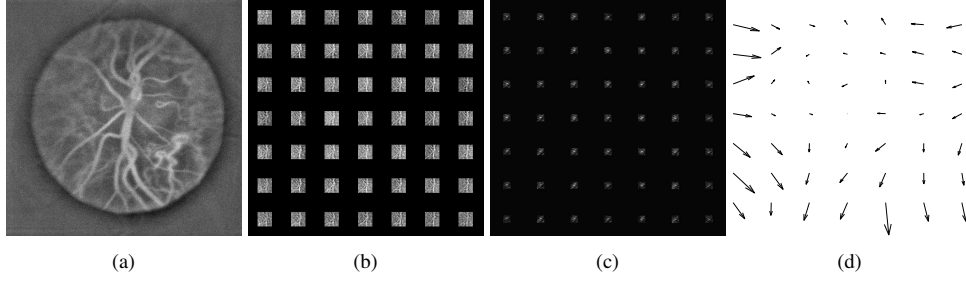


Fig. 4. Diagram illustrating steps of the numerical Shack-Hartmann algorithm. 4a Image of the retina rendered without aberration correction. 4b Images rendered from fields in subapertures with masked outer parts. 4c Cross-correlations between subimages. 4d Shift vectors of the subimages.

Zernike basis functions, subapertures from the corners are removed from the list of n measured shifts. The criterion of exclusion is based on assessment of the subaperture centre position with respect to the circle.

$$\mathbf{M} = \begin{pmatrix} m_{11} & m_{12} & \cdots & m_{1p} \\ m_{21} & m_{22} & \cdots & m_{2p} \\ \vdots & \vdots & \ddots & \vdots \\ m_{n1} & m_{n2} & \cdots & m_{np} \end{pmatrix} \quad (3)$$

$$y = \begin{pmatrix} y_1 \\ y_2 \\ \vdots \\ y_n \end{pmatrix} \quad (4)$$

The Zernike coefficients c_j can be found by solving (Eq.5).

$$c = (\mathbf{M})^{-1}y \quad (5)$$

After having estimated coefficients, the image in the reciprocal plane is multiplied by $e^{-i\Phi}$ phase to correct the aberrations.

The second regularization used in this paper is based on direct wavefront reconstruction from the gradient, without solving the linear equation. The respective shifts are first normalized (divided by the number of pixels in the subaperture) and then multiplied by πNx , where Nx is the size in pixels of the wavefront we wish to reconstruct, interpolated in both directions to acquire smooth function and integrated numerically [24].

4.3. Choice of the reference image

The shifts are measured from the cross-correlation between two images reconstructed from subapertures. As a result, shifts are known up to a constant, which depends on the shift of the reference image. Since the linear terms in the wavefront function do not blur the image, the choice of the constant does not compromise the resolution of the output. The use of the central subaperture as the reference image [11] is advantageous because it usually holds the best-resolved

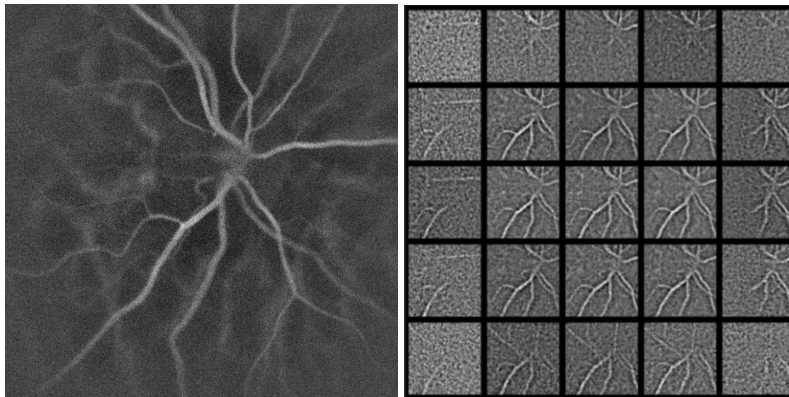


Fig. 5. Images of a optic never head of a volunteer calculated from the entire pupil (left) and from subapertures in the pupil (right), where the position of the image corresponds to the position and size of the subaperture in the pupil plane.

image. Alternatively, [17] proposed cross-correlating randomly chosen subapertures which increased both the stability and the performance of the aberration measurement. However this approach cannot be easily applied to LDH as the angular composition is not homogeneous across the field of view (Fig. 5). As a result, two randomly chosen subapertures do not necessarily have enough features in common to allow for the unequivocal shift assessment. To avoid the cross-correlation being driven by the numerical artefacts that appear due to this effect, the subimages are cropped to the central part. The margin applied is chosen empirically and depends on the propagation distance. Typically the margin is adapted to make sure that the extension of features visible is similar for all subimages.

Alternatively, we propose the use of the original image resized to the dimensions of the subapertures as the reference image. The respective shifts can then be assessed for all subimages including the central one. This choice is motivated by a strong speckle pattern that appears in subapertures due to the fully coherent illumination. As this speckle pattern changes from one subimage to another, it can jeopardize the measurement of the respective shifts. Furthermore, choosing the resized image as the reference can be seen as setting the average gradient as a reference zero level, which ensures that there is no tip or tilt component in the aberration wavefront. Such a component would have no impact on the results if the regularization basis were perfectly orthogonal, but discretization through the system of subapertures introduces a spurious cross-talk between the modes.

5. Results

5.1. Measurement of a numerically imposed aberration using Zernike regularization method

The LDH is used to image the optic nerve head of a volunteer. Experimental procedures adhered to the tenets of the Declaration of Helsinki, and the study was approved by an ethical committee (Comité de Protection des Personnes; clinical trial NCT04129021). Written informed consent was obtained from the subject. During reconstruction, the field in the Fourier plane is multiplied by a known phase function, which represents a linear combination of rank 2nd and 3rd of Zernike polynomials with randomly chosen coefficients. Consequently the wavefront distortion is measured using the algorithm described in section 4. Employment of both reference images is considered. The shifts are measured for 7 x 7 subapertures, and the wavefront estimated is projected onto Zernike polynomials from 2nd to 3rd degree. In Fig. 6 we compare the ground

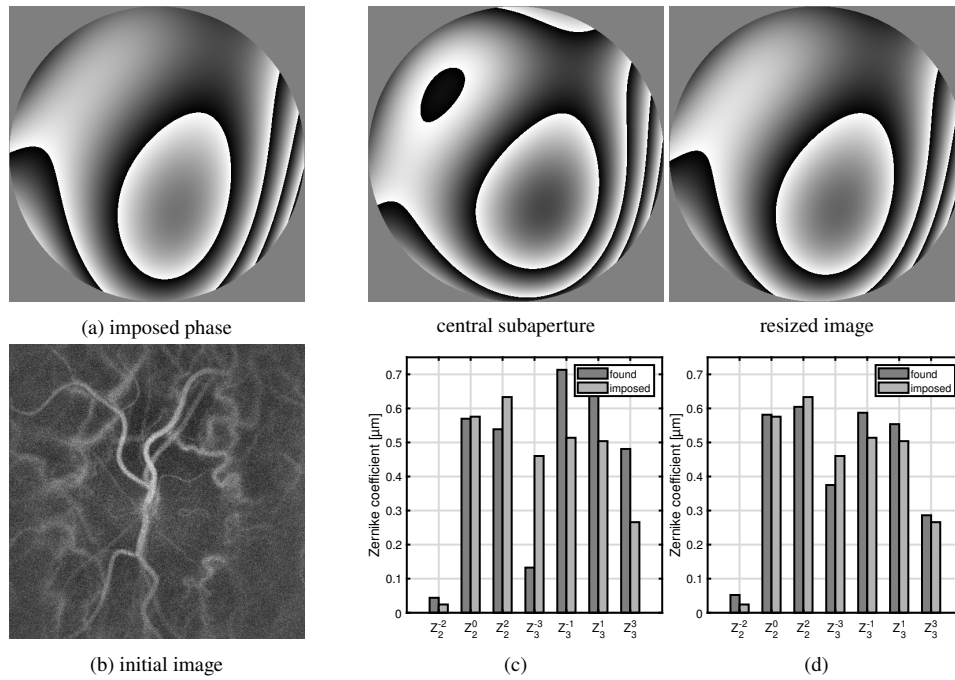


Fig. 6. Wavefront distortion imposed (Fig. 6a) and found using subaperture correlation based algorithm with central subaperture (Fig. 6c) and resized image (Fig. 6d) used as the reference. Below, associated Zernike coefficients are plotted.

truth with the results obtained. To quantify the error of the wavefront estimation we calculate the RMS of Zernike coefficients for the imposed and residual phases. Using the central subaperture as the reference image enables decreasing of initial RMS of $1.73 \mu\text{m}$ to $0.44 \mu\text{m}$ (which corresponds to 26% of the initial value), whereas with the resized image used as a reference one obtains the final phase of RMS $0.25 \mu\text{m}$ (15% of the initial phase).

5.2. Typical astigmatism correction for laser Doppler images with Zernike regularization approach

The impact of aberration compensation on the images reconstructed is investigated. Wavefront distortion is induced by placing a lens with 1.25 D astigmatism in front of volunteer's eye, which mimics the case in which aberrations are not circular functions perfectly inscribed in the field of view in the pupil plane. No additional aberration is added numerically. As previously the wavefront distortion is estimated in the reconstruction process using the numerical Shack-Hartmann algorithm, with the resized image used as a reference image. The field in the Fourier plane is split into 7×7 subapertures, and the wavefront estimate is projected onto Zernike polynomials from 2nd to 3rd degree. To compare the resolutions obtained for videos rendered with and without employing aberration correction algorithm, all frames calculated are averaged and a profile of the intensity along the line running through a region where two vessels run very closely to one another is plotted (Fig. 7). In addition, the influence of the resolution on the temporal signal is evaluated by comparison between two vessels of different sizes. The aberration correction technique allowed to considerably increase the contrast of the image calculated and, as a result, it facilitated the distinction of capillary vessels. There is no striking difference between the pulses detected.

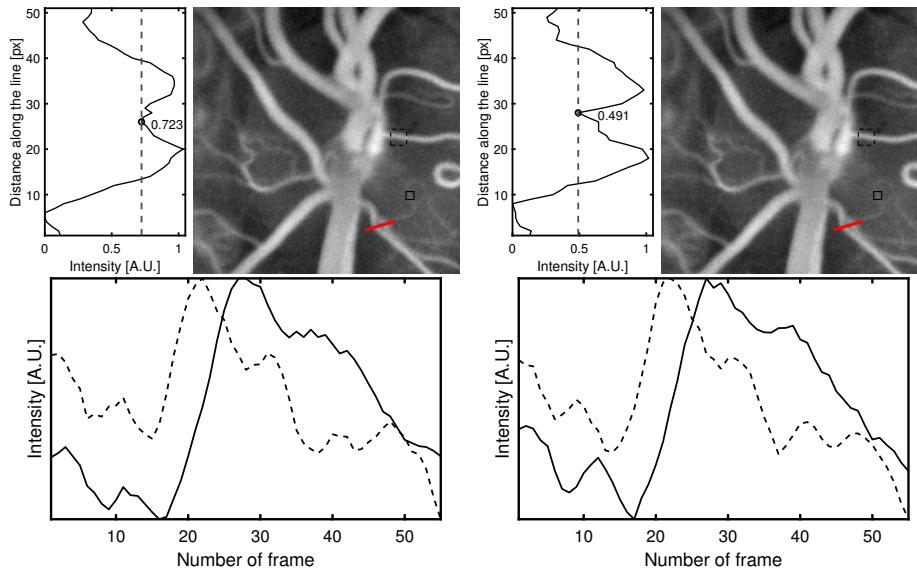


Fig. 7. Images of a optic nerve head of a volunteer taken with a cylindrical lens of 1.25 D power placed in front of the eye, without (left) and with (right) numerical Shack-Hartmann aberration correction applied. On the left side of the images, the intensity profiles along the red lines are represented. To quantify the contrast, the ratio between the local minimum and the averaged value of the two peaks is calculated. Plots below the images represent the average temporal signals corresponding to the regions marked with dashed and continuous lines respectively.

5.3. Comparison of aberration correction robustness for different reference images and regularization techniques

5.3.1. Numerically imposed aberration

Gradient integration and Zernike regularization methods are employed to reconstruct aberration numerically imposed on a batch of interferograms recorded with LDH and measured with the digital Shack-Hartmann algorithm. The distortion phase is constructed from Zernike polynomials of 2nd and 3th rank with coefficients chosen randomly between -1 and $1 \mu\text{m}$. For both techniques two possible reference images - central subaperture and resized full-pupil image - were tested during the assessments of shifts in subapertures. The comparison is done through estimation of the residual phase and its variance. Prior to these calculations, tilt and tip components - which have no influence on the resolution of the image obtained but can appear with the gradient integration approach - were subtracted. Immediate observation can be made that the gradient integration method with central subaperture used as a reference fails to correctly assess the aberration phase, however it manages to do so with resized image used as a reference Fig. 8. The Zernike regularization performs considerably better than the gradient integration approach. The observation from the Section 5.1 suggesting that the use of resized image as a reference improves the results has been confirmed. In this case the variance of the residual phase was 21% lower than that obtained using the central subaperture.

5.3.2. Physically imposed aberration

In the subsequent experiment a 6 D astigmatism lens was placed in front of the volunteer's eye. The field in the Fourier plane is split into 10×10 subapertures, and the wavefront estimate is projected onto Zernike polynomials from 2nd to 5th degree. In total 18 coefficients are

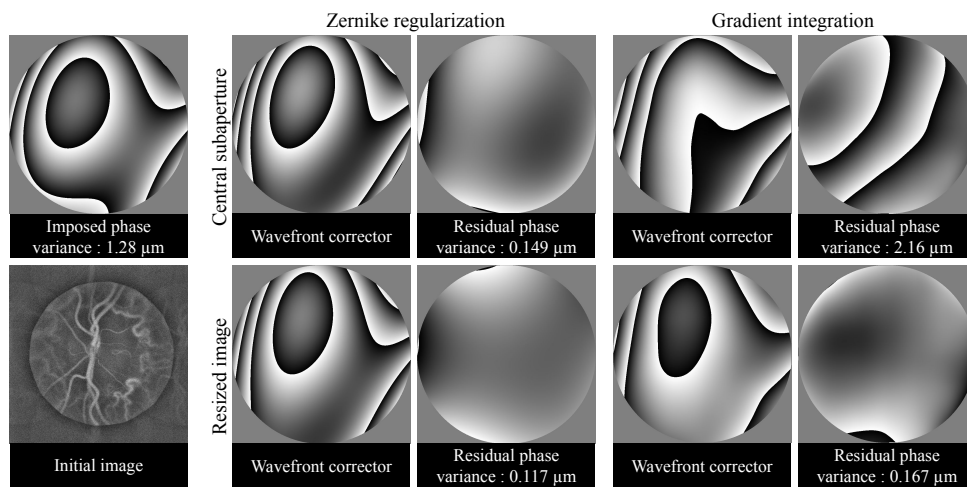


Fig. 8. On a batch of interferograms allowing to obtain an image of the ONH of a volunteer (initial image) a numerical aberration is applied (imposed phase). Shifts between subimages are assessed with central subaperture or resized image used as a reference. Zernike regularization and gradient integration techniques are compared. For four combination possible we represent both wavefront corrector and residual phase with its variance.

determined. The comparison between employing a central subaperture and the entire image resized as a reference image in the context of both regularization methods is illustrated in Fig. 9. For both regularization techniques, the use of resized image as a reference image helped reveal capillaries. The same criteria as in the section above are used to evaluate the resolution obtained for both the averaged image and the temporal signal measured. The two vessels are most easily distinguished for direct gradient integration wavefront reconstruction, with resized image used as a reference. For the Zernike regularization technique, the use of central subaperture as reference resulted in slightly better contrast, however the velocity profiles across the vessels seems overly noisy. For the temporal signals we can see that, once again, the direct gradient integration wavefront reconstruction, with resized image used as a reference, provided the best results. It is the only pulse profile for which the dicrotic notch can be detected for the smaller vessel.

5.3.3. Physically imposed aberration with low stability

So far, the configurations with perfect alignment between the aberrating lens and the optical paths have been considered. However, this model is frequently inadequate when imaging the human eye, as the patient moves and aberrations induced are not perfectly radially symmetrical. To mimic the above problems, a volunteer is asked to hold a 6D astigmatism lens in front of his/her eye. The wavefront is reconstructed, like previously, using the subaperture correlation technique. The shifts were estimated over 7×7 subapertures, using resized image as reference. The effectiveness of wavefront reconstruction through projection on the Zernike basis of 2nd order and direct gradient integration are compared. Two acquisitions are considered, images integrated over the total number of frames available are illustrated in Fig. 10. First video consists of 85 and the second of 100 frames. The duration of the measurement was determined by the time over which the subject was capable of focusing vision on one point. As one can see, imposing 6D astigmatism blurs the image of the optic nerve head reconstructed at an adapted focal depth (Fig. 10a,d) and hinders the visualisation of capillary vessels. Generally, aberration

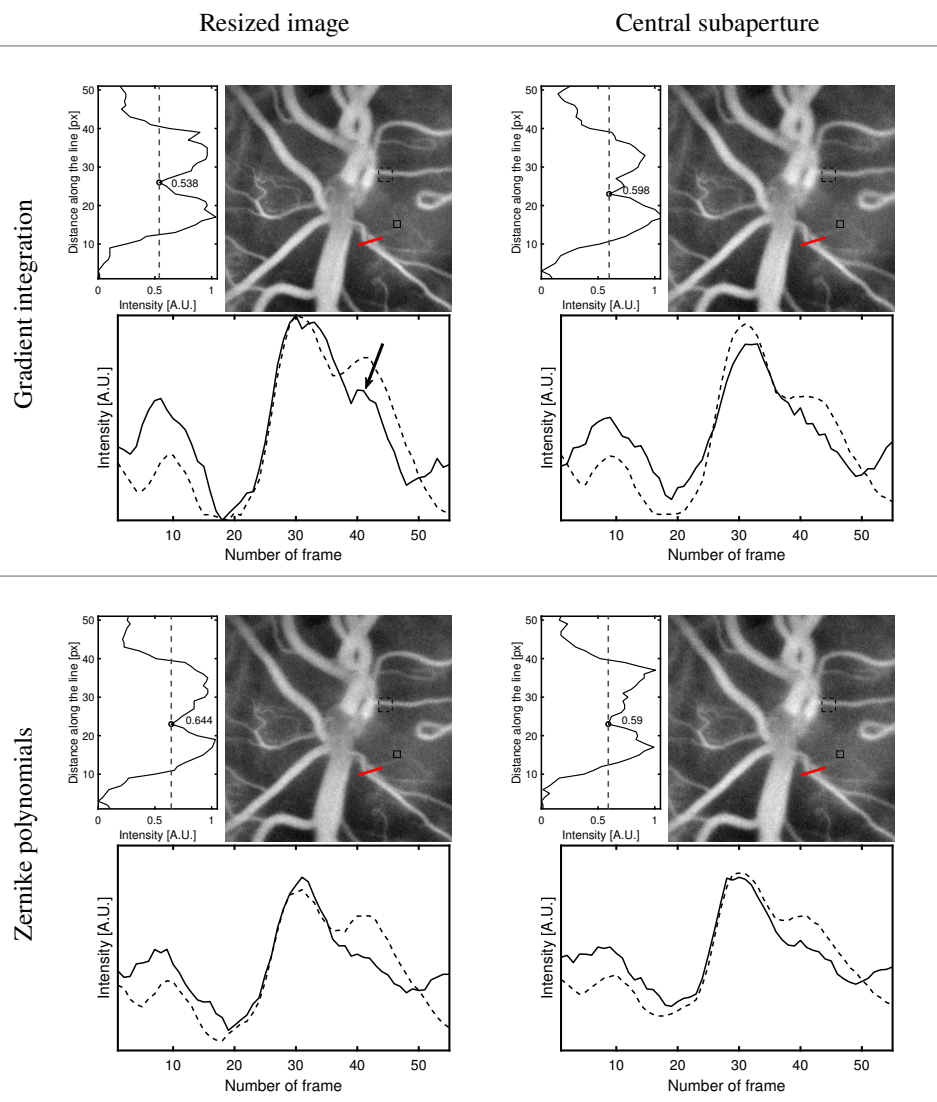


Fig. 9. A comparison of close-up LDH images of a ONH of a volunteer reconstructed with numerical Shack-Hartmann aberration correction, for various regularization and shift assessment techniques. The profiles on the left side of the images correspond to the intensity profiles along the red lines indicated in the pictures. Plots below the images represent the average temporal signals corresponding to the regions marked with dashed and continuous lines respectively. An arrow in the top left pulse plot points to the dicrotic notch visible in the micro-vasculature pulsation waveform.

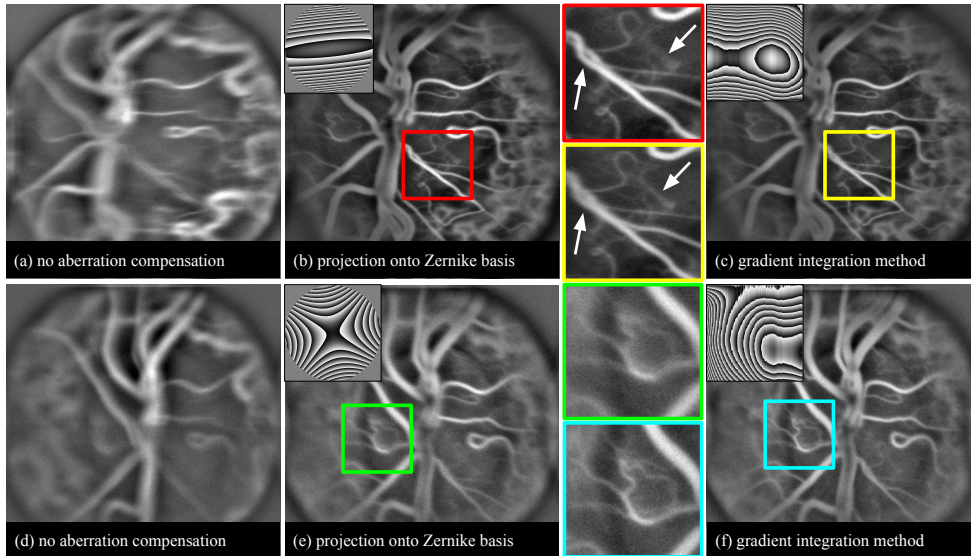


Fig. 10. Doppler holographic images of the papillary region of the retina in a volunteer who holds an astigmatism 6D lens in front of his/her eye. The experiment is repeated twice (a, d). During image reconstruction we apply numerical Shack-Hartmann algorithm to measure aberration wavefront. In images (b, e) wavefront is projected on the Zernike polynomial basis, in (c, f) it is reconstructed using gradient integration technique. Images represented above are averaged over multiple frames of a video.

compensation with regularization through the Zernike polynomials increases the resolution of the image, but its effectiveness varies between measurements (Fig. 10b,e). Gradient integration technique, on the other hand, allows to repeatedly obtain images with high resolution (Fig. 10c,f). The main difference between these two sets of data lies in the symmetry of the wavefront to be detected as shown in the inserts in the figure. In the first case (top), the aberrations are equally well approximated by symmetrical Zernike polynomials and direct gradient integration. The difference between the two results (Fig. 10b,c) lies in various resolutions for superficial and deeper vessels. In the second case (bottom), the wavefronts reconstructed by the two techniques differ clearly.

6. Discussion and conclusions

This paper studies the deployment of aberration correction from subaperture image analysis for the LDH imaging of the human eye fundus. This technique consists principally of measuring the distorted wavefront in a discrete basis and regularizing it, in such a way that it represents a continuous function. Each of these steps can be adequately optimized and adapted to the imaging technique applied, which was the aim of this study.

One of the primary challenges met in deploying wavefront measurement from subaperture image analysis in digital holography is the varying angular composition of points across the field of view and the speckle pattern that emerges in images reconstructed from subapertures due to highly coherent illumination. To address this issue, we proposed to crop the subimages used for calculating cross-correlation function and use a resized full-pupil image as a reference for shift assessment. This approach favours accurate measurements of subimage shifts, a crucial first step in applying subaperture-based digital adaptive optics to laser Doppler imaging techniques. The study also compared regularization with Zernike polynomials and direct gradient integration

approaches for the continuous wavefront reconstruction.

To begin with, the digital Shack-Hartmann algorithm was validated as a method for wavefront measurement for the LDH, as it correctly measured numerically imposed aberrations. Subsequently, it was observed that typical astigmatism (1.5 D) correction using the numerical Shack-Hartmann method with the Zernike regularization approach improved the resolution of the images obtained, but it has no significant impact on the temporal signal measured. The comparison of performance for the regularization and the gradient integration approach was conducted in three steps. Reconstructions of numerically imposed aberrations suggested that the Zernike regularization method performs far better than the gradient integration technique. For both wavefront reconstruction methods, resized images used as a reference performed better than the central subaperture. In the second step, videos were distorted with a 6 D astigmatism lens placed in front of the volunteer's eye. The comparison between four possible combinations revealed that only the gradient integration technique with a resized image used as a reference allows the detection of the dicrotic notch in the microvasculature pulsation, which was visible in less distorted images. The difference between those results and the numerical experiment is probably caused by the fact that digitally imposed aberrations, constructed from the exact Zernike functions on which the wavefront is projected, create a bias towards the regularization approach.

Finally we studied a system where imposed aberrations are non-symmetrical and unstable in time. This allowed to mimic a configuration in which the optical axis of the eye and the setup are not aligned and subject struggles with fixation. In such a case, the wavefront reconstruction through gradient integration can perform considerably better, due to the higher degree of freedom and a higher stability of the measurement. In the Zernike regularization approach, the precision of shift measurements over each subaperture is critical; a single inaccurate measurement can compromise the entire wavefront reconstruction. Conversely, with gradient integration, an erroneous shift assessment in one subaperture remains a localised issue, thus preserving the overall accuracy of the wavefront reconstruction and minimising impact on image sharpness. It is possible that the effect of aberration correction is additionally enhanced by the registration algorithm, which performs better on sharper images.

In conclusion, we have seen that subaperture correlation based digital adaptive optics can be adapted to LDH allowing for better contrast and resolution in images obtained. Furthermore, we propose for the first time the use of resized full-pupil image as a reference instead of using one or multiple subapertures, which limits the error of the aberration estimation. In this study, we also compared two wavefront reconstruction methods, namely Zernike regularization and gradient integration, showing that the latter performs better in terms of resolution obtained for the case of LDH.

Funding

This work has received support under the program « Investissements d'Avenir » launched by the French Government.

Acknowledgments

Authors would like to thank Vincent Borderie and Pedro Mecê for revision and helpful comments.

Disclosures

The authors declare no conflicts of interest.

Data Availability

Online repository for image rendering and aberration compensation routines : [Holowaves\(17df875\)](https://doi.org/10.1101/17df875).
Data used for this paper can be shared upon request.

References

1. H. Hashemi, A. Fotouhi, A. Yekta, *et al.*, “Global and regional estimates of prevalence of refractive errors: Systematic review and meta-analysis.” *Curr Ophthalmol* **30**, 3–22 (2018).
2. J. F. Castejón-Mochón, N. López-Gil, A. Benito, and P. Artal, “Ocular wave-front aberration statistics in a normal young population,” *Vis. Res.* **42**, 1611–17 (2002).
3. A. Roorda, F. Romero-Borja, W. Donnelly-III, *et al.*, “Adaptive optics scanning laser ophthalmoscopy,” *Opt Express* **10**, 405–12 (2002).
4. J. Liang, D. Williams, and D. Miller, “Supernormal vision and high-resolution retinal imaging through adaptive optics,” *J Opt Soc Am A Opt Image Sci Vis* **14**, 2884–92 (1997).
5. B. Hermann, E. Fernández, A. Unterhuber, *et al.*, “Adaptive-optics ultrahigh-resolution optical coherence tomography,” *Opt Lett* **29**, 2142–4 (2004).
6. J. I. W. Morgan, T. Y. P. Chui, and K. Grieve, “Twenty-five years of clinical applications using adaptive optics ophthalmoscopy [Invited],” *Biomed. Opt. Express* **14**, 387 (2023).
7. D. R. Williams, S. A. Burns, D. T. Miller, and A. Roorda, “Evolution of adaptive optics retinal imaging [Invited],” *Biomed. Opt. Express* **14**, 1307 (2023).
8. K. M. Hampson, R. Turcotte, D. T. Miller, *et al.*, “Adaptive optics for high-resolution imaging,” *Nat. Rev. Methods Primers* **1**, 68 (2021).
9. C. Liu, X. Yu, and M. K. Kim, “Phase aberration correction by correlation in digital holographic adaptive optics,” *Appl. optics* **52**, 2940–49 (2013).
10. C. Liu, D. Thapa, , and X. Yao, “Digital adaptive optics confocal microscopy based on iterative retrieval of optical aberration from a guidestar hologram,” *Opt. express* **25**, 8223–36 (2017).
11. A. Kumar, W. Drexler, , and R. A. Leitgeb, “Subaperture correlation based digital adaptive optics for full field optical coherence tomography,” *Opt. express* **21**, 10850–66 (2013).
12. L. Ginner, A. Kumar, D. Fechtig, *et al.*, “Noniterative digital aberration correction for cellular resolution retinal optical coherence tomography in vivo,” *Optica* **4**, 924–31 (2017).
13. L. Ginner, T. Schmoll, A. Kumar, *et al.*, “Holographic line field en-face oct with digital adaptive optics in the retina in vivo,” *Biomed. Opt. Express* **9**, 472–485 (2018).
14. S. Hubmer, E. Sherina, R. Ramlau, *et al.*, “Subaperture-based digital aberration correction for optical coherence tomography: A novel mathematical approach,” *SIAM J. on Imaging Sci.* **16**, 1857–1885 (2023).
15. D. Hillmann, H. Spahr, C. Hain, *et al.*, “Aberration-free volumetric high-speed imaging of in vivo retina,” *Sci. Reports* **6**, 35209– (2016).
16. H. Sudkamp, D. Hillmann, P. Koch, *et al.*, “Simple approach for aberration-corrected oct imaging of the human retina,” *Opt. letters* **43**, 4224–4227 (2018).
17. D. Hillmann, C. Pfäffle, H. Spahr, *et al.*, “Computational adaptive optics for optical coherence tomography using multiple randomized subaperture correlations,” *Opt. Lett.* **44**, 3905 (2019).
18. L. Puyo, M. Paques, M. Fink, *et al.*, “In vivo laser doppler holography of the human retina,” *Biomed. Opt. Express* **9**, 4113–4129 (2018).
19. L. Ginner, A. Kumar, D. Fechtig, *et al.*, “Noniterative digital aberration correction for cellular resolution retinal optical coherence tomography in vivo,” *Optica* **4**, 924 (2017).
20. S. Hubmer, E. Sherina, R. Ramlau, *et al.*, “Subaperture-based digital aberration correction for optical coherence tomography: A novel mathematical approach,” *SIAM J. on Imaging Sci.* **16**, 1857–1885 (2023).
21. Z. Bratasz, O. Martinache, Y. Blazy, *et al.*, “Diffuse laser illumination for maxwellian view doppler holography of the retina,” Preprint arXiv:2212.13347.
22. D. Valente, K. V. Vienola, R. J. Zawadzki, and R. S. Jonnal, “Kilohertz retinal FF-SS-OCT and flood imaging with hardware-based adaptive optics,” *Biomed. Opt. Express* **11**, 5995 (2020).
23. L. Puyo, M. Paques, and M. Atlan, “Spatio-temporal filtering in laser doppler holography for retinal blood flow imaging,” *Biomed. Opt. Express* **11**, 3274–3287 (2020).
24. J. D’Errico, “Inverse (integrated) gradient,” MATLAB Cent. File Exch. (2024).

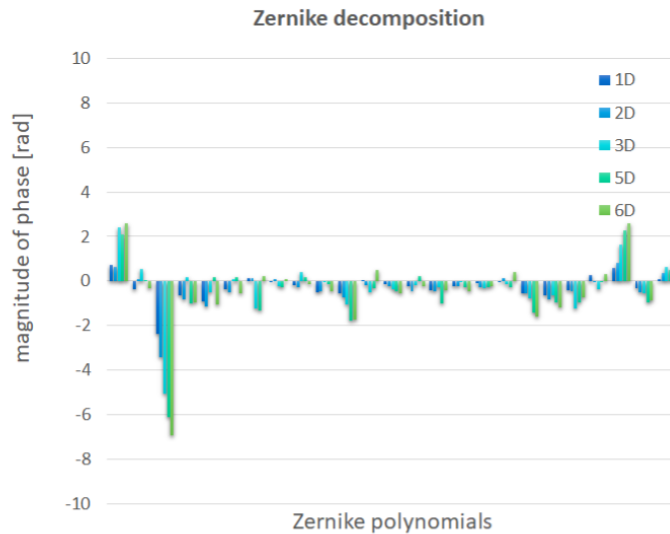


Figure 2.7: For images with imposed increasing astigmatism from 1 to 6 dioptres measured aberrations decomposed on ranks from 2 to 6 of zernike polynomials. On the right shifts were calculated using central subaperture, on the left the new technique.

2.3 Aberration measurements validation and sources of errors

The main mean of validating the aberration measurement accuracy through verifying that it allows ameliorating the resolution of images obtained. However, additional tests were conducted in the first stage of work on aberration compensation, which preceded the study presented in the article above. The results obtained allowed us to understand the limitations and sources of error in the method employed.

Firstly, a series of measurements, in which lenses with increasing power of astigmatism were consecutively placed in front of the volunteer's eye, was carried out. Aberrations measured were projected on 2nd - 6th rank of Zernike polynomials. Fig. 2.7 illustrates the level of Zernike coefficients found. Immediate observation can be made that other Zernike polynomials, than those imposed, have been detected in the aberrations measured. The presence of residual higher-order aberrations in itself would not be surprising given object image can induce aberrations which are being added to the ones imposed. However, it can be observed that some coefficients increase with the magnitude of astigmatism imposed which suggests that there is a coupling between them, which should not be observed in an orthogonal basis.

To understand this effect better, let us describe in greater detail how the projection basis is calculated. A chosen Zernike polynomial is inscribed in a square image, with the values outside the circular function given a constant value of 0. This image is divided into a number of subapertures, denoted n , over which the gradient is calculated (Fig. 2.8). The subapertures whose centers do not belong to the disc are rejected. The average gradient value is calculated over the subaperture, and then scaled to correspond to a shift in the direct space. In subapertures containing the borders of the disc, the phase function is discontinuous and hence its derivative will yield to outliers, which must be

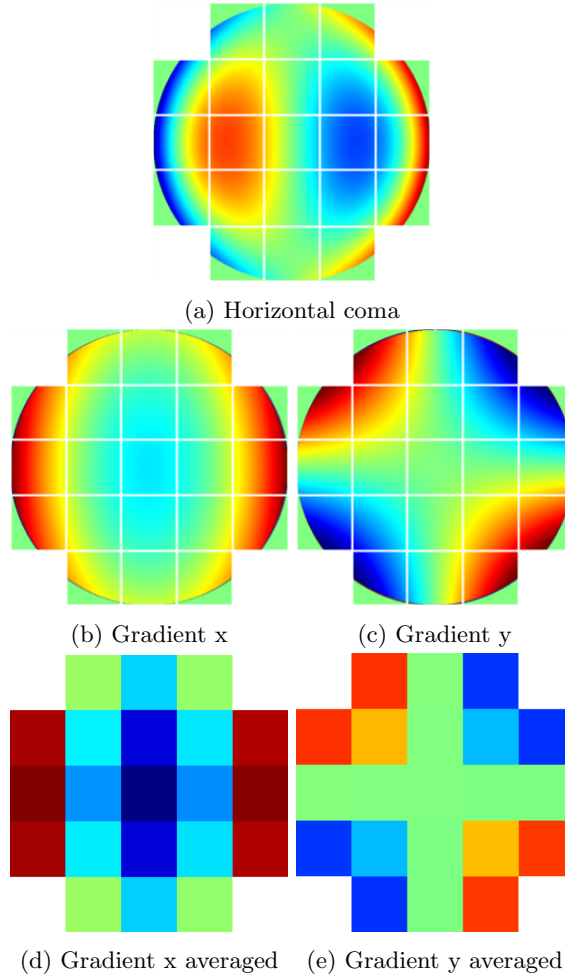


Figure 2.8: Visualisation of processing applied to calculate the \mathbf{M} matrix. We start with one of the Zernike polynomials in the basis and we subdivide it into a number of subapertures (a). Over each of the a gradient in x (b) and y (c) direction is calculated. The maps obtained are averaged over each subaperture (d,e). The values at the borders of the circle are not taken into consideration.

rejected. The procedure enables obtaining a vector of shifts, describing given Zernike polynomial in the new basis. The processing is repeated for all p Zernike polynomials chosen. All vectors obtained are assembled to form a matrix of projection denoted \mathbf{M} .

$$\mathbf{M} = \begin{pmatrix} m_{11} & m_{12} & \cdots & m_{1p} \\ m_{21} & m_{22} & \cdots & m_{2p} \\ \vdots & \vdots & \ddots & \vdots \\ m_{n1} & m_{n2} & \cdots & m_{np} \end{pmatrix} \quad (2.1)$$

It should be kept in mind that the shifts are measured in directions x and y, and the two should be treated independently. In the case being analysed, the vectors of shifts in the x and y directions

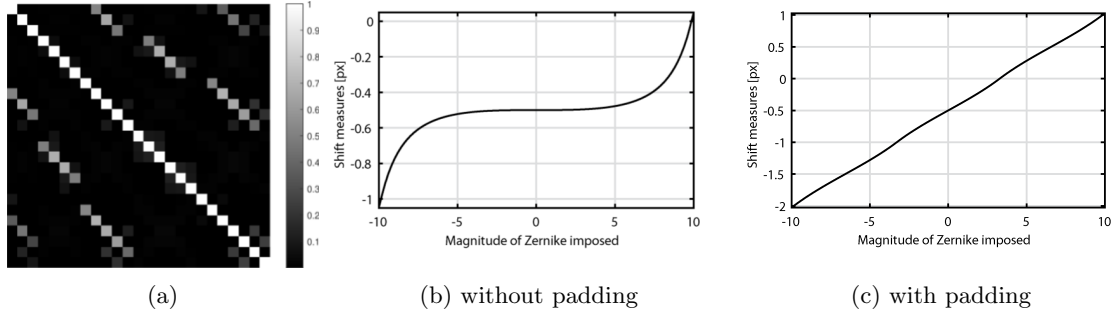


Figure 2.9: (a) Covariance matrix for Eq.2.2. Each vector was normalized so that the values on the diagonal are unitary. (b,c) Shift measured as a function of slope of the phase in the pupil.

were concatenated.

$$\mathbf{M} = \begin{pmatrix} m_{11}^x & m_{12}^x & \cdots & m_{1p}^x \\ \vdots & \vdots & \ddots & \vdots \\ m_{n1}^x & m_{n2}^x & \cdots & m_{np}^x \\ m_{11}^y & m_{12}^y & \cdots & m_{1p}^y \\ \vdots & \vdots & \ddots & \vdots \\ m_{n1}^y & m_{n2}^y & \cdots & m_{np}^y \end{pmatrix} = \begin{pmatrix} m'_{11} & m'_{12} & \cdots & m'_{1p} \\ \vdots & \vdots & \ddots & \vdots \\ m'_{n1} & m'_{n2} & \cdots & m'_{np} \\ m'_{(n+1)1} & m'_{(n+1)2} & \cdots & m'_{(n+1)p} \\ \vdots & \vdots & \ddots & \vdots \\ m'_{2n1} & m'_{2n2} & \cdots & m'_{2np} \end{pmatrix} \quad (2.2)$$

To verify the orthogonality of the projection basis we calculate the covariance of transition matrix between the shifts and the Zernike polynomials basis. Care should be taken to the normalization of the basis vectors, before the calculations.

$$\mathbf{C}_{ij} = \sum_{k=1}^{2n} m'_{ik} m'_{jk} \quad (2.3)$$

The covariance matrix is calculated for Zernike polynomials up to 6th rank. The field of view is divided into 12 subapertures. The result obtained is represented in the Fig. 2.9a. One can see that the matrix is not perfectly diagonal, which would be the case for a fully orthogonal basis. In theory the number of sampling points respecting the Nyquist condition should be sufficient for the correct representation of the basis. However, this is not what we observe. One of the explanations for this issue is the transition from polar to Cartesian coordinate system might be the source of error. Alternatively, it is possible that the error in Zernike coefficients arises from the shift assessment on the data itself. One should notice here that the performance of the algorithm relies on the principle that the shift in the subimage varies linearly with the slope of the phase in the corresponding subaperture. A numerical experiment, in which a tilt phase with varying slope was numerically propagated to assess the shift of the focal point. The Fig. 2.9b illustrates the dependency obtained which is clearly not linear. To alleviate this error one can apply padding in the Fourier space which can ensure the linear dependency of between the two (Fig. 2.9c). One can see that the oscillation in the function found are still present but their amplitude is low enough to consider that they have no impact on the results.

2.4 Aberrometry

2.4.1 Astigmatism quantification

Numerical Shack-Hartmann algorithm can be equally employed to conduct aberrometric measurements using LDH. To begin with, we would like to verify whether LDH allows to correctly quantify the level of the aberrations. The simplest aberration to add would be defocus, as it can be correctly characterised even if the effective pupil in LDH is very small. However imposing defocus in LDH only changes the effective reconstruction distance which can also vary with patient's movement and eyepiece to camera distance. To avoid this coupling, but at the same time profit from independence of the pupil size we opt for the astigmatism as aberration to impose. A cylindrical lens was used to induce wavefront distortion, which was then measured using the numerical Shack-Hartmann algorithm. The Zernike coefficients obtained were subsequently compared with the ground truth. Let us take a meridian of astigmatism phase and represent it with a parabolic function $y(x) = ax^2$. The focal power is then equal to $P = 4a$.

$$P = 4a = \frac{2c_f\lambda}{\pi x^2} \quad (2.4)$$

Where λ is the wavelength, c_f is coefficient found, and x is the pupil half size, which can be calculated from magnification of the eyepiece used and the angular acceptance of the pixels. It is worth noting here that this formula differs with the normalization type chosen. Here, we have considered that the Zernike functions are normalized with respect to its maximum value. We have conducted two experiments in which we change the eyepiece (lens of 100 mm and doublet of 60 mm lenses) and the size of the effective pupil, as well as the magnitude of aberration imposed (1.25 and 6 D). The results obtained were represented in the Table 2.10.

Lens focal length [mm]	100		33.5	
Effective pupil radius [mm]	1.52		0.51	
Astigmatism imposed [D]	1.25	6	1.25	6
Z_2^{-2}	0.8816	-6.255	0.676	0.5754
Z_2^0	-1.9876	-0.8839	-2.7119	-1.3692
Z_2^2	-4.0668	5.8696	0.1638	3.2786
Total astigmatism	4.161	8.578	0.696	3.329
Astigmatism power found [D]	1.00	2.07	1.45	6.95

Figure 2.10: Table summarizing the results of aberration quantification. For two focal lengths of eyepiece used, an astigmatism of 1.25 D and 6 D was imposed. From Zernike coefficients found numerically the resulting magnitudes were calculated using Eq. 2.4.

The estimation of astigmatism power with the lens doublet (33.5 mm effective focal length) seems to be rather correct, even if for both magnitudes of astigmatism imposed the estimation is 16% higher than expected. On the other hand, for the lens of 100 mm the estimations are lower than expected. Especially for the astigmatism of 6 D the estimation is 3 times smaller than the real value.

The error in the results can arise from one of the two estimations : of the pupil size or of the Zernike coefficient. The issue with these estimations might result from the fact that cylindrical lens imposes not only astigmatism but also defocus. Effectively, it acts like a spherical lens with astigmatism added. This is not a problem in terms of astigmatism estimation but it certainly is

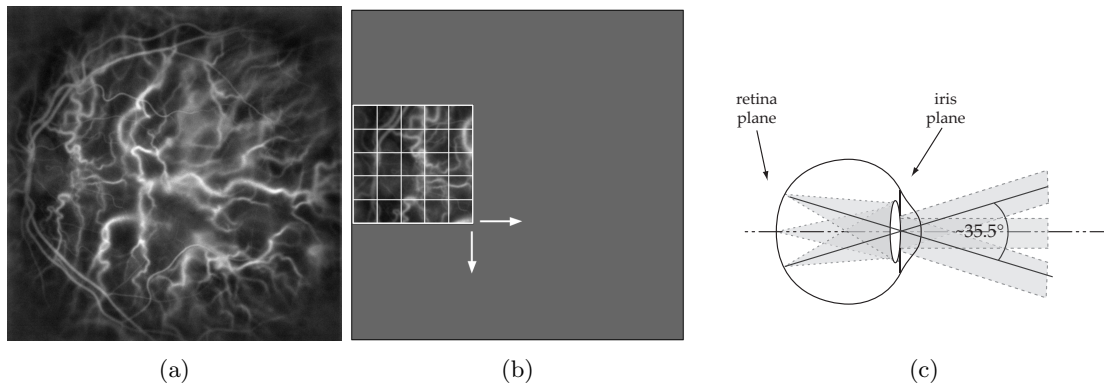


Figure 2.11: A numerical Shack-Hartmann can be performed on a reduced zone of reconstructed image, which introduces an angular dependency of zernike coefficients found. Peripheral measurement configuration the field is $\sim 35^\circ$ (Fig. 2.11c). For images with important field of view (Fig. 2.11a), with 768×768 pix, it is possible to subdivide the initial image (windows of 256×256 pix) and to measure how the average aberrations change with the varying mean angle of incidence, by sliding the window of interest (Fig. 2.11b).

an issue for pupil size assessment. Moreover, as the exact position of the lens is not known, it is impossible to calculate the resulting pupil size. In the future, it would be advantageous to place an additional spherical lens which will compensate for the effect of cylindrical lens and ensure that astigmatism is the only aberration added.

2.4.2 Peripheral aberrations

So far we have concentrated our study on the on-axis aberrations as they have the highest importance for the quality and comfort of vision in daily tasks, and, as a result, are of the highest clinical importance. Nevertheless, in the recent years the peripheral aberrations have been linked to conditions such as retinal detachment and their impact on eye health begins to be investigated [59]. To measure peripheral aberrations using LDH we profit from the maximal extension of the field of view at the retina. A sub-image stack is chosen from the entire field in the retina plane, before the frequency integration. On this sub-image we perform the usual numerical Shack-Hartmann processing to obtain a Zernike coefficient of interest. This procedure is repeated for different positions of the sub-image. As the size of sub-image has to remain relatively large for a sufficient SNR to be obtained, it can be advantageous to introduce an overlap between the areas of interest (Fig. 2.11). Finally, we represent a value of each Zernike coefficient as a function of the position of sub-image centre. Fig. 2.12 represents the Zernike coefficients maps obtained from a wide-field image of the volunteer's macula. We considered 2nd and 3rd rank of Zernike polynomials. We can clearly see that the maps of coefficients for the second order resemble the Zernike polynomials which they assess. For higher order functions it seems to also be the case although the general tendencies are less easily identified. The interpretation of these results remains challenging. The coefficient that seems the easiest to understand is defocus, as we expect that its value corresponds to the mismatch of focal and retina planes.

To verify this hypothesis, we conduct a “calibration” experiment. We glue a card with black and white pattern onto a moving stage, which allows sample rotation with respect to the axis perpendicular to the optical axis of the instrument. The angle between the two is varied between

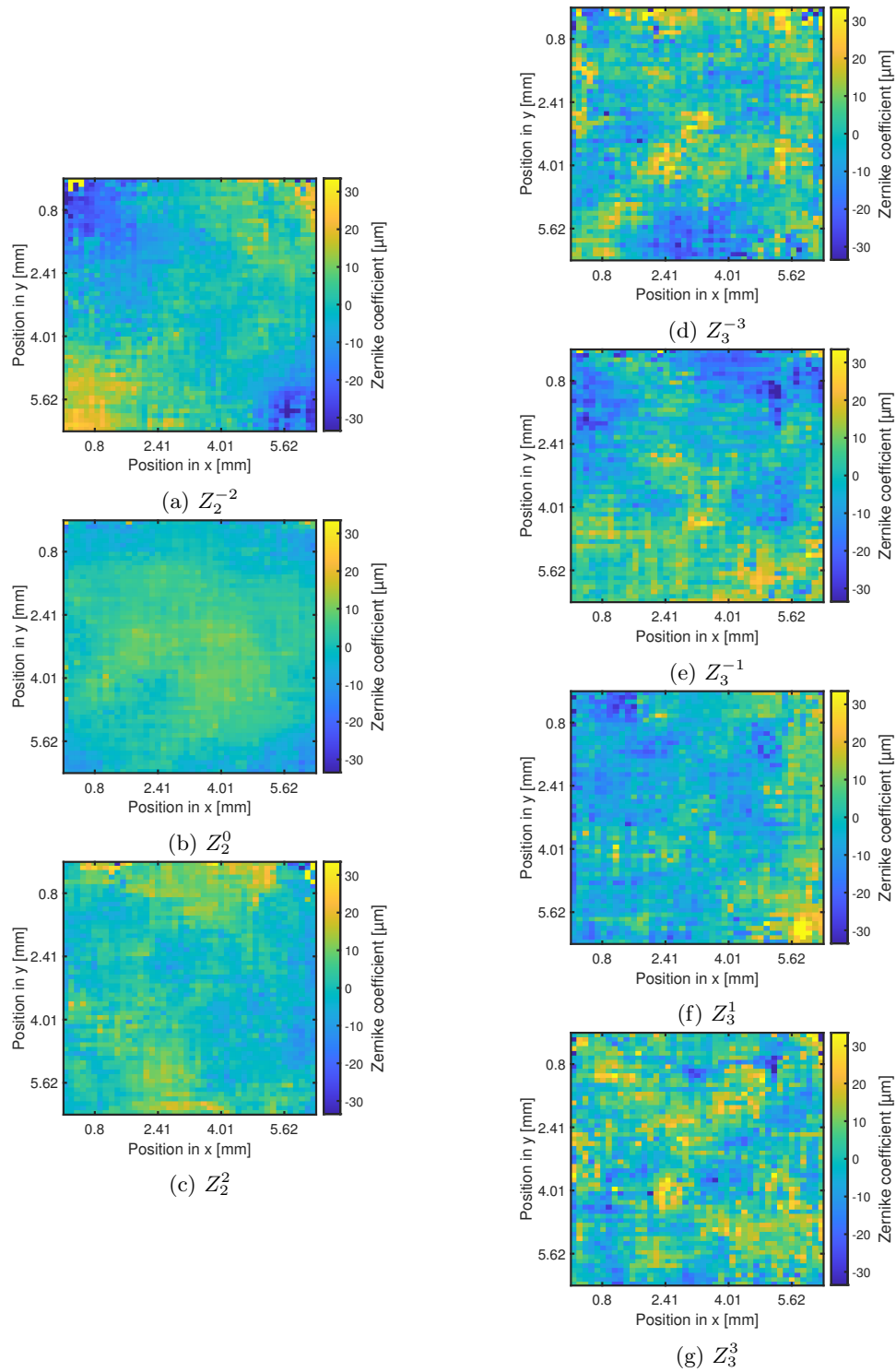


Figure 2.12: Respective Zernike polynomials (2nd and 3rd rank) coefficients represented as a function of subimage position.

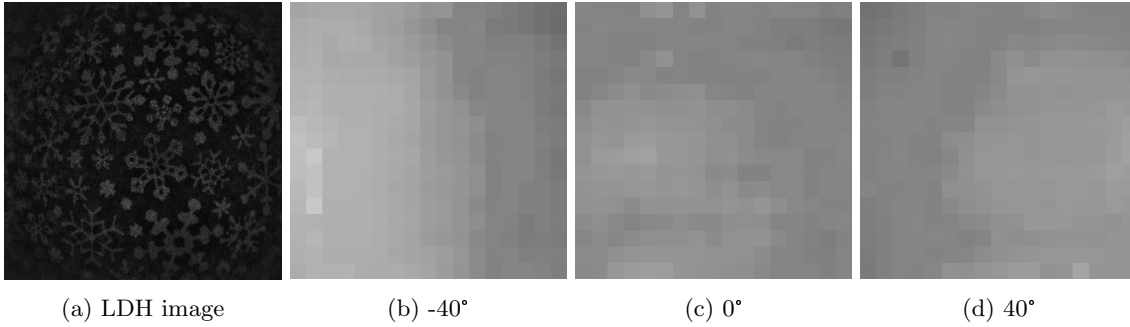


Figure 2.13: A card with black and white pattern is imaged using laser Doppler holography (2.13a) with different angles between the image plane and optical axis. In the reconstruction phase peripheral defocus measurement is performed. Obtained coefficient maps were represented for tilt of -40° (2.13b), 0° (2.13c) and 40° (2.13d)

-40° to 40° every 10° . Additionally, the card fixation enables rotation of the image with respect to the optical axis. Small angle rotations during the acquisition induce a Doppler shift detectable with LDH yet slow enough not to blur the image. Finally, the propagation distance was chosen at $z = 0.45$ to match the reconstruction distance for the human retina in the previous experiment. For each position the measurements are performed twice.

The image reconstructions indicates that the lens doublet distorts the image and gives an impression of a curvature. The map of defocus for 0° reveals that the focal plane of the system is curved (Fig. 2.13). To quantify the tilt measured with the Zernike coefficient map we project the defocus maps onto the Zernike basis and we consider the value of tilt. The values obtained were plotted as a function of angle imposed (Fig. 2.14). The dependency between the two is almost linear, although it seems that function flattens around the extreme values of tilt, which might be caused by the reduced precision of the measurements.

In conclusion, the experiment confirmed that the value of defocus corresponds to the mismatch between the focal and object planes. Nonetheless, it is possible that the resemblance between the Zernike polynomials and the Zernike coefficient maps which we measure for peripheral aberrations is an artefact. One of the constraints that we have not taken into account while conducting this experiment is the inhomogeneous angular composition of each part of the image which has been so far ignored. In this situation, a real deformation of wavefront is partially masked.

2.5 Conclusions

In this chapter we have first discussed multiple techniques that can be employed to compensate for the ocular aberrations in retinal imaging. Due to the dynamic nature of distortions present in the eye their compensation requires adaptive optics (AO) strategies, which can be either hardware-based (HAO) or computational (CAO). HAO is indispensible for the techniques with low coherence, where aberrated photons cannot be detected due to coherence gating. For this reason the hardware-based approach cannot be fully replaced by its computational version. In the case of LDH, the coherence length is very high and the aberrations do not induce problems with the detection. As a result, it seems favorable to profit from the holographic detection scheme and employ CAO.

Alternatively, AO systems can be grouped into techniques which do or do not employ wavefront

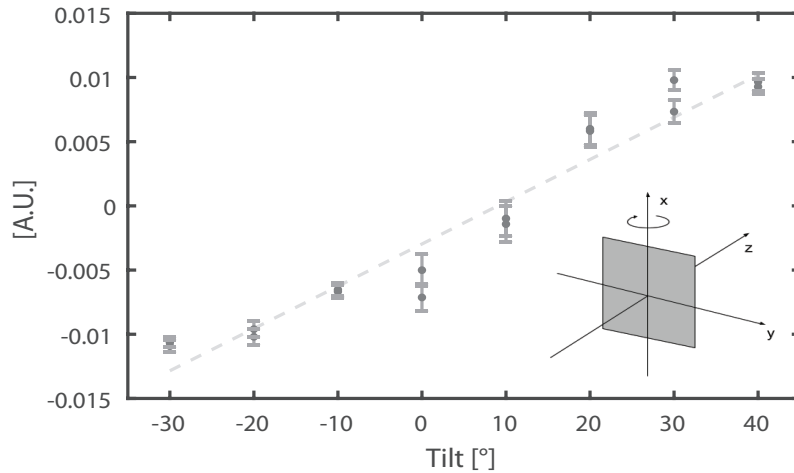


Figure 2.14: The slope of the variation of the defocus coefficient over the field of view is represented as a function of tilt imposed to the calibration card. For the calibration measurements card is tilted around x axis to introduce defocus diversity. The doppler shift is induced by a rotation around z axis

sensing. The main advantage of employing wavefront sensing is time efficiency, and its main drawback is the inherent limitation of the “resolution” - that is the number of corrected modes. Conversely, sensorless approaches can, in principle, compensate for as many modes as desired, but they require long computation time. In the scope of this thesis, we have opted for wavefront-sensing, numerical approach, as the correction of higher-order aberrations has relatively low impact on the resolution of the LDH images.

The study presented in the article “Aberration compensation in Doppler holography of the human eye fundus by sub-aperture signal correlation” proved that numerical Shack-Hartmann can be successfully adapted to LDH to improve the image quality. A novel reference image was proposed as an answer to the specific issue of inhomogeneous angular composition of different parts of the image in LDH and two wavefront reconstruction techniques - Zernike polynomials regularization and gradient integration - were investigated.

Some limitations of the numerical Shack-Hartmann approach are due to the low SNR of the imaging technique used. These limitations can be addressed by improving the detection system. However, other limitations are inherent to the Shack-Hartmann technique itself. For example, there is an uncertainty relationship between the size of the subaperture and the precision of the slope assessment; smaller subapertures may increase spatial resolution but reduce the accuracy of slope measurements, and vice versa. Another inherent limitation arises from the coupling between vectors in the regularization basis. While this coupling may not affect the quality of reconstructed images, it poses a challenge in aberrometry, where the Shack-Hartmann and Zernike regularization bases are commonly used.

The use of LDH for aberrometric measurements was considered. Preliminary tests comparing quantified Zernike coefficients measured with the aberrations imposed were conducted. Strong discrepancies between the expected and found values suggest that estimation of the pupil size in the presence of aberrations is inaccurate. Additionally, we performed preliminary measurements of the

peripheral aberrations. Interpretation of the results remains unclear for the moment. In general, LDH is not the best adapted technique for the aberrometric measurements as the effective pupil size is very small compared with the human pupil. However it allows for a very large field-of-view which offers a unique opportunity for the peripheral vision assessment and it would be interesting to investigate this subject further.

Chapter 3

Quantitative estimation of blood flow

3.1 Introduction

As mentioned in the introduction, LDH is a promising device for blood flow quantification. It has been previously demonstrated that the signal detected enables qualitative estimation of the blood flow velocity through Doppler broadening. Nonetheless, blood flow was never expressed in terms of absolute values, and a model linking the detected signal to flow velocity was not developed. The aim of this chapter is to describe existing blood flow measurement techniques, position LDH with respect to them and discuss the model I proposed for blood flow quantification.

3.2 State of the art

3.2.1 Color Doppler Imaging (CDI)

CDI is an ultrasound technique based on Doppler shift measurement (Fig. 3.1). Currently, it is the most widely used method for blood flow imaging in clinical practice, allowing for the precise assessment of blood flow direction and velocity in major arteries, veins, and the heart. Its main advantage is that it enables blood flow imaging through opaque media, however, it has a relatively low spatial resolution and limited range of blood flow velocities it can measure [60]. CDI is equally a valuable tool in ophthalmology, enabling detailed assessment of blood flow in key retrobulbar vessels, including the ophthalmic artery, central retinal artery, and short posterior ciliary arteries [9]. During the examination, the probe is placed on a closed eyelid, as contact with the tissue is required. CDI has been employed for first estimation of multiple biomarkers, which were introduced in the Chapter 1: peak systolic velocity (PSV), end-diastolic velocity (EDV), mean velocity (MV), the resistivity index (RI), and the pulsatility index (PI).

3.2.2 Laser Doppler Velocimetry (LDV) and Laser Doppler Flowmetry (LDF)

Laser Doppler velocimetry (LDV) is one of the earliest approaches employing light source for blood flow measurement [32]. The proposed optical setup captures signals from the laser beam backscat-

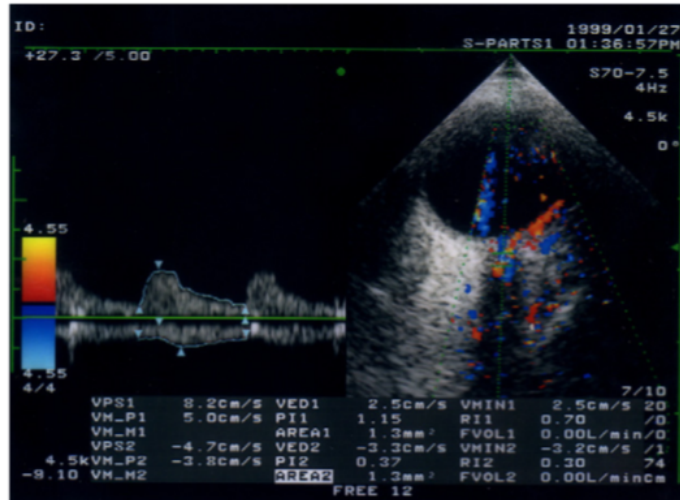


Figure 3.1: Figure adapted from [9] representing a typical result of color Doppler imaging in the eye. The eye fundus is represented in cross section. The color scale combined the information about the absolute value and direction of the flow. The red to yellow color scale is for the flow directed toward the detector, the blue to white - away from it.

tered by moving particles in the sample, which are then combined with a reference beam. The Doppler shift causes a frequency detuning between these beams, leading to intensity flickering in the detected signal. By analyzing the spectrum of this signal, the frequency shift due to the Doppler effect can be determined. The extent of Doppler broadening depends on the angle between the particle velocity and the difference in incidence and scattered wave vectors. Challenges in estimating these directions can be addressed by using a bidirectional configuration, where two backscattered light signals are recorded at known angles to accurately measure the Doppler shift [61] (Fig. 3.2). As a result, the dependency on the absolute values of the incidence and scattering angles is alleviated. In LDV the measurements are typically taken at a single point, but by incorporating scanning techniques, it is possible to generate 2D velocity maps.

In recent years, the authors of [62] proposed combining LDV with adaptive optics (AO) fundus camera, which enables precise positioning of the laser's focal spot and thus improves the resolution of the local velocity maps. One of the limitations of this technique is a relatively low temporal resolution (approximately 10 fps) due to its single-point measurement approach. Additionally, since the LDV pathway cannot be used simultaneously as the adaptive optics (AO) pathway, the system is rather complex and demands precise alignment, which restricts its practicality in clinical settings.

Laser Doppler Flowmetry (LDF) is another laser-based technique for blood flow measurements, similar to LDV in its principle (Fig. 3.3). The difference with LDV lies in the fact that in the LDF optical setup, the scattered light is not combined with the reference beam but rather the flickering results from the mixing of signals from static and moving scatterers, which effectively acts as a reference arm [63].

In a paper by Chauhan et al. from 2006, the authors evaluate the capacities of LDF to visualize and measure the temporal signal in the capillary vessels of the rat retina and compare it with results obtained using fluorescein isothiocyanate-dextran angiograms [64]. The SLDF (scanning - LDF) images were obtained using a commercial instrument - Heidelberg Retina Flowmeter (HRF;

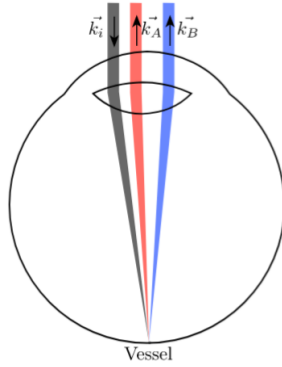


Figure 3.2: Figure adapted from [62] illustrating the bidirectional configuration which alleviates the need for scattering angle determination in blood flow measurement through Doppler effect.

Heidelberg Engineering GmbH, Dossenheim, Germany). The authors conclude that the precision of LDF is limited and does not enable the visualization of capillary vessels.

3.2.3 Doppler OCT

The potential of using OCT for blood flow measurements was first demonstrated with time-domain OCT in the 1990s, shortly after the technique's introduction [65]. The signal recorded in time-domain OCT is modulated by the frequency shift caused by the axial velocity of the reflective surface in the reference arm. If scattering objects within the sample also exhibit axial movement, this will alter the frequency of the light backscattered from the sample. Consequently, the modulating frequency changes, reflecting the velocity difference between the sample and reference beams. To extract the local sample velocity, a sliding-window Fourier transform can be applied to the modulated signal.

The real breakthrough, however, arrived with Fourier-domain OCT (FD-OCT) systems, which enabled phase-sensitive measurements with a high frame rate [66]. As a result, the phase changes can be followed in time. The velocity can be written as:

$$v(z) = \frac{\Delta\varphi(z, T)}{T \cos(\alpha)} \frac{\lambda}{4\pi} \quad (3.1)$$

where $\Delta\varphi(z, T)$ is the phase difference between two consecutive frames separated by interval T and α is the angle between the incident beam wave vector and movement direction. One can see that unambiguous velocity measurement necessitates that the $\Delta\varphi$ belongs to the $[-\pi, \pi]$ interval, which puts an upper limit on velocities this technique can measure. The minimum velocity which can be measured, on the other hand, is defined by the phase fluctuation amplitude. The values estimated, as for the other techniques, depend on the angle of incidence. Similarly to LDV, this problem was approached by bidirectional configuration. A review paper by Leitgeb et al. provides a valuable overview of various techniques that have been developed to combine optical coherence tomography (OCT) with local velocity measurements within the sample using the Doppler shift effect [67].

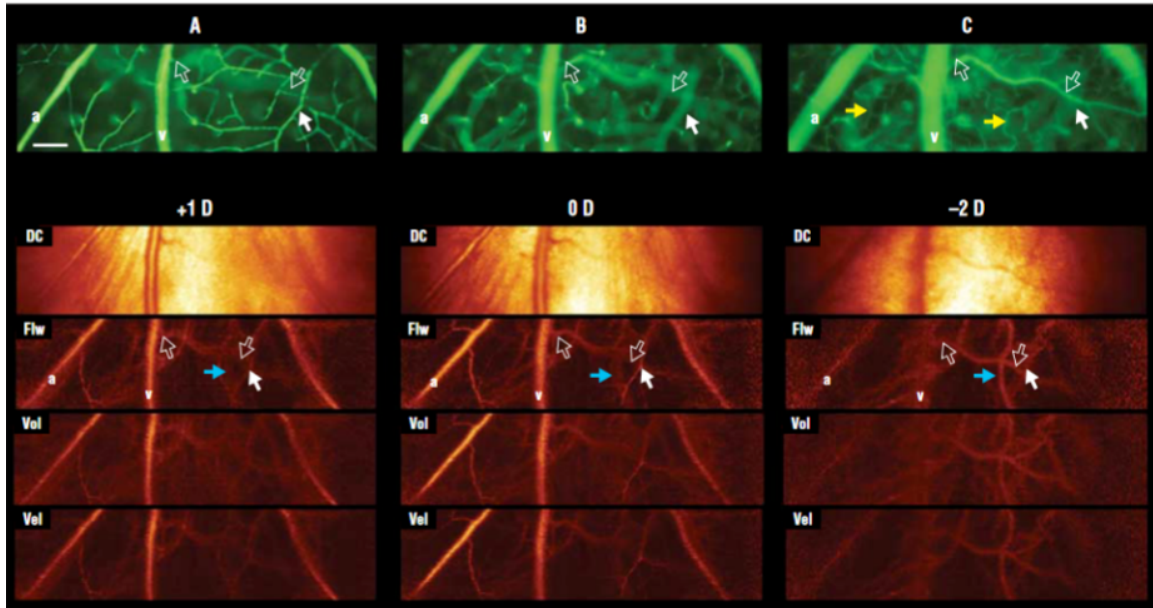


Figure 3.3: Figure adapted from [64] comparing laser Doppler flowmetry (red-orange colormap) with FITC - contrast agent based fluorescence microscopy (green colormap) - for different layers in the eye.

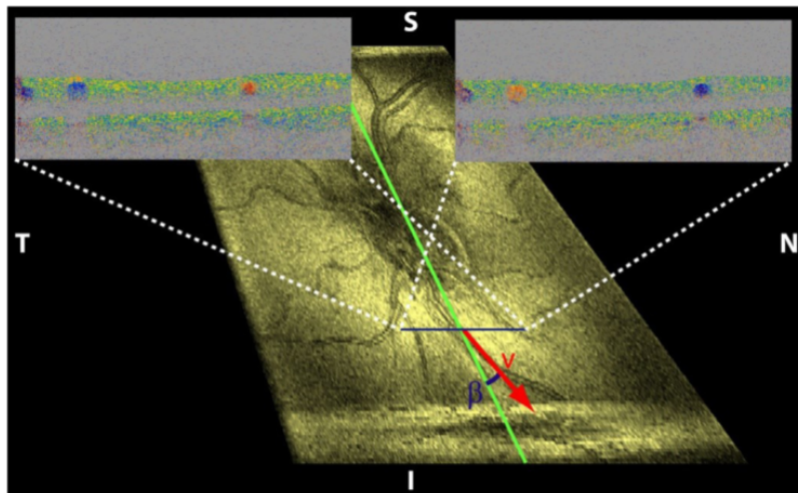


Figure 3.4: Figure adapted from [67] illustrating the Doppler OCT blood-flow measurements in bi-directional configuration. Two cross-sections were measured with beams arriving at the detection plane with different angles, which modifies the contrast in the vessels observed.

3.2.4 Proposition of Laser Doppler holography relative to other techniques

The challenge in validating new retinal blood flow imaging devices stems from the absence of a universally accepted gold-standard technique for measuring retinal blood flow. Current methods can be categorized into two main groups: those utilizing the Doppler effect and those that track displacement across consecutive frames. Determining which approach holds greater promise remains difficult. Unlike other Doppler-based devices, LDH (Laser Doppler Holography) uniquely measures the Doppler effect in transmission by using a highly coherent light source. This can enhance sensitivity, as the majority of photons interacting with red blood cells are forward scattered. However, this also complicates quantification due to the lack of an established model for this specific configuration. Additionally, LDH does not offer axial sectioning, and strong multiple scattering can hinder measurements in capillary vessels. Despite these challenges, the system's primary advantage is its ultra-high temporal resolution combined with the ability to capture a large field of view.

3.3 Segmentation

The first step in blood flow quantification consists of segmenting the vessels in the images obtained. As discussed in the previous Chapters, blood flow quantification requires calculating the difference between the spectra in the vessels and in the background [37]. For that purpose, we first conduct a segmentation aiming at the localization of main retinal arteries and veins. The algorithm proposed is based partially on an existing vessel extraction method called Frangi segmentation [68], which enables identification of vessel-like structures. It also incorporates specific properties unique to our problem, as detailed below.

- The overall signal in LDH is dominated by the temporal trace of the arteries, thus cross-correlating the signal averaged over the entire field of view with that of each pixel allows for first segmentation of the arteries, which is later improved (Fig. 3.5b). This processing can be applied iteratively.
- Retinal vessels are, almost always, connected to the ONH, which is easily identified using the *M1* image (detailed below). This condition can be employed to discard any artefacts, which could appear due to strong choroidal signal. The exact processing applied consists of smoothing the *M1* image with a Gaussian filter, finding the coordinates of maxima in the intensity distribution, taking the previously obtained mask, and adding a disc of a chosen size centered at the coordinates found. Finally, a function which enables extraction of the largest area of connected points can be applied (Fig. 3.5d). As a result, every "vessel" which is connected to the disc will remain in the mask, and those which are not are discarded.

The existing algorithm for vessel segmentation is a result of my joint work with other PhD students: Yohan Blazy, Olivier Martinache, and Baptiste Fontaine, who was an intern I co-supervised. It begins with calculating the vessel masks using Frangi segmentation. The signal from the vessels is extracted, averaged, and then cross-correlated with the temporal trace in each pixel. As the averaged signal is dominated by the arteries' contribution, identifying regions with the highest cross-correlation coefficient enables their identification. Finally, the parts of the choroid that remain or artifacts of aliasing are discarded using the connectivity with the center condition described above.

However, segmenting vessels using LDH measurements continues to present challenges. Some of the key issues that still persist include:

- Lack of distinction between separate vessels in the areas where they cross.

- The presence of choroidal vessels which seem connected to the center due to the crossing with retinal vessels.
- Difficulties in retrieving the full length of the vessel in situations where the signal diminishes due to the size of vessels and the illumination intensity distribution.
- A large number of adaptable parameters which influence the results obtained.

As a result, the algorithm, in its current form, is rather difficult to use as for each video the processing parameters need to be adapted. However, it is possible that once a large number of masks is obtained, it would be possible to apply machine learning algorithms, which could resolve existing problems. This approach will be explored in the work of next PhD students.

3.4 Statistics of Doppler effect and analysis of spectra

3.4.1 Introduction

As we have seen in the introduction, the angular frequency shift induced by scattering on a particle moving with velocity \vec{v} can be expressed as:

$$\Delta\omega = (\vec{k}_s - \vec{k}_i) \cdot \vec{v} \quad (3.2)$$

Where \vec{k}_i, \vec{k}_s correspond to the incident and scattered wave vectors. In the case of the human eye, the moving particles capable of inducing the Doppler effect are predominantly red blood cells (RBCs). The RBCs are disc-shaped with a diameter of 7.5 - 8.3 μm and a thickness of 1.7 - 2.2 μm . As these dimensions are comparable with the wavelength of the laser beam used, the scattering event can be described by the Mie model, which defines the probability distribution of an incident photon being deviated in a chosen direction (Fig. 3.7a). The typical angle of scattering for an 852 nm wavelength on RBCs is approximately 5°. For the purpose of the calculations presented here, we will use a simplified model in which the scattering angle varies between 0°- 5°, and all directions within these boundaries are equally probable.

We have also seen in Chapter 1 that the average photon returning from the eye has typically been scattered multiple times and has passed through all the eye's layers before its axial direction was reversed. As a result, the frequency of that photon has been altered multiple times. The totality of photons detected is characterized by the spectrum they form, which is measured through the Fourier transform of the detected interference signal. Let us discuss the evolution of that spectrum during beam propagation in the eye fundus (Fig. 3.8). For simplicity, we consider the initial frequency as the zero reference level.

The incident light is monochromatic, so its spectrum is highly peaked around 0. When traveling through the eye fundus, the spectrum broadens due to scattering on the red blood cells and the surrounding tissues, which are subject to natural eye movements. The majority of these events occurs below the retina, which is mostly transparent and has a relatively low concentration of vessels. Finally, the spectrum of the light impinging on the retina from the deeper layers is considerably broadened and relatively homogeneous, thanks to the presence of the highly scattering RPE layer covering the choroid. An exception to this occurs in areas with large choroidal vessels, where RBC velocities can be significantly higher. This is because resistance to blood flow scales with the fourth power of the vessel's radius, as we have seen in the Chapter 1. Consequently, the spectrum broadening in these regions can be much greater than in the rest of the choroid. Although the RPE layer blurs the signal, the vessels remain identifiable. Finally, the source of contrast in the

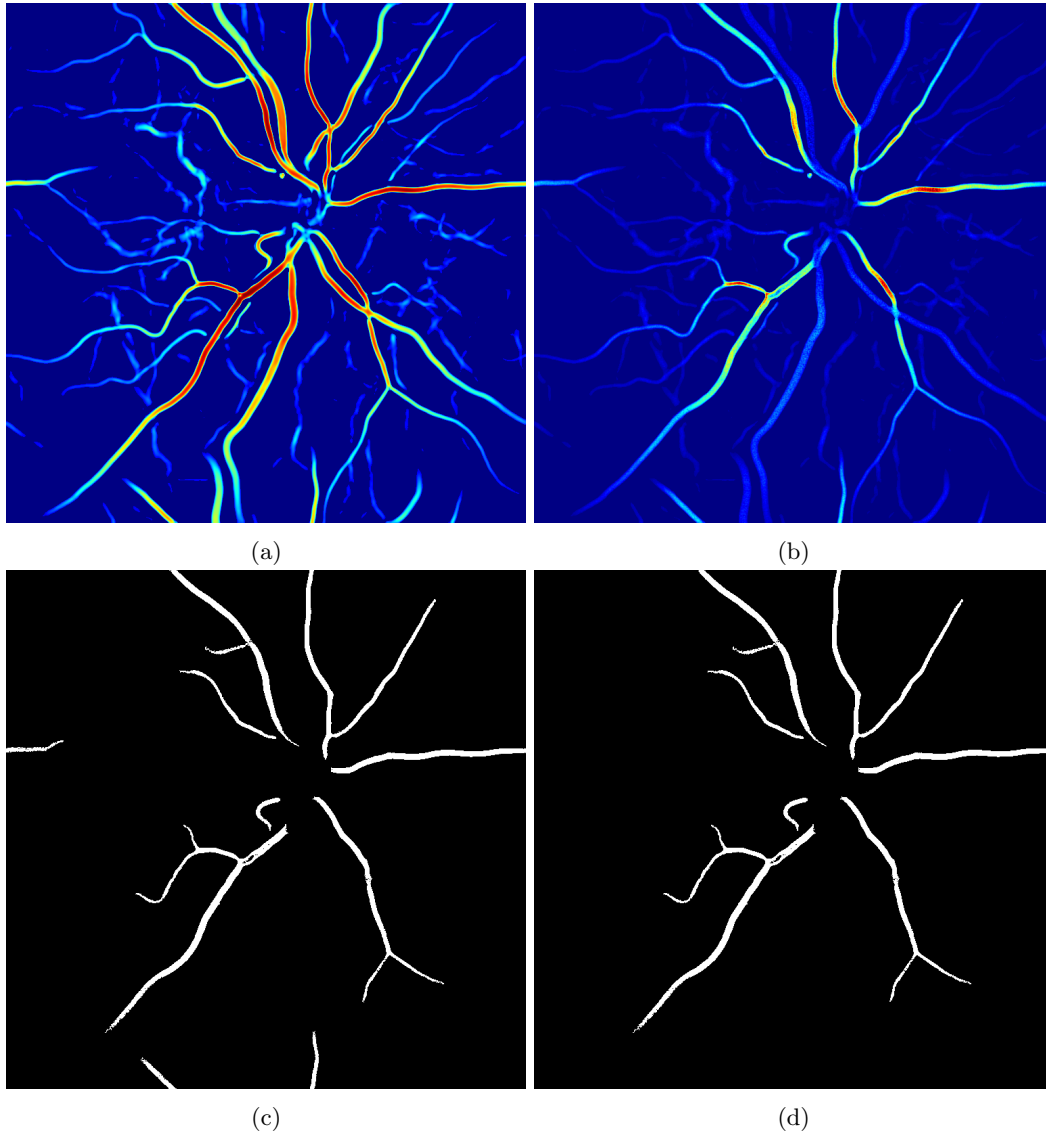


Figure 3.5: Major steps of segmentation processing. (a) Colour map representing the **vesselness** resulting from Frangi segmentation, (b) 2D map of normalized correlation factor between the approximated pulse and signal of each pixel, (c) mask obtain by applying an threshold to the (b), (d) previous masked cleaned using the property of being directly connected to the centre (defined as a region at a given distance from the ONH, which can be identified with M_1 image.)

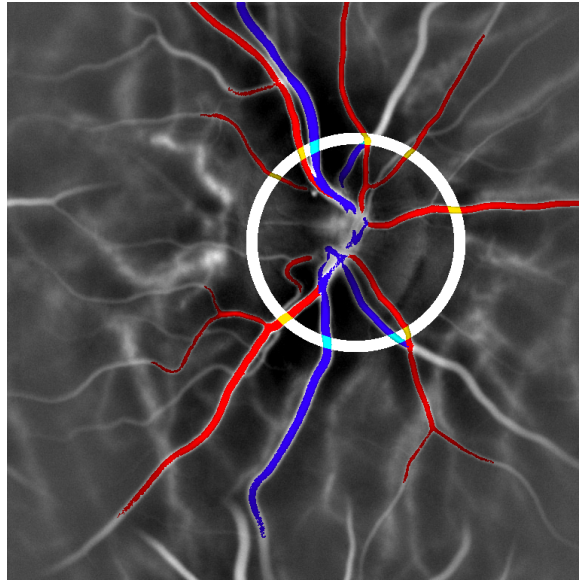


Figure 3.6: Result of vessels segmentation overlapped with power Doppler image of ONH with LDH, red - arteries, blue - veins. White circle is centred around the ONH and can be employed in further assessment of the total blood volume rate arriving in the retina.

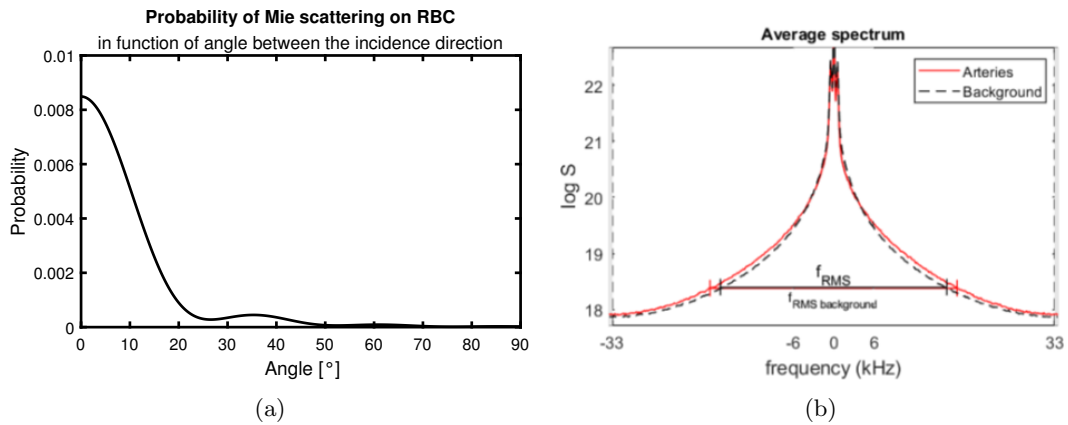


Figure 3.7: (a) Plot of probability of Mie scattering on the RBC in function of angle for 852 nm wavelength. (b) Spectrum in arteries and background measured on the LDH data with a sampling frequency of 67 kHz.

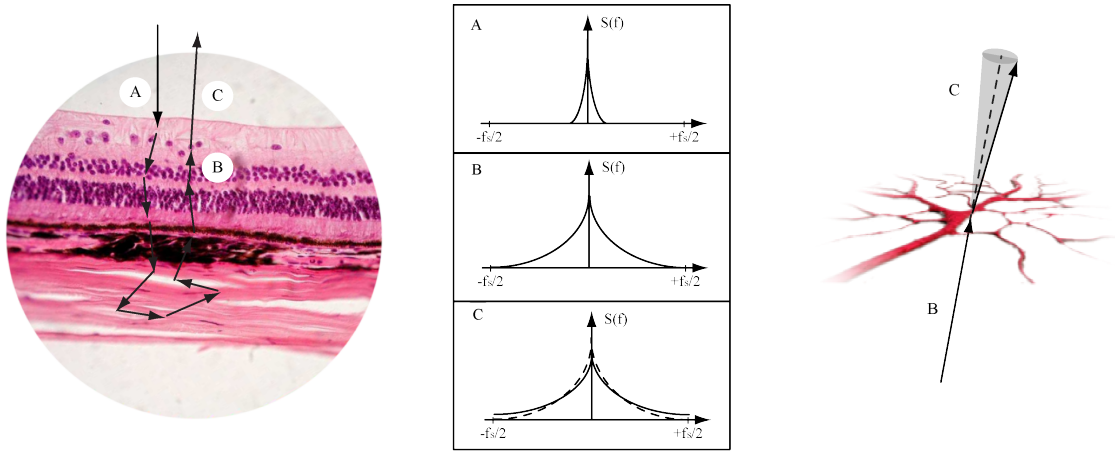


Figure 3.8: Left: retina cross section image by David Fankhauser, a schematic representation of photon scattered in the eye fundus, centre: a representation of spectrum of light: A - arriving at the retina, B - light impinging on the retina, backscattered by deeper layers. C - spectrum of B overlapped with that of light further broadened by scattering in the retina (dashed line). Right: schematic representation of Mie scattering at the vessels.

retina is the last scattering event, which induces a small perturbation to the spectrum (Fig. 3.7b). Quantification of the velocity of the RBCs requires subtraction of the background signal from the spectrum measured in the vessels and finding the correspondence between the frequency distribution and the velocity of scattering particles.

Typically, to quantify the information contained in the spectrum, the moments of the distribution are calculated. However, as mentioned in the Chapter 3, the detected signal mixes information about the sample and the reference arm, with the spectrum of the latter comprising the lowest frequencies. To eliminate its contribution, we must limit our analysis to the higher frequencies by choosing the integration limits f_1 and f_2 .

$$M_0 = \int_{-\infty}^{\infty} S(\omega) d\omega \quad (3.3)$$

$$M_1 = \int_{-\infty}^{\infty} \omega S(\omega) d\omega \quad (3.4)$$

$$M_2 = \int_{-\infty}^{\infty} \omega^2 S(\omega) d\omega \quad (3.5)$$

As suggested in the PhD thesis of Léo Puyo, M_0 can be seen as the total energy in a chosen frequency band [69]. Similarly, the moment M_1 corresponds to the average frequency of the signal. It is worth mentioning that M_1 here was employed in our work to measure the asymmetry of the spectrum, whereas in previous work it was used to assess the average frequency, and the sign of the shift was ignored. The asymmetry of the spectrum allows us to uniquely measure the velocity component parallel to the optical axis and thus can be employed to identify the out-of-plane vessels. Finally, moment M_2 can be employed to assess the variance of the spectrum.

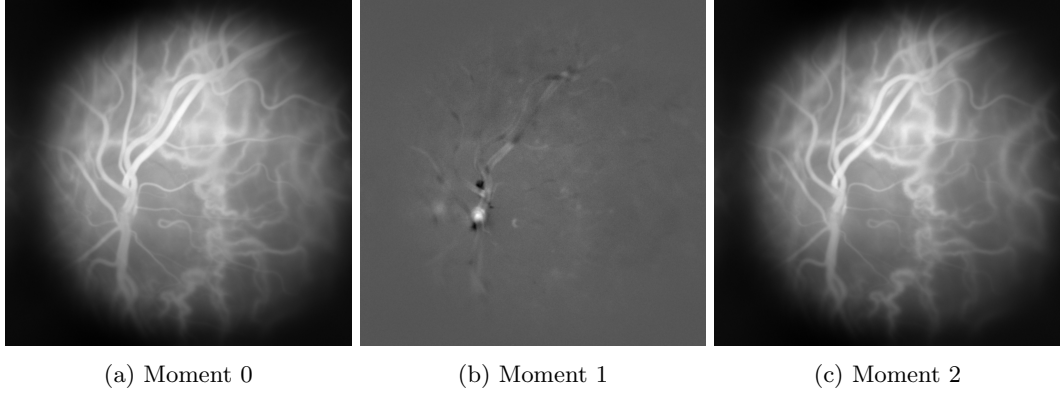


Figure 3.9: Average moment 0, 1 and 2 image obtained with laser Doppler holography, integrated over 6-33 kHz band.

In all previous works, the signal comprised in M_0 was considered proportional to the local velocity of RBC particles. As we apply a high-pass filter, we expect that the energy contained in the higher frequencies is positively correlated to the broadening induced. However, there is not theoretical evidence suggesting that M_0 in the upper frequency band is proportional to the velocity of RBCs. Moreover, M_0 is dependent on the overall energy of the signal, which varies across the field of view. For these reasons, it is important to search for another method of extracting information about the RBC velocities from the spectrum.

The images corresponding to each moment integrated between 6 and 33 kHz are represented in the Fig. 3.9. As mentioned above, the high-pass filter is applied to reject the image of the reference arm and static scatterers. As we can see, there is a strong correlation between M_0 and M_2 images. The M_1 image allows us to assess indirectly the angle of the vessels, given that it is correlated to the out-of-plane component of the velocity. However, determining the angle is not straightforward because the absolute velocity is unknown. Nevertheless, for a continuous vessel, we can estimate how its orientation varies. As observed, most retinal vessels are perpendicular to the optical axis, and from this point forward, they will be considered as such.

3.4.2 Scatterer velocity and the distribution of the frequency shift

To find the proportionality factor between the moments of the spectrum and the local velocity of scattering particles, we propose a simplified model describing Doppler shift induced in the forward scattering configuration. Let us consider a plane containing blood vessels, which is perpendicular to the optical axis. The beam arriving at this plane has some angular distribution due to the multiple scattering in the underlying layers. A photon incident at a given angle θ , measured between the wavevector and the direction perpendicular to the vessel plane, is scattered by a RBC moving with a velocity \vec{v} . (Fig. 3.10a). We consider that scattered beam belongs to the cone of half angle φ_{Mie} , which is the maximal angle of Mie scattering in our simplified model (estimated at 5°). In consequence, the vectors $\vec{q} = \Delta\vec{k}$ belong to a part of a sphere, denoted Ω . For a given angle θ , the average frequency shift is given by:

$$M_1 = \langle \Delta\omega \rangle_\Omega = \int_\Omega \vec{q} \cdot \vec{v} dq \quad (3.6)$$

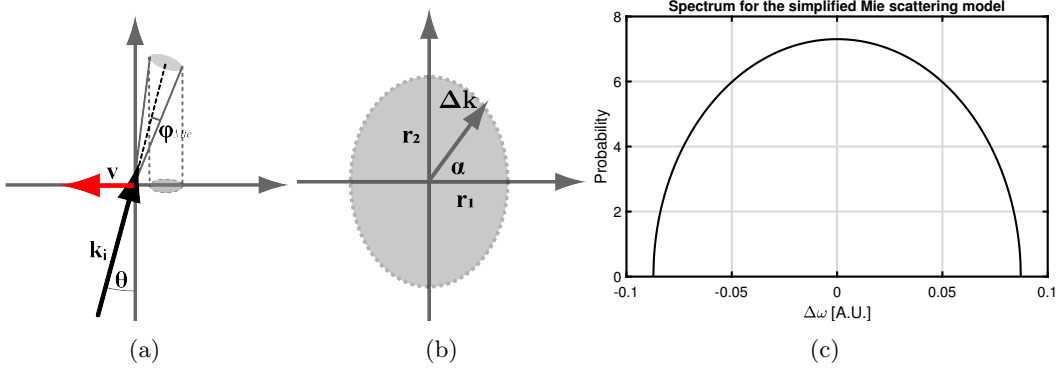


Figure 3.10: (a) Schematic representation Mie scattering, (b) a schematic defining ellipsoid to which Δk vectors belong, (c) a spectrum resulting from approximating Mie scattering as a cone with homogenous probability for all angles.

For small angles φ_{Mie} , we can approximate the part of the sphere as a disc, and then for small angle θ , we can approximate the projection of this disc on the plane in which the red blood cell moves as circular (precisely speaking, the projection of that disc onto the plane is an ellipse, but the difference between the radii can be omitted). One can easily see that in this case, the Eq. 3.6 averages to 0. The non-zero component can appear if there is a part of the vessel that is not perfectly perpendicular to the optical axis. This is illustrated in the Fig. 3.9b. Now, let us take a look at the M_2 .

$$M_2 = \langle \Delta\omega^2 \rangle_\Omega = \frac{1}{\Omega} \int_\Omega (\vec{q} \cdot \vec{v})^2 dq \quad (3.7)$$

As mentioned before, in the approximation of small angles, we can consider that the spherical cap Ω is a disk of radius R . As a result, we can write that:

$$\langle \Delta\omega^2 \rangle_\Omega = \frac{1}{\pi R^2} \int_0^R \int_0^{2\pi} (r \cdot v \cdot \cos \alpha)^2 r dr d\alpha = \frac{1}{4} \cdot v^2 \cdot R^2 \quad (3.8)$$

Now if we substitute $R = |k| \sin(\varphi_{Mie})$, we obtain that:

$$\langle \Delta\omega^2 \rangle_\Omega = \frac{1}{4} \cdot k^2 v^2 \sin^2(\varphi_{Mie}) \quad (3.9)$$

As we can see the result does not depend on the incidence angle θ . If we want to calculate the M_2 we have to integrate this result over all angles θ which will be detected by the sensor array.

$$M_2 = \int_0^\theta \int_0^{2\pi} \frac{1}{4} \cdot k^2 v^2 \sin^2(\varphi_{Mie}) dr r d\varphi \quad (3.10)$$

$$M_2 = \frac{2\pi\theta}{4} \cdot k^2 v^2 \sin^2(\theta_{Mie}) \quad (3.11)$$

To remove the dependency on the detection surface size we can normalize the result obtained.

$$\frac{M_2}{M_0} = \frac{1}{4} \cdot k^2 v^2 \sin^2(\theta_{Mie}) \quad (3.12)$$

Finally we can write:

$$\Delta\omega_{\text{RMS}} = \frac{1}{2} \cdot kv \cdot \sin(\theta_{\text{Mie}})v = \frac{2}{k \cdot \sin(\varphi_{\text{Mie}})} \cdot \Delta\omega_{\text{RMS}}$$

$$v = 6,2 \times 10^{(-3)} \text{mm/s} \cdot \Delta\omega_{\text{RMS}}$$

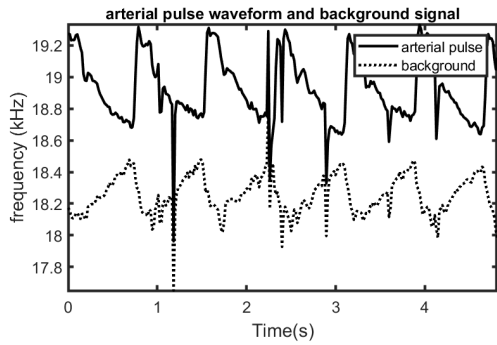
Based on this model, the velocities of 5 mm/s would yield to a Doppler broadening of $\Delta\omega_{\text{RMS}} = 0.8\text{kHz}$. To summarize, we have developed a model that provides a quantitative linear relationship between the velocity of a scattering RBC and the broadening it induces on a monochromatic beam. The approximations made involve assuming that both the angle between the optical axis and the incident wavevector, as well as the scattering angle, are small. Those approximations are justified by the Mie scattering model and the acceptance angle of the coherent detection in LDH. Now, we have to find the statistical effect induced given that the incident beam has already a given distribution of frequencies.

3.4.3 Preliminary analysis of the velocity

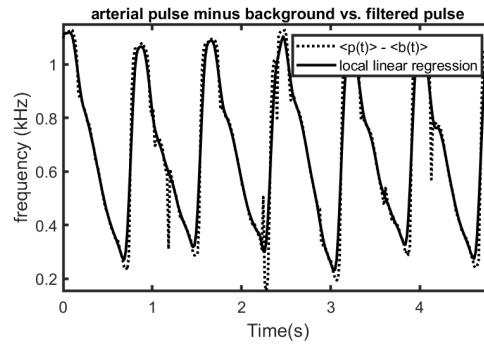
In the first step, we extended the analysis of the blood flow velocity proposed by Léo Puyo to consideration of the $\frac{M_2}{\langle M_0 \rangle_{xy}}$ ratio as a mean of extracting quantitative information from the spectrum measured. We limit our study to the retinal arteries identified earlier in the segmentation process. As proposed by Léo Puyo, we subtract the background signal from that measured in the arteries. Two improvements are proposed. The first involves extending the region of interest to encompass all arterial vessels, with each pixel processed separately. The second improvement focuses on considering a local background, rather than averaging the signal across the entire field of view. To approximate the corresponding background, the arteries mask is dilated, inverted, and applied to the video. The zero values in the video obtained are filled in by interpolating the edge values. Consequently, we obtain an estimation of what the LDH video would look like if the arteries were not present. Then again, this video is multiplied by the non-dilated artery mask. This processing enables estimating the values in the background of the arteries. Signals studied are averaged over artery regions in the original video and the one with the estimated background. As was reported before (Chapter 3), the subtraction of the background signal enables revelation of regular pulsations. Moreover, the frequency shifts measured seem to be coherent with what is expected to be induced by a single scattering event on a moving RBC (Fig. 3.11a,3.11b). The next processing step proposed consists of calculating the so-called "one cycle" video, which effectively corresponds to averaging the signal over all complete pulses. Analysis of one-pulse videos can be extremely useful for comparison between patients or stitching multiple videos to obtain wide-field dynamic maps of the retina. Distinctive pulses correspond to intervals between consecutive systoles, which are identified as the moments when the rise of blood velocity is at its highest. They can be determined by calculating the differential of the arterial signal (Fig. 3.11c). To avoid detection of false peaks in the plot, it is important to smooth the arterial signal beforehand to remove abrupt variations in intensity resulting from global eye movements. The one-pulse plot obtained allows extraction of other biomarkers such as the interval between the peak of systole and dicrotic notch, the time of the systolic velocity increase, etc. (Fig. 3.11d).

3.5 Velocity measurement

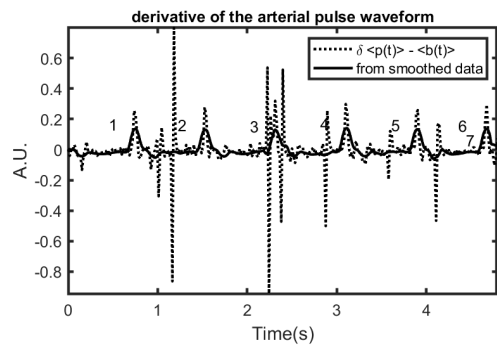
The processing proposed in the section above allows us to obtain an estimation of the Doppler broadening induced in the arteries, however, it is not physically exact, as the link between normalized



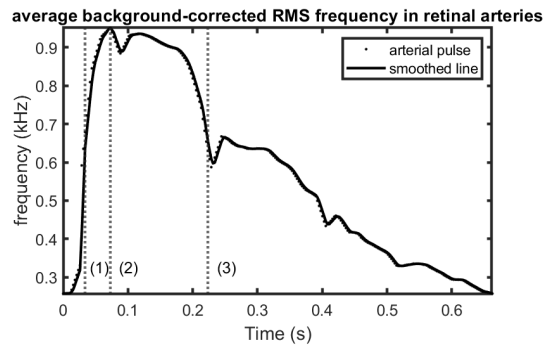
(a)



(b)



(c)



(d)

Figure 3.11: Plots representing: the signal averaged in the arteries and in the background (a), the difference between the two with local linear regression applied for systole detection (b), the derivative of the signal (smoothed and not) with peaks detected corresponding to systoles (c), the averaged one cycle waveform (d).

M_2 and the velocity was developed for a single scattering regime, in which the beam incident on the blood vessels is monochromatic, which is not the case in LDH. Moreover, the background subtraction was performed under the assumption that multiple scattering on RBCs is a perfectly additive process. This means it was treated as if two scattering events on particles with velocities v_a and v_b were equivalent to a single scattering event on a particle with velocity $v_a + v_b$. However, we have not proven that this assumption is valid.

Let us denote the spectrum of the light in the background and the theoretical spectrum, that would be obtained if the scattering were happening only in the retinal artery as S^b and S^a , respectively. The effective spectrum measured in the arteries S^{eff} can then be expressed as a convolution of the two:

$$S^{eff}(\omega) = (S^b * S^a)(\omega) = \int_{-\infty}^{+\infty} S^b(\tilde{\omega})S^a(\omega - \tilde{\omega})d\tilde{\omega} \quad (3.13)$$

If we approximate S^b, S^a as Gaussian functions,

$$S^b = A_b \exp\left(\frac{\omega^2}{\sigma_b^2}\right), S^a = A_a \exp\left(\frac{\omega^2}{\sigma_a^2}\right) \quad (3.14)$$

the effective spectrum in the arteries can be calculated as:

$$S^{eff} = \frac{\sqrt{\pi}A_aA_b\sigma_a\sigma_b \exp\left(\frac{\omega^2}{(\sigma_a^2+\sigma_b^2)}\right)}{\sqrt{\sigma_a^2 + \sigma_b^2}} \quad (3.15)$$

It should be mentioned here that the use of Gaussian approximation is inconsistent with the previous paragraph, where we calculated the coefficient allowing us to quantify the broadening, and we considered that the probability of Mie scattering can also be represented in the form of a uniform distribution in a disc. As a result, the spectrum that we approximated for scattering in the arteries represents a function:

$$P(\Delta\omega) = \frac{2}{\pi\Delta\omega_{max}} \cdot \sqrt{1 - \frac{\Delta\omega^2}{\Delta\omega_{max}^2}}, \quad (3.16)$$

which is very different in its form from the proposed Gaussian. Consequently, the calculation that will follow should be considered as a first estimation of the true model.

Quantification of the average velocity in the arteries necessitates the extraction of the σ_a parameter. To directly access the width of the spectrum, we can calculate the respective ratios:

$$\frac{M_2^b}{M_0^b} = \frac{1}{2}\sigma_b^2, \quad (3.17)$$

$$\frac{M_2^{eff}}{M_0^{eff}} = \frac{1}{2}(\sigma_a^2 + \sigma_b^2), \quad (3.18)$$

$$\sigma_a^2 = \frac{M_2^a}{M_0^a} = \frac{M_2^{eff}}{M_0^{eff}} - \frac{M_2^b}{M_0^b}, \quad (3.19)$$

$$\sigma_a = \sqrt{\frac{M_2^{eff}}{M_0^{eff}} - \frac{M_2^b}{M_0^b}}. \quad (3.20)$$

The $\frac{M_2}{M_0}$ image is calculated as the first step of the processing (Fig. 3.12a). An immediate observation is made that the contrast of the image is inverted, that is, the estimated broadening in the arteries

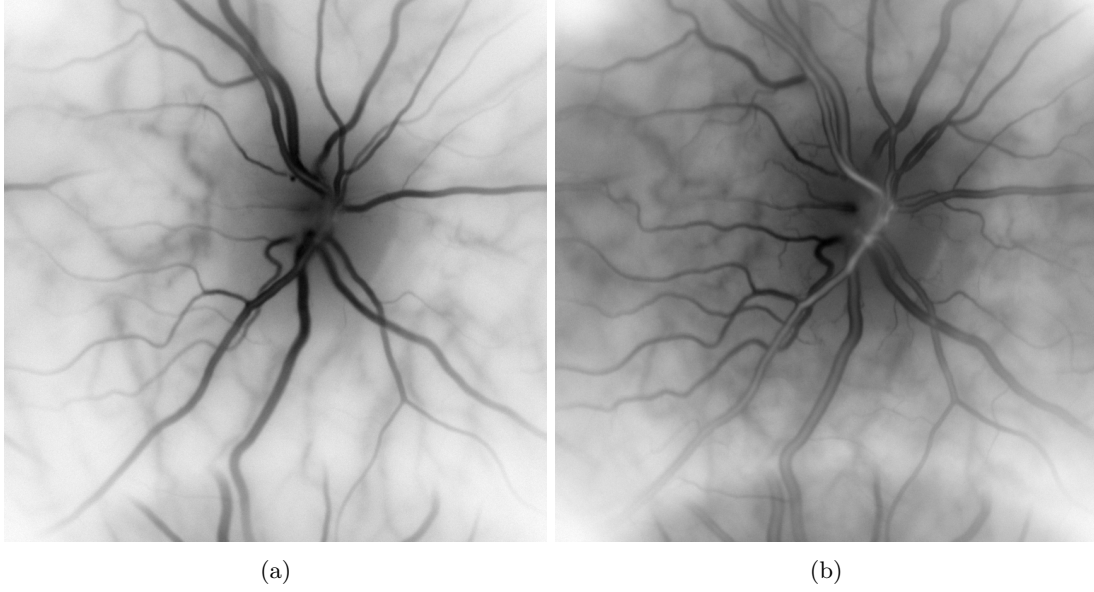


Figure 3.12: Averaged images of $\frac{M_2}{M_0}$ integrated between 6 and 30 kHz (a) and 1 and 30 kHz (b). For a lower value of f_1 we get closer to a realistic contrast in the vessels. Still, the difference between the background and the vessels does not allow correct assessment of the velocities.

is lower than that in the background. This result contradicts the physics describing the problem, and it probably results from integration in the calculation of moments between f_1 and f_2 , in order to reject components of the reference arm. This makes the analytical solution much more complex. If we were to treat the problem rigorously, we would obtain that the M_2 is actually equal to:

$$\int_{f_1}^{f_2} A\omega^2 \exp\left(-\frac{\omega^2}{\sigma^2}\right) = \frac{1}{4}\sigma^2 A \left\{ 2f_1 \exp\left(-\frac{f_1^2}{\sigma^2}\right) - 2f_2 \exp\left(-\frac{f_2^2}{\sigma^2}\right) + \sqrt{\pi}\sigma \left[\operatorname{erf}\left(\frac{f_2}{\sigma}\right) - \operatorname{erf}\left(\frac{f_1}{\sigma}\right) \right] \right\} \quad (3.21)$$

The integration on the negative side of the spectrum, which in our model is symmetrical, will give exactly the same result. As a consequence, we obtain that:

$$\frac{M_2}{M_0} = \sigma^2 + \frac{2\sigma}{\sqrt{\pi}} \frac{f_1 \exp\left(-\frac{f_1^2}{\sigma^2}\right) - f_2 \exp\left(-\frac{f_2^2}{\sigma^2}\right)}{\operatorname{erf}\left(\frac{f_2}{\sigma}\right) - \operatorname{erf}\left(\frac{f_1}{\sigma}\right)} \quad (3.22)$$

Where erf is the error function defined as:

$$\operatorname{erf}(x) = \frac{2}{\sqrt{\pi}} \int_0^x e^{-t^2} \quad (3.23)$$

Let us introduce a parameter K which corresponds to the correction that results from the integration limits.

$$K = \frac{2\sigma}{\sqrt{\pi}} \frac{f_1 \exp\left(-\frac{f_1^2}{\sigma^2}\right) - f_2 \exp\left(-\frac{f_2^2}{\sigma^2}\right)}{\operatorname{erf}\left(\frac{f_2}{\sigma}\right) - \operatorname{erf}\left(\frac{f_1}{\sigma}\right)} \quad (3.24)$$

$$\frac{M_1}{M_0} = \frac{2\sigma \exp\left(-\frac{f_1^2}{\sigma^2}\right) - \exp\left(-\frac{f_2^2}{\sigma^2}\right)}{\sqrt{\pi} \operatorname{erf}\left(\frac{f_2}{\sigma}\right) - \operatorname{erf}\left(\frac{f_1}{\sigma}\right)} \quad (3.25)$$

$$K = \frac{M_1}{M_0} \times \frac{f_1 \exp\left(-\frac{f_1^2}{\sigma^2}\right) - f_2 \exp\left(-\frac{f_2^2}{\sigma^2}\right)}{\exp\left(-\frac{f_1^2}{\sigma^2}\right) - \exp\left(-\frac{f_2^2}{\sigma^2}\right)} \quad (3.26)$$

Under the approximation that $f_1 < f_2$ we can use the series expansion:

$$\frac{f_1 \exp\left(-\frac{f_1^2}{\sigma^2}\right) - f_2 \exp\left(-\frac{f_2^2}{\sigma^2}\right)}{\exp\left(-\frac{f_1^2}{\sigma^2}\right) - \exp\left(-\frac{f_2^2}{\sigma^2}\right)} \approx \frac{f_1 - f_2 \exp\left(\frac{f_1^2 - f_2^2}{\sigma^2}\right)}{1 - \exp\left(\frac{f_1^2 - f_2^2}{\sigma^2}\right)} \quad (3.27)$$

This formula can be simplified if:

$$f_2 \exp\left(\frac{f_1^2 - f_2^2}{\sigma^2}\right) \ll 1 \quad (3.28)$$

$$\sigma \ll \frac{\sqrt{f_2^2 - f_1^2}}{\sqrt{\ln(f_2)}} \quad (3.29)$$

The right side of Eq. 3.29 varies little for f_1 an order smaller than f_2 , which is going to be decisive for condition on σ . For $f_2 = 30$ kHz, which is our maximal sampling value, we obtain approximately that $\sigma < 8.89$ kHz. In that case we obtain:

$$\frac{M_2}{M_0} \approx \sigma^2 + \frac{M_1}{M_0} f_1 \quad (3.30)$$

$$\sigma_a^2 = \frac{M_2^{eff}}{M_0^{eff}} - \frac{M_2^b}{M_0^b} - f_1 \left(\frac{M_1^{eff}}{M_0^{eff}} - \frac{M_1^b}{M_0^b} \right) \quad (3.31)$$

Let us calculate first the M_1/M_0 image, then scale it by f_1 and subtract it from the M_2/M_0 (Fig. 3.13). We immediately observe that the subtraction does not enable contrast inversion and obtaining coherent results. Additionally, the values obtained for the σ^2 across the field of view are all above 100, which means that the approximation made in Eq. 3.29 is incorrect and cannot be made.

Even though we have not succeeded in obtaining quantitative values for blood flow velocities, we can still deduce some important information about the developments made. Firstly, the higher the value of σ_a the less important the correction corresponding to the integration between f_1 and f_2 . This explains why, in Fig. 3.12, when we integrate between 1 and 30 kHz frame rate, the centres of the vessels appear in the correct contrast. Secondly, the same image suggests that taking a lower boundary for f_1 also decreases the impact of the correction, although it cannot be directly deduced from our calculations. Finally, the value of f_2 has direct impact on the limitation of σ . If we take the value of σ corresponding to the maximum of values calculated in Fig. 3.13a, which is around 16^2 , we can evaluate what value of f_2 would be sufficient to apply the approximation proposed in Eq. 3.31. Results are represented in the Fig. 3.14. One can see that a correct application of this correction could be obtained, with expected values of σ for sampling frequency of 100 kHz which would yield $f_2 = 50$ kHz.

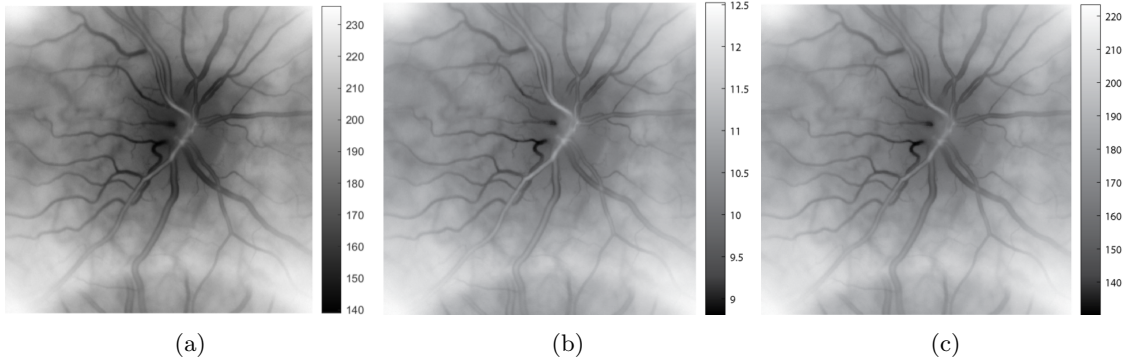


Figure 3.13: From the left: calculated image of M_2/M_0 (kHz²), M_1/M_0 (kHz) and finally the difference between the first one and the second scaled by factor f_1 . The boundaries used to calculated all moments are $f_1 = 1\text{kHz}$ and $f_2 = 30\text{kHz}$. The sampling frequency used for the interferogram recording is 60 kHz.

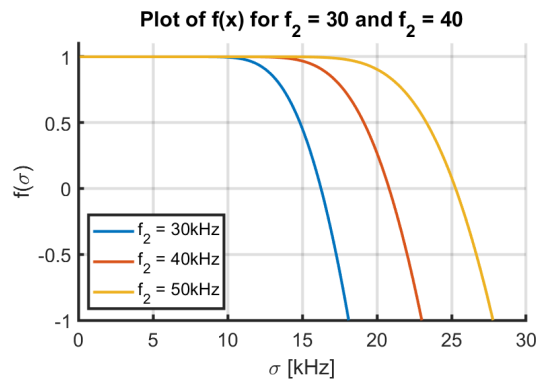


Figure 3.14: Plot representing a factor standing before the correcting term in assessment of M_2/M_0 as a function of σ for $f_2 = 30, 40$ and 50 kHz. For the predicted values of σ varying between 10 and 16 kHz the fps required to satisfy the approximation made for the correction is around 100 kHz.

3.6 Conclusions and discussion

In this chapter, we have approached the problem of blood flow quantification in LDH. We have seen in the Chapter 3 that even though this technique, in its state before the beginning of my thesis, was employed to visualize blood vessels and detect local waveforms, an approach enabling extraction of quantitative blood velocities was not proposed. One of the main observations made is that the signal in the blood vessels can be improved when the signal averaged over the entire field of view is subtracted from it.

To propose a blood flow quantification method, we employ the model of light-scattering in the retina proposed by Léa Krafft in her thesis manuscript, which suggests that the Doppler signal measured results from the last scattering event on the retinal vessels, which are illuminated from behind by the sclera, acting as a secondary source of illumination [19]. A formula linking the spectrum broadening induced with the RBC velocities has been developed. However, in a simplified model, we have considered that the incident light is monochromatic, which in reality is not the case. So far, we do not know how to extract the broadening caused by the last scattering event from the broadening induced by previous scattering events, given the spectrum in the background. With a simplified model describing the resulting spectra, we have demonstrated that increasing the camera frame rate to 100 kHz would enable such measurements with good approximation. Another approach could be based on finding a Gaussian fit for the spectrum at each point, although it would be considerably more computationally expensive. Alternatively, a strategy based on digital bidirectional measurements could be investigated. However, the potentially low SNR and varying angular composition of features across the field of view could present significant challenges.

At the same time, we have a formula that, even though it cannot be physically justified, provides coherent results and is up to now the best estimation of blood flow velocities in retinal vessels. We propose additionally a processing of the calculated signal, which allows for segmentation, extraction of averaged pulse waveforms, and a number of biomarkers.

Chapter 4

Retinal vessels elastography

4.1 Introduction

As it was already mentioned in previous Chapters, retinal images can provide information about the condition of networks which extend well beyond the eye. As an example, one can consider the nerve fibre layer, which can enable assessment of the general state of the neurons and has been studied for early detection of multiple sclerosis [70]. Similarly, analysis of the retinal vessels has been investigated for the diagnosis of cardio-vascular pathologies. Most cardio-vascular events are caused by a progressive disease called arteriosclerosis - a term which, in literal translation, means hardening of arteries. There are many risk factors which can influence the degradation and change of the elastic properties of the vessels such as: diabetes, high cholesterol level, hypertension, or smoking. Stiffness of the vessel can be directly evaluated by the measurement of PWV. It has been already demonstrated that pulse wave velocity (PWV) can help predicting: coronary artery disease [71], myocardial infarction [72], heart failure [73], stroke [74], and hypertension [75].

First, PWV value was obtained with color Doppler imaging [76]. The measurement consists in comparing of the delay between signals recorded transcutaneously (that is through the skin) at two locations (in the aorta and femoral artery). The distance between the two locations is measured on the surface of patient's body. Even though these estimations seem quite approximate, they have effectively demonstrated the link between PWV and the conditions listed above. Another, more precise technique, which can be employed to evaluate wave velocities in arteries, is the ultrasound elastography. The acquisition consists of imaging a big vessel, located not too deep below the surface of the skin, and following its deformation in time. This technique can be used to measure either the PWV or the shear wave speed (SWS) generated remotely by an acoustic accutator. The comparison between the two values, revealed that both PWV and SWS can be employed to evaluate arterial stiffening [77].

So far, there exist few techniques which assess vessel hardening in micro-vascular systems. And yet there are reasons to believe that early changes would be more easily detectable in smaller arteries which are first affected by arteriosclerosis [78, 79]. Moreover, retinal vessels are directly connected to the cerebral vasculature and hence should be better indicators of the stroke risk. In the year 2020, it has been demonstrated for the first time that PWV in retinal arteries is positively correlated to the PWV measured between aorta and femoral artery [80]. In conclusions, there is enough experimental evidence justifying the assumption that PWV in retinal arteries could become a valuable biomarker for early prediction of cardio-vascular conditions.

As mentioned in Chapter 3, Gabrielle Laloy-Borgna et al. demonstrated that it was possible to

measure the elastic waves in the retina using LDH acquisitions. In this chapter, I present the preliminary work on the automation of the retinal elastography measurements and analysis of processing parameters impact on results obtained.

4.2 State of the art

Several research groups attempted to measure the PWV in retinal arteries. In their paper from 2013, Kotliar et al. find a PWV in retinal vessels of 0.4 mm/s in normotensive subjects using dynamic vessel analyser (DVA) [81]. DVA is a commercially available device which uses a color fundus camera with adapted filters (which help distinct structures containing blood from surrounding tissues) operating in real time. Additionally, it allows the user to measure the diameter of a vessel at a chosen location. The study did not deliver experimental evidence that results obtained from arteries and veins differ. In the following years, several publications reported PVW measurements with OCT systems. In 2015, Spahr et al. used phase-sensitive full-field swept-source-optical-coherence-tomography systems (FF-SS-OCT) with sampling interval of 0.5 ms per volume to monitor the expansion of retinal tissue neighbouring the vessels. The signal cannot be measured directly on the vessels because their walls are essentially transparent and they cannot provide a coherent phase signal. Acquisition of the signal is implemented simultaneously in two regions, separated by a distance of approximately 12 mm, between which the de-phasing in pulse waveform is measured. The PVW determined with FF-SS-OCT in arteries is above 600 mm/s, so 3 orders of magnitude higher than previously reported values [82]. Additionally, no time-delay is observed for the venous signal. The authors suggest that this result is coherent with the fact that pulse wave propagates differently in veins. A different group investigated use of Doppler spectral domain OCT (SD-OCT) for PWV measurements [83]. Similarly to the previous study, the velocity is determined from comparison of pulse waveform at two locations using jump-scanning configuration. The PWV reported are between 20-30 mm/s for healthy subjects and 50 mm/s for a subject with hypertension. The study equally reports that the method used failed to measure venous PWV.

As one can see, there are enormous disparities between the PVW values measured experimentally. Gabrielle Laloy-Borgna suggests that, in reality, most measurements detect the flexural mode which is dispersive. That would explain the existence of the broad range of values determined [42]. The only measurement which agrees with the values predicted by models for PVW is 600 mm/s reported by Spahr et al. [82].

4.3 Implementation

4.3.1 Finding curve signal

Segmentation algorithm allowing to obtain vessel masks has been developed previously for the blood flow quantitative estimation (Chapter 3). A single, long vessel is chosen from the mask (Fig. 4.1a). Subsequently, from the single-vessel mask, the curve for which the signal calculated is determined. As the information about direction of wave propagation can be of interest, the order of curvilinear coordinates is saved as an output in form of the colour map, (Fig. 4.1b).

According to the thesis of Gabrielle Laloy-Borgna [42], extraction of the anti-symmetrical wave can be facilitated by averaging signals along the section of the vessel. Additionally, as we have learnt from the studies of Léo Puyo et al. subtracting a background can improve the SNR of the temporal signal [37]. From our own work, we have deduced that using a local background performs even better as it alleviates the impact of vessel crossing (Chapter 3). Nonetheless, it should be kept

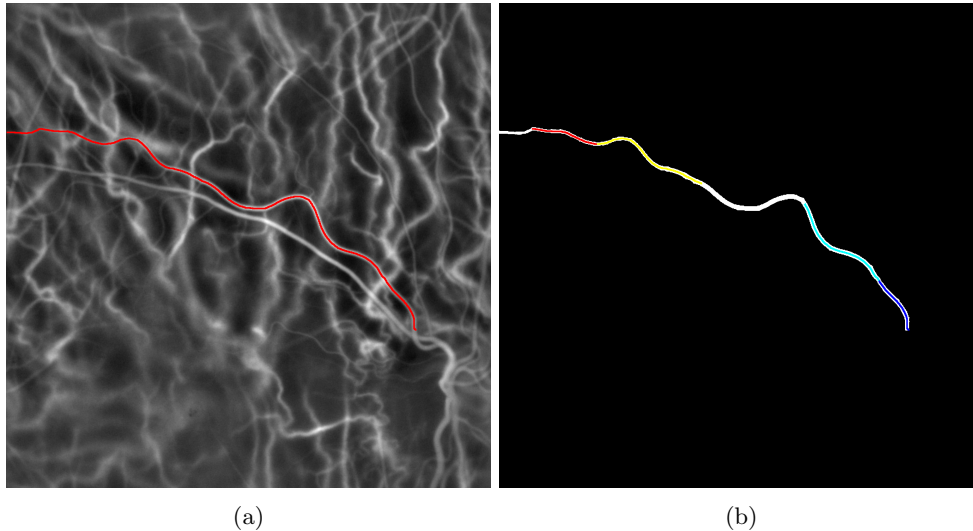


Figure 4.1: (a) Curve following the vessel. (b) Map representing the order in which the points are considered from blue to read, as a result away from ONH is considered as positive direction.

in mind that the soft tissues surrounding the vessel are probably also affected by the shear wave propagation. We have seen in the Section 4.2 that it is possible to measure the PWV by following the movements of tissue surrounding the arteries. Similarly, it is possible to measure the SWS from the neighboring tissues movements. Consequently, the impact of local background subtraction can be either advantageous or detrimental for the vessel elasticity signal. The results obtained with and without background subtraction are compared.

The curve signal is extracted as an average of the points belonging to the vessel, on the line perpendicular to the curvilinear coordinates (Fig. 4.2). Similarly, the local background is calculated as an average of 5 points on each side belonging to the same straight but lying outside the vessel.

4.3.2 Extraction of velocities from the curve signal

The data processing was identical to that proposed by Laloy-Borgna et al. [39]. First, the signal is averaged for all the curve points and the temporal spectrum is calculated. I choose frequencies with the most important signal, that is, whose energy is above approximately 10% of the maximum of the spectrum. The wavelengths of each frequency are calculated using the formula given in Chapter 3 and sine function is fitted to the plot obtained. Despite spectrum thresholding, for many frequencies, the SNR of monochromatic focal spot is low and makes it impossible to find a sinusoidal fit. I decided to reject data with a confidence coefficient of the fit lower than 0.5 (Fig. 4.3). The remaining fits give us information about the wavelength for chosen frequencies. From the latter, we can obtain the velocity or wave-vector vs. frequency plots.

The exact estimation of the field of view in the LDH is rather difficult due to the imprecise estimation of the distance at which the image of the retina is formed. Nevertheless, it is possible to propose a rough estimation of the extend of the field of view which leads to an estimation that 200 px corresponds to 1 mm, which is used in the following measurements.

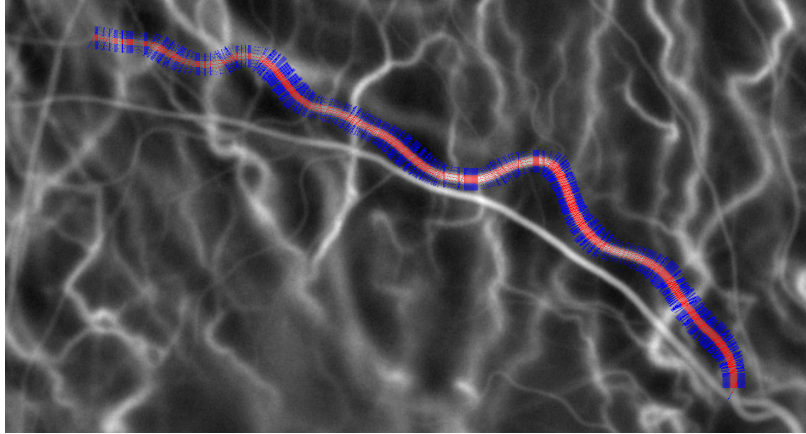


Figure 4.2: Visualisation of curve sections for artery (red) and background (blue). The respective signals are obtained by averaging over those sections.

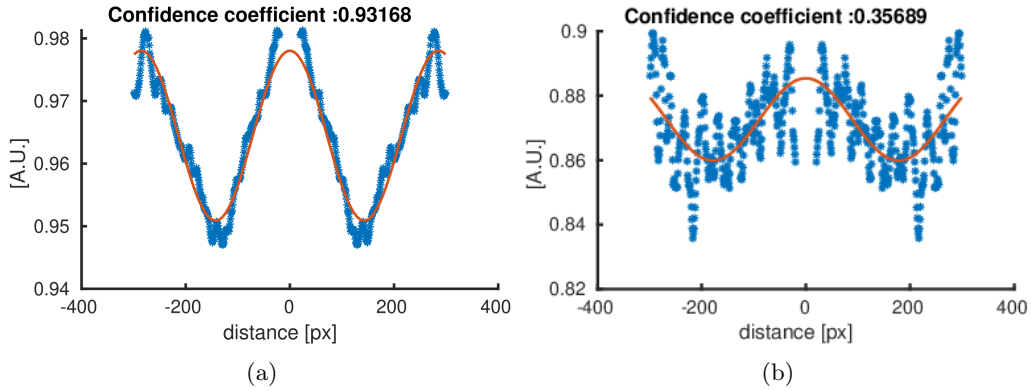


Figure 4.3: Example of plots obtained for the monochromatic focal spot calculation. (a, b) are examples of high and low confidence coefficient respectively.

4.4 Result

4.4.1 Dispersion curves

Two measurements were taken on the same volunteer (different eyes) with sampling frequencies of 30 and 67 kHz (Tab. 4.1). Power Doppler videos were calculated. The signal from main arteries was extracted and analysed using processing described above. Results obtained were represented in Fig. 4.4. Firstly, by analysing the spectrum we can see that the dominant frequencies for the two acquisitions (red for 67 kHz and blue for 30 kHz) are slightly different, suggesting that the heart rate of the volunteer varied. Secondly, the velocity vs. frequency graph suggest linear dependency between the two. As expected, the 30 kHz acquisition enables better sampling of the flexural waves corresponding to lower frequencies. This result could have been predicted given that 67 kHz video lasts only 2.57 s, because of a limited on-board memory of the camera used for the recording, which is not enough to properly sample slower variations. The wave-vector vs. frequency plot

sampling frequency	duration	resulting fps	extracted artery points
30 kHz	6.42 s	59 Hz	1057 px
67 kHz	2.57 s	131 Hz	951 px

Table 4.1: Characteristics of data acquired at 30 and 67 kHz. The main differences are: the duration of the acquisition (which was limited by the onboard memory of the camera) and the final sampling frequency.

reveals that certain points are clearly aberrant, as they deviate from the general trends, suggesting that the wavelength was, at times, incorrectly assessed. To verify this hypothesis I increased the confidence coefficient threshold to 0.7. As a result, the number of points has considerably decreased, especially for the 67 kHz data. However, some of the removed points were expected to be valid, as they belonged to the curves which could be fitted to data with high confidence coefficient, which indicates that a single-mode fit does not represent well the graphs obtained. In the dispersion curves predicted by Loloy-Borgna et al. [39], all the points belong to one branch - there is only one mode propagating in the arteries. The measurements that I have conducted rather suggest that there are multiple modes propagating. One possible interpretation is that our signal carries information about both the arteries and surrounding tissues, and we are not capable to distinguish between the two. Nonetheless, it is possible that the single mode description of the waves propagating in the blood vessels is not exhaustive. Moreover, it seems that many points which seemed to have a good tendency were rejected when the confidence coefficient threshold was increased. It is possible that confidence coefficient is not sufficient as a condition for the validation of the wavelength measurements. For example, if a given frequency compromises multiple modes the effective confidence coefficient will be low. An alternative solution consists in Fourier analysis of the monochromatic focal spot.

The same processing can be applied to the main veins. The confidence coefficient threshold was again set to 0.5. The results are presented in Fig. 4.5. The velocity vs. frequency graphs are represented in the log scale as three of the points measured have velocity an order of magnitude higher than the others. The slopes suggested by the 67 and 30 kHz acquisitions vary greatly. The same points represented in the wave-vector vs. frequency space reveal that only the 67 kHz acquisition allows us to observe general predicted tendencies, that the wavenumber increasing with the frequency. The observation that was made for arteries about the impact of video length is not valid in the case of the veins, which can be due, however, to the spectrum thresholding. The results cannot be easily improved by increasing of the confidence coefficient threshold as essentially all the points that were selected using the 0.5 threshold, have a confidence coefficient above 0.75. As for the arteries, the points measured clearly cannot describe a monomode dispersive curve. Given that the confidence coefficient of the sinusoidal fit is very high for all the points, it is valid to suspect that the errors arise from the way the signal is extracted from the power Doppler video.

The analysis of waves propagating in the vessels using monochromatic measurements requires a number of adjustable parameters and therefore the interpretation of the results can be ambiguous. In consequence, from now on, only the time-of-flight measurements will be considered.

4.4.2 Time of flight measurements

Let us investigate the possibility of subtracting the signal of the local background. The impact of background subtraction is especially crucial for veins, which are in consequence considered in the study presented here. The slope of the fringes is quantified by calculating the 2D Fourier transform of the image, and choosing a pixel of maximum intensity (Fig. 4.6). One can see that the background

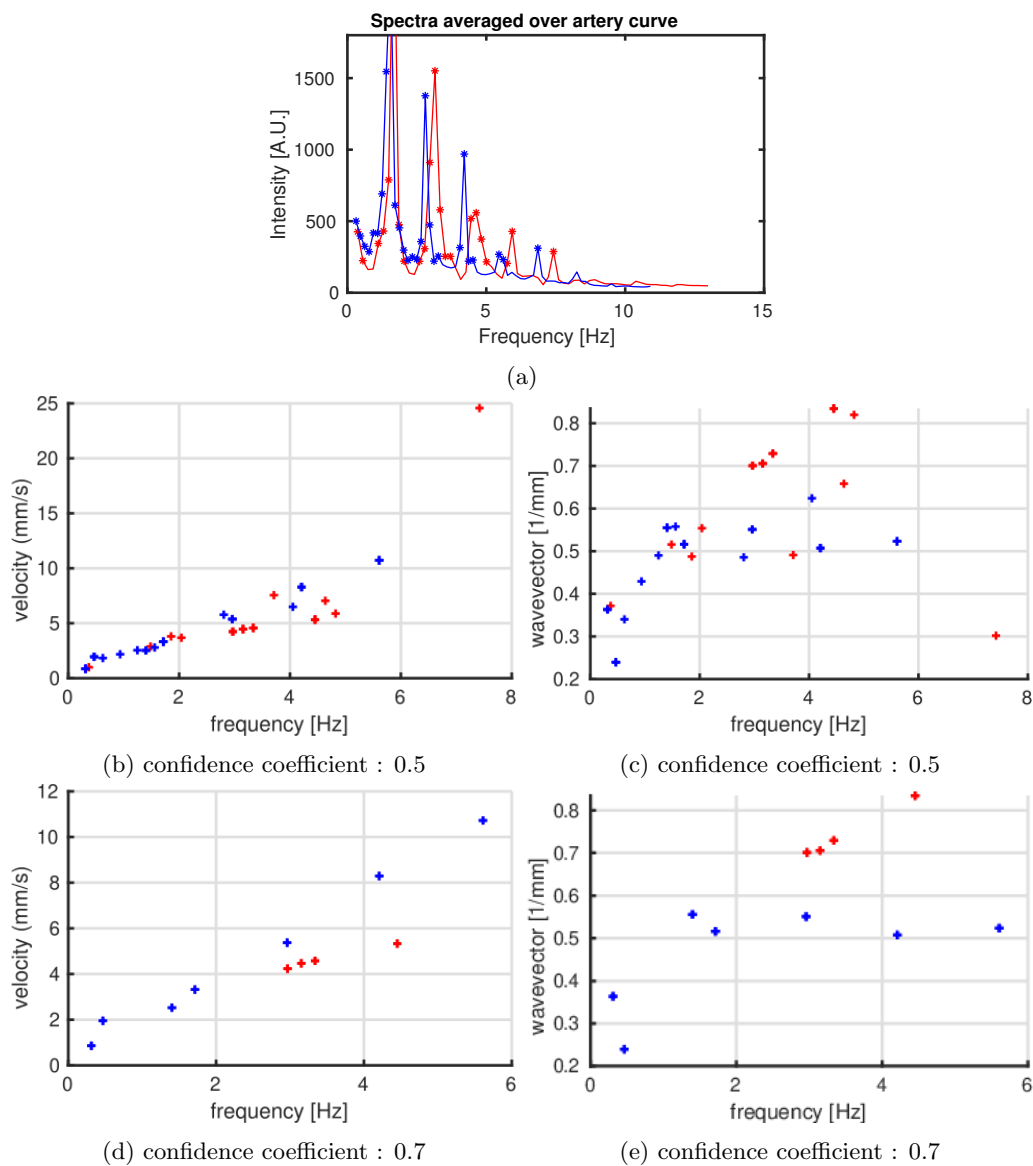


Figure 4.4: The spectrum of power Doppler videos averaged over the positions along the main artery for the acquisition at 67 kHz (red) and 30 kHz (blue) frame rate (a).. The frequencies carrying a significant amount of energy were selected (marked on the spectra plot with *). The wavelengths corresponding to these frequencies were converted to velocities and wave-vectors, and plotted against the frequencies. The confidence coefficient threshold, which is used as a criterion for the data validity, was initially set at 0.5 (b,c) and then increased to 0.7 (d, e).

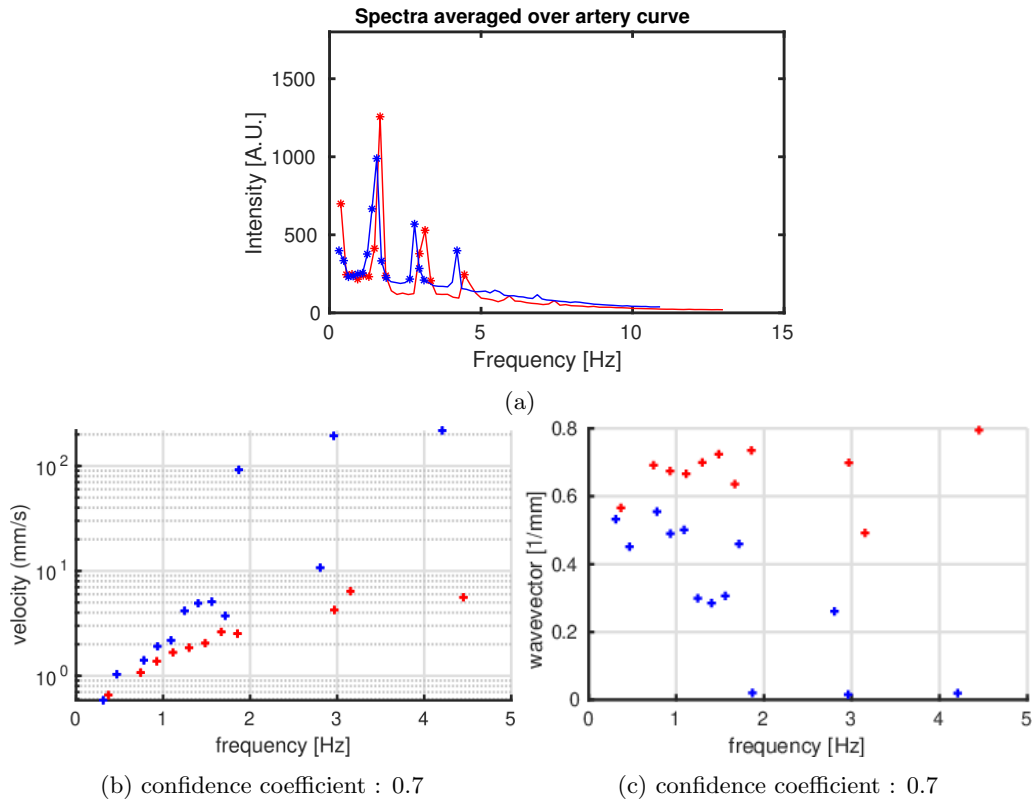


Figure 4.5: The spectrum of power Doppler videos averaged over the positions along the main vein for the acquisition at 67 kHz (red) and 30 kHz (blue) frame rate (a). The frequencies carrying a significant amount of energy were selected (marked on the spectra plot with *). The wavelengths corresponding to these frequencies were converted to velocities (b) and wave-vectors (d), and plotted against the frequencies. The confidence coefficient threshold was set to 0.5.

signal subtraction discards the majority of the modes, leaving only the dominating one. Furthermore, it increases the directionality of the propagation - the distribution of energy becomes less uniform. As a result, this operation facilitates the choice of the “dominant wave” velocity. However, its value, which corresponds to the exact position of the peak, changes slightly. Before the background signal subtraction, we measured a velocity of 1596.47 px/s which corresponds to approximately 8 mm/s, after the background subtraction the velocity was estimated at 1217.45 px/s which corresponds to approximately 6 mm/s, both values measured at 1.42 Hz. Subsequently, time of flight measurements were compared for arteries and veins for both sampling frequencies (Fig. 5.9). Similarly to the procedure presented above, the peak corresponding to the highest energy was determined. One can observe that the sign of the dominant spatial frequency in the arteries is opposed to that in the veins in both cases. The fact that the sign for the two arteries is different results from the fact that the orientation of the image with respect to the ONH has not been taken into account. Finally, to verify the observation about the dominant direction of propagation, I compare the results obtained on a larger number of acquisitions. Nine LDH measurements were performed on the same volunteer. The images were centred on different vessels (both eyes were measured). Some vessels

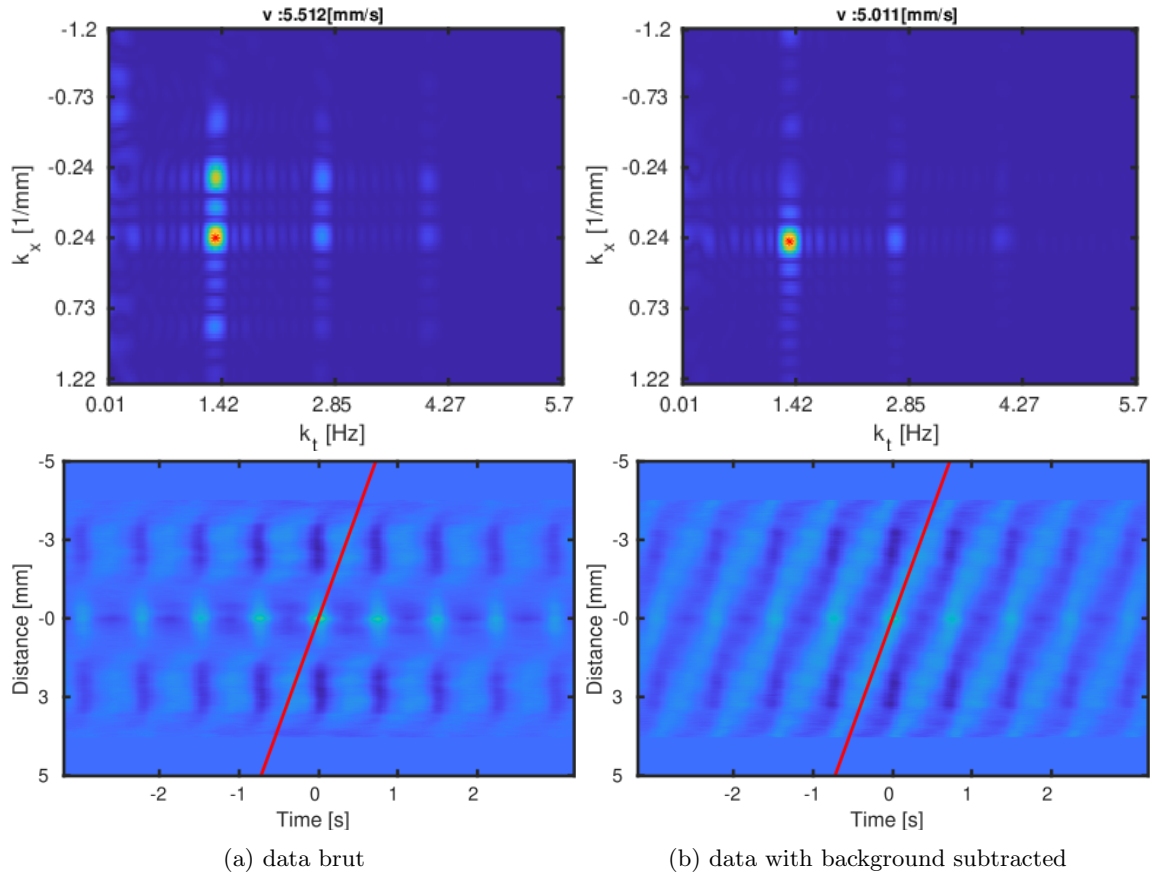


Figure 4.6: The signal extracted from the vein at 30 kHz is analysed using time of flight measurements. The raw signal (left column) and with background subtracted (right column) are considered. The top row represents the 2D Fourier transform of the graphs below. The mode with the highest energy is selected and marked with a red '*' symbol. Corresponding slope is plotted in red.

were sampled multiple times (with different frequencies). The frame rate of the camera used varies between 20 and 70 kHz. However, in the final processing, the videos taken at 20 kHz fps were discarded as they did not provide sufficient SNR for elastomeric analysis. The number of arteries and veins studied is uneven as in one quadrant main vein splits close to the ONH into two large branches. The dominant velocities were assessed using time-of-flight measurements. The results are represented in Fig. 4.8. The first observation that can be made is that the flexural waves with the highest energy in the veins propagate towards ONH, whereas in arteries they propagate away from ONH. Subsequently, the group velocity as a function of the vessel thickness is plotted. Overall, the absolute value of the velocity in arteries seems to be slightly higher than that in veins. However, there is no clear correlation between the two parameters, which might result from the inaccuracy of the vessel thickness measurements.

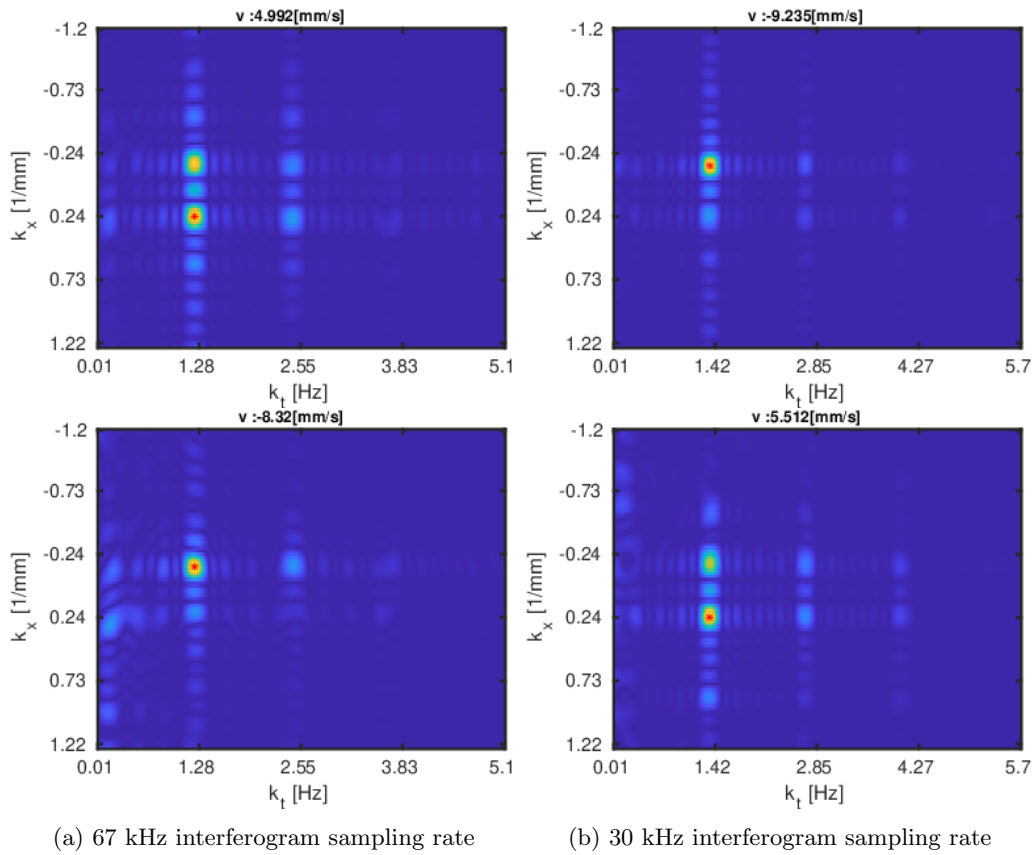


Figure 4.7: The time-of-flight measurements are represented in the Fourier space for veins (top row) and arteries (bottom row). Data acquired with 67 kHz (a) and 30 kHz (b) frame-rates are considered

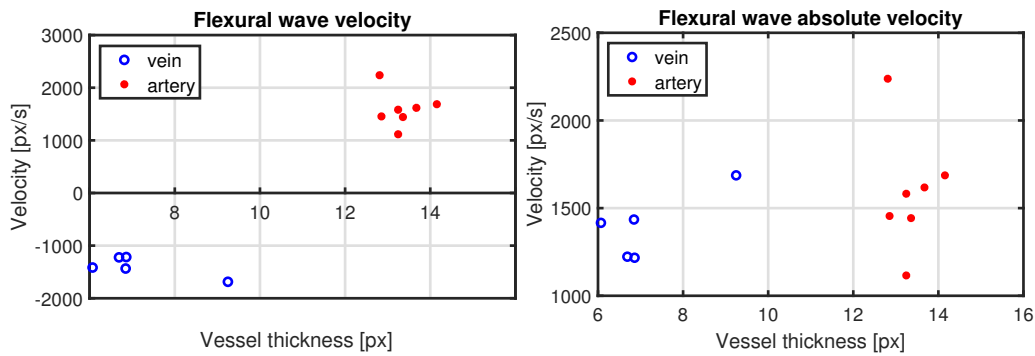


Figure 4.8: Velocities for veins and arteries are represented as a function of the vessel thickness. On the left the direction of the propagation is considered, on the right the absolute values of velocities are taken.

4.5 Discussion and conclusion

LDH can be considered as a very unconventional method for elastometric measurements as it does not measure directly the displacements. Instead, power Doppler images correspond to broadening of the spectrum induced by scattering on moving particles, so that the collective motion of particles induced by a mechanical wave modifies this spectrum. According to current models of elastic wave propagation in blood vessels, the LDH technique has a field of view that is too limited relative to its sampling frequency to effectively detect the PVW. It allows, however, identification of waves propagating at much lower velocities, which were identified by Gabrielle Laloy-Borgna et al. as flexural waves.

Automated extraction of dispersion curves from LDH data remains rather challenging. As one could see, the duration of the power Doppler video can be a limiting factor for sampling of the lower frequencies, especially for arteries. Further advancements, including higher camera frame rates, will undoubtedly help us overcome these limitations in the future. The veins have been shown to have a greater number of points with high confidence coefficient, which suggests that the flexural waves are easier to detect in veins. This could be due to the fact that the blood flow velocity varies less in the veins and thus the separation of the blood flow variations due to pressure changes from those induced by the vessel movements are easier.

The comparison between 30 and 67 kHz data suggests that the sampling frequency changes the results obtained. Firstly, we have observed that the length of the recorded video has more influence on the results obtained than the frequency at which the interferograms are sampled. To validate this conclusion it would be useful to compare results obtained from videos of the same length, which could be easily performed by cropping the 30 kHz video. Secondly, we have observed that the results vary qualitatively, that is we observe different additional branches in the dispersion curves which appear for either 30 or 67 kHz videos. Again, to fully validate this observation, it would be necessary to distinguish between the sampling frequency of the interferograms and the effective frame-rate in the power Doppler videos. It is possible that this effect is caused by some kind of aliasing, which could be alleviated using a more developed processing approach.

Investigation of background subtraction so far is not very conclusive. I have observed that the procedure modifies qualitatively the results. It is not clear whether the removal of some modes and the shift of the main peak have a physical/physiological justification, or not. I believe that it would be interesting to see if there is a correlation between certain modes propagating in the vessels and in the surrounding tissue which could be induced by the mechanical movements of the vessels.

Finally, it was observed that the direction of dominant wavefront propagation is the same as that of blood flow in a given vessel. That is the waves in arteries propagate away from the ONH whereas in the veins they propagate towards ONH. Development of a model which would allow us to properly predict the form of the dispersion curve for different vessel types and thus explain this phenomenon is needed.

Chapter 5

Holowaves software

5.1 Introduction

As mentioned previously, LDH is by principle a technique for which the great majority of adjustments is performed numerically. As a result, the digital processing is complex and consists of a great number of code lines. For this reason, the totality of the code used in LDH measurements is assembled into three software:

- **Holovibes**, written in C++ and CUDA, enables real-time rendering of holograms used as a preview. Typically, the camera connected to it runs at a 5 kHz frame rate. In the rendering, we use batches of typically 32, 64, or 128 frames to calculate image which results in a 157, 78, or 40 fps respectively. The maintenance of this software was beyond the scope of my thesis.
- **Holowaves**, written in MATLAB, computes all types of videos from the interferograms recorded using ultra-fast camera
- **Pulsewave**, written in MATLAB, takes as an input the output videos of Holowaves and extracts from it the biomarkers. It is the newest of our softwares, and its development was mostly the work of my colleagues: Yohan Blazy, Olivier Martinache, and Yann Fisher.

All of them are open-source and can be downloaded directly from our Github repository: Holowaves

5.2 Holowaves

The first versions of the Holowaves software was created as a collective work from a number of internships which preceded my thesis. The advances and modifications which I proposed consisted in providing new outputs, a aberration correction system, and reorganization of processing. I have proposed to organize the functionalities into five main compartments of the front-end:

- **File loading**: where one enters information about acquisition parameters as well as the characteristics of the machine on which the processing is performed.
- **Video rendering**: where one chooses the type of the output, the way in which the entire stream of interferograms is going to be segmented, and if the registration of the frames is performed. In the newest version, we have also proposed the “folder management” modality which allows user to pre-define rendering parameters, save them in the “config” file for multiple

interferogram streams, and launch the rendering of all of them at once. This data management tool has already proven to be a valuable improvement when dealing with large amounts of data acquired on patients.

- **Image rendering:** where one defines the parameters for the rendering of a single frame, a preview of which is displayed in the box above. It is equally possible to save the preview in .png file.
- **Advanced Processing:** is a section mostly used for tests such as local SVD filtering or the dark-field digital holography modality. The majority of processing proposed in not applied in the image rendering.
- **Aberration Compensation:** where one chooses parameters connected with aberration compensation. The wavefront measured plus three first Zernike coefficients are displayed in the bottom of the box. Additionally, above this section, we display the images calculated from the field in subapertures which are going to be cross-correlated.

One can see that in the current form the software serves probably more as a scientific aid rather than a clinical one. The main application of the Holowaves software is to ensure that all results reported can be easily reproduced. Proposing a Holowaves version for a clinical studies requires drastic simplifications of the software and is beyond the scope of my thesis.

5.3 Holowaves extension to FF-SS-OCT

It is worth noting that the majority of processing necessary to obtain the final videos is also applied to the interferograms obtained using FF-SS-OCT. For that reason, we decided to extend the Holowaves software variability and allow it to process 3D data. The data used for this aim are the courtesy of Maciej Wojtkowski from ICTER, Warsaw.

The FF-SS-OCT utilizes frequency a sweep to encode the information about the reflectivity of planes in the sample arm. The camera is typically located in the image plane of the sample. The volume reconstruction relies on associating the recorded flicker frequencies to corresponding depths. One can see that this technique is analogous to the LDH - the flicker frequency encodes the information to be extracted, that is the depth for FF-SS-OCT and the scattering particles velocity for LDH. Puyo et al. demonstrated in publication from 2022 that the two techniques can be combined to obtain a wider range of information about the retina [84].

The main differences between the LDH and FF-SS-OCT, which make the techniques inherently different, are the coherence length of the laser and the distance between the image and camera planes. As mentioned previously the coherence length of the diode laser used for LDH is much greater than the path light travels between emission and detection. On the other hand, the coherence length of the laser used for OCT, is typically quite low to perform gating and reject multiply scattered photons. The acquisitions in LDH is taken outside of the focal plane, which enables separation of the twin images, whereas in OCT typically, the detection is performed in the focal plane. The propagation distance between the image and detection planes has a crucial impact on the properties of the field recorded as it drastically changes the the angular composition of the images obtained. Nevertheless, these aspects do not change key elements of the processing that allows extracting images from interferograms recorded.

A part of my work on the Holowaves software consisted in implementing the modality enabling the reconstruction of the OCT data. In the current form, one can switch the data input type to the OCT, correct for the aberration, visualise the cross-sections chosen, and render the corresponding videos (Fig. 5.2).

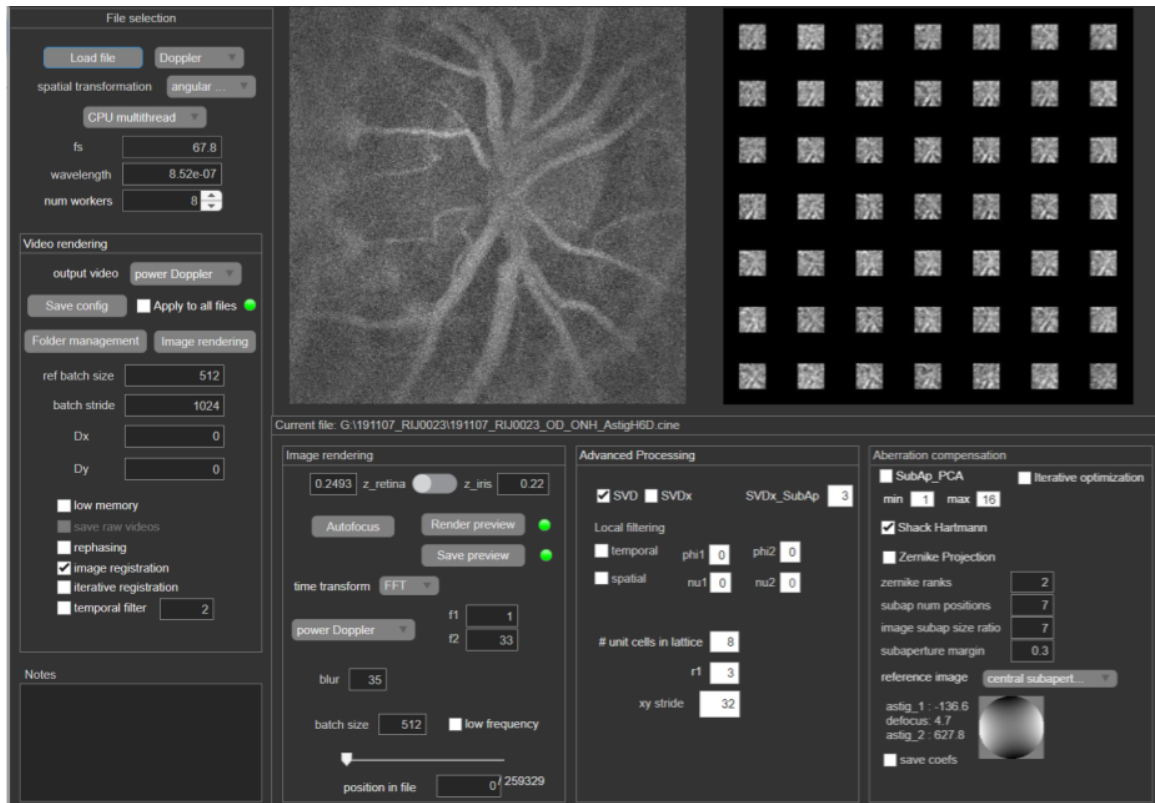


Figure 5.1: The interface of the Holowaves software. The image represented (left) is a LDH of the ONH. To the right one can see the subimages, which were being correlated for the numerical Shack-Hartmann algorithm.

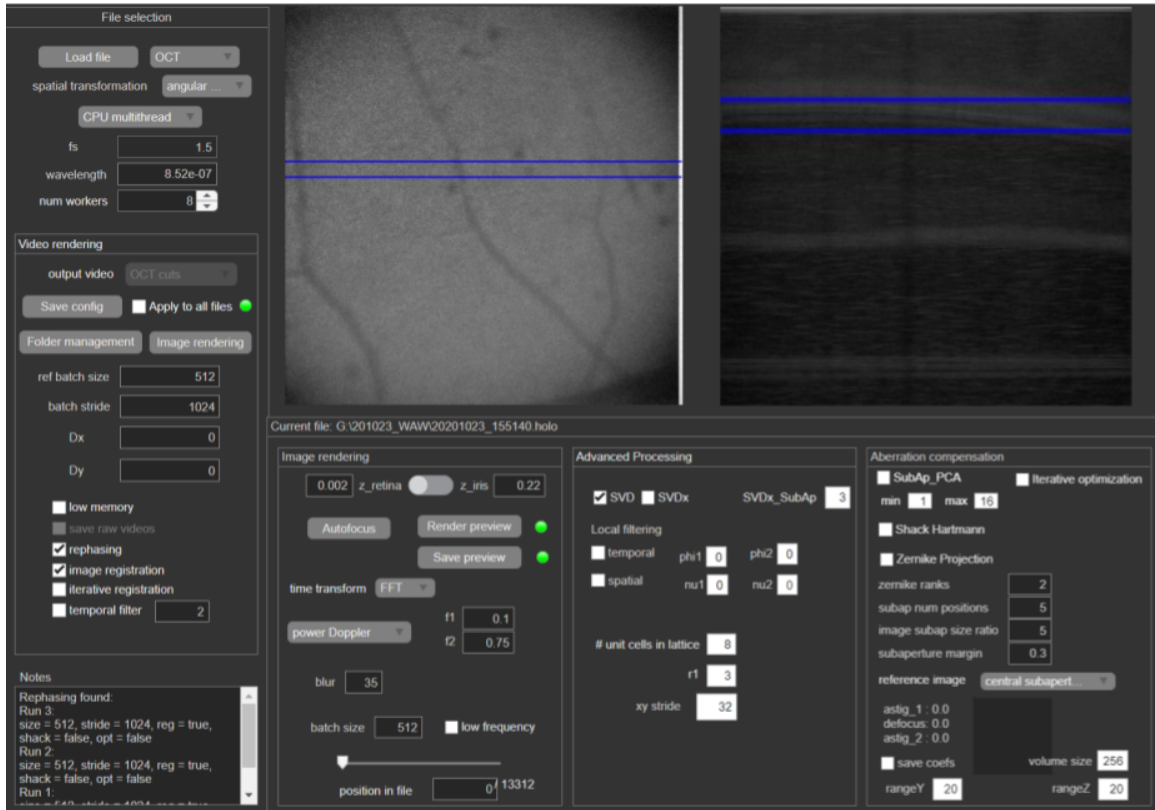


Figure 5.2: The interface of a Holowaves software in the OCT configuration. The image on the left represents an FF-SS-OCT en-face image of the retina. The two blue lines indicate the section over which the signal is averaged to represent the b-section of the image on the right. Similarly, the blue lines on the right show the layer which is averaged to create the image on the left.

5.4 Future perspectives for the Holowaves software

The Holowaves software is primarily designed to optimize processing and facilitate studies on larger patient populations. However, transforming it into clinical software would require a significant simplification. Currently, generating power Doppler videos involves numerous adjustable parameters, posing a challenge for clinical applications.

Another key function of Holowaves is to support scientific collaboration and exchange. Ideally, the software should incorporate a method that allows for the seamless integration of plug-ins, such as alternative aberration correction techniques or spectrum analysis, enabling the creation of new types of output videos.

Conclusions and Perspectives

Conclusions

As it was illustrated throughout this manuscript, the work I have conducted during my thesis consisted of proposing advances to LDH that allow us to bring the device closer to the clinical use. Firstly, adding a diffuser to the optical setup of LDH enables wide-field blood flow imaging. In the current state the field-of-view covers comfortably the ONH and four main branches beyond the optic discs. As a result, the blood flow measurements, performed with a single acquisition, can assess the total blood perfusion of the retina. In the following Chapter, it is convincingly illustrated that the first aberration compensation technique was successfully implemented in LDH. Ensuring that ocular aberrations do not jeopardize the measurement is crucial, given that they affect an important percentage of the population. Subsequently, I have studied the possibility of quantifying the blood flow using combined moments 1 and 2 for the blood flow measurements, which emphasized the acute need for the development of a more comprehensive model of Doppler broadening induced by the multiple scattering in the layers of the retina. Finally, the preliminary study of the elastic waves propagating in the retinal vessels revealed that again separation of the background from the true signal may be an effective way to overcome the difficulties arising from the multiple scattering.

In conclusion, one could see that, even though there are still some experimental and theoretical challenges and limitations that need to be overcome to make LDH a widely used clinical device, there are many opportunities for improvement. Moreover, a great majority of the results presented here was obtained numerically, which means that none of these improvements entails additional costs for the clinical device. Moreover, all the codes are available online and can be shared with all interested research groups which would be willing to reproduce LDH.

Perspectives

Aberration compensation

In Chapter 2, it is shown that numerical Shack-Hartmann enables wavefront measurement and compensation. Moreover, using a resized image as a reference for subaperture shift assessment has yielded the best final resolutions. Its limitations arise from a weak performance in the situation where strong distortions completely blur out the features in the initial image. As for the wavefront reconstruction technique, there were reasons to believe that in the case of LDH, the gradient integration technique would be more effective. I believe that a final comparison should be conducted on data acquired on patients with astigmatism, keratocone, etc. to test it in situations that are closer to clinical cases. Equally promising would be to demonstrate that numerical Shack-Hartmann is an optimal technique for aberration compensation and performs better than the iterative approach. The key element for the comparison would be, however, the calculation time. Finally, it would be worth verifying if the aberration compensation could be performed in the real-time processing. Possibly, it would demand to push the algorithm to the extreme in terms of simplicity and robustness: considering a low number of Zernike modes, cross-correlating a small images extracted from the sub-images etc. Nevertheless, I believe that it is, or will be in the near future, possible to numerically compensate for aberrations in real-time.

Aberrometry measurements

The applicability of the LDH for aberrometric measurements is limited given that the NA of the instrument is very small. Nevertheless, it seems important to validate quantitative measurements of Zernike coefficients, to verify that we can correctly assess the extent of effective pupil size of

the instrument. Furthermore, as it was shown, LDH could be employed for the measurements of peripheral aberrations. In my opinion, LDH, and similar technologies offer an opportunity to alleviate the need for forming a perfect point source at the retina, which is now required in the aberrometric measurements. For this reason, I believe that it is interesting to further investigate this issue. Moreover, it is a challenge to understand why measurements of variations of the 2nd order Zernike coefficients resemble the corresponding polynomials themselves. The most straightforward approach would be to verify that the change in the angular composition of each point mixed with the spherical mismatch between the focal and retina plane do not induce this effect. This can be done with a numerical simulation.

Blood flow measurement

The blood flow quantification remains still a challenge. The main problem that needs to be solved for correct blood flow assesment is how to distinguish the contribution of the so-called background from the signal. The simplified model, that I have proposed, describing the effective form of the spectrum as well as scattering itself was developed to find a simple, analytical solution to the problem - one formula which could convert the moments of the spectrum into the blood flow velocity. I have shown that under the hypothesis made, and with the current sampling frequencies, this cannot be achieved. The next approach to investigate is based on fitting a Gaussian function to the spectrum recorded. Eventually, the Gaussian model can be replaced by a distribution which better corresponds to what is being observed.

Retinal vessels elastography

Gabrielle Lolo-Borgna in her thesis concludes that LDH is not the best suited device for the measurement of the velocity of the elastic waves propagating in the retina as it does not follow directly the deformation but a velocity variation which could be caused by the latter. It is true that this adds additional complexity but LDH has some important advantages. First of all, compared with the techniques which have sufficient resolution for detecting the small deformation of the vessels, LDH has a far-spreading field of view. The measurements were conducted without the need for developing a new configuration - as it was the case for the OCT systems where the measurement had to be taken at two locations with a distance between the two being additionally measured. As mentioned before, improvements of the segmentation algorithm should ameliorate the SNR. Furthermore, there are reasons to believe that optimizing the sampling frequency could offer a perfect balance between the length of the video and the Doppler broadening sampling capacities. The capabilities of the technique could be also improved by the use of triggered camera which could acquire interferogram batches at chosen intervals. As a result, a video covering a large time span, without compromising the ability to detect the highest velocities, could be recorded. As one could see, the elastic waves are possibly easier to detect in veins using LDH. Unfortunately, there are indications, that they are of a lesser importance for clinical applications because the most cardiovascular incidents are caused by a modified elasticity of arteries. Nonetheless, I believe it would be worth studying the properties of veins in the pathological cases such as the spontaneous pulsation of veins.

Résumé en français: Avancées en Holographie Doppler Laser

Introduction

L'évolution démographique mondiale montre un vieillissement rapide de la population, avec une augmentation prévue du nombre de personnes âgées de 60 ans et plus. Ce phénomène entraîne une demande croissante en soins de santé spécialisés, notamment dans le domaine de l'ophtalmologie. Les maladies oculaires liées à l'âge, telles que les erreurs de réfraction, les cataractes, le glaucome, la dégénérescence maculaire liée à l'âge (DMLA), et la rétinopathie diabétique, touchent principalement la population vieillissante. Ces pathologies nécessitent des techniques d'imagerie avancées pour un diagnostic précoce et précis.

L'imagerie rétinienne joue un rôle crucial non seulement dans la détection des maladies oculaires, mais aussi dans l'évaluation des conditions systémiques comme le diabète et l'hypertension. Parmi les techniques d'imagerie de pointe, l'holographie Doppler laser (LDH) émerge comme une méthode prometteuse, offrant des possibilités uniques de détection des flux sanguins et d'analyse des microvasculatures rétinienne et choroïdienne.

Context

L'Œil Humain

L'œil humain est un système optique complexe, composé de plusieurs éléments qui travaillent ensemble pour produire la vision. La rétine, située à l'arrière de l'œil, est une structure multicouche qui capte la lumière et la convertit en signaux nerveux envoyés au cerveau. La vascularisation de l'œil est assurée par deux réseaux principaux : le réseau vasculaire rétinien, alimenté par l'artère centrale de la rétine (CRA), et le réseau choroïdien, alimenté par les artères ciliaires postérieures (PCA).

Les pathologies telles que le glaucome, la rétinopathie diabétique, et la DMLA affectent la perfusion sanguine de l'œil, conduisant à des complications graves si elles ne sont pas détectées et traitées à temps. Par exemple, le glaucome est souvent associé à une pression intraoculaire élevée qui affecte le flux sanguin dans la tête du nerf optique, tandis que la rétinopathie diabétique résulte de l'hyperperméabilité des vaisseaux rétiniens, provoquant des œdèmes maculaires et des exsudats durs.

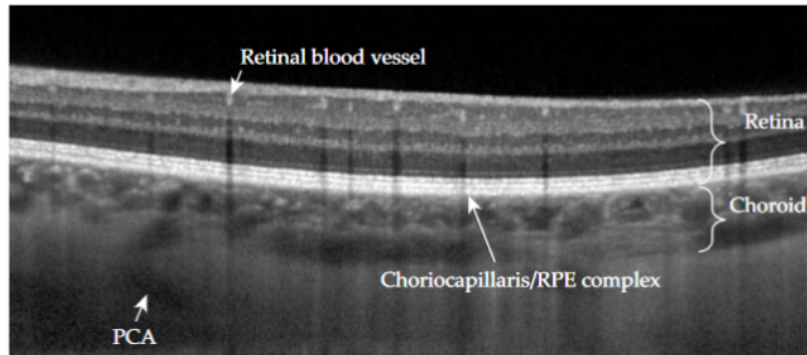


Figure 5.3: Figure adapted from [2]. The layered structure of the human eye fundus seen with OCT. The layers of the retina are well visible as well as some of its vessels. Underneath we can distinguish the choroid. The structures get considerably blurred closer to the sclera whose outline is effectively invisible.

Holographie Numérique et Élargissement Doppler

L'holographie numérique est une technique qui permet de capturer et de reconstruire des images en enregistrant l'interférence entre un faisceau de référence et un faisceau diffusé par l'objet. Cette méthode est particulièrement efficace pour observer des phénomènes rapides, tels que les mouvements des globules rouges dans les vaisseaux rétiniens, grâce à l'effet Doppler, qui modifie la fréquence de la lumière diffusée en fonction de la vitesse de déplacement des particules.

La propagation de Fresnel et le spectre angulaire sont deux méthodes couramment utilisées pour reconstruire l'image de l'objet à partir des données holographiques. En LDH, la détection des termes croisés de l'interférence permet de déterminer la direction axiale du flux sanguin, ce qui est crucial pour une analyse précise des dynamiques de flux dans l'œil.

Holographie Doppler Laser (LDH)

La LDH, qui combine une détection holographique avec des mesures Doppler, offre plusieurs avantages pour l'imagerie du flux sanguin rétinien. Elle permet une séparation claire des termes d'interférence, une correction numérique des aberrations optiques, et une amélioration du rapport signal/bruit grâce à la forte intensité du bras de référence. Ces capacités sont essentielles pour l'analyse des mouvements sanguins rapides dans la rétine et la choroïde.

La configuration optique utilisée en LDH est basée sur un interféromètre de Mach-Zehnder, comme illustré dans la Fig. 5.4. Cette configuration utilise un laser infrarouge et deux caméras CMOS, l'une pour la surveillance en temps réel et l'autre pour le rendu numérique des images, fournissant des vidéos dynamiques du flux sanguin.

La reconstruction d'image en LDH implique plusieurs étapes, dont la propagation numérique jusqu'au plan focal, le passage au domaine des fréquences temporelles, et l'intégration dans une bande de fréquences choisie. Ces étapes permettent de capturer des images détaillées des vaisseaux rétiniens avec une résolution temporelle élevée.

Dans un article de 2018, Leo Puyo et al. ont démontré pour la première fois la faisabilité des mesures in-vivo par LDH sur l'œil humain [?]. Les vidéos obtenues ont été calculées en utilisant M_0 du spectre détecté, intégré dans une bande de fréquences choisie. Les valeurs obtenues étaient exprimées en unités arbitraires, car le lien entre M_0 du spectre et la vitesse locale des particules

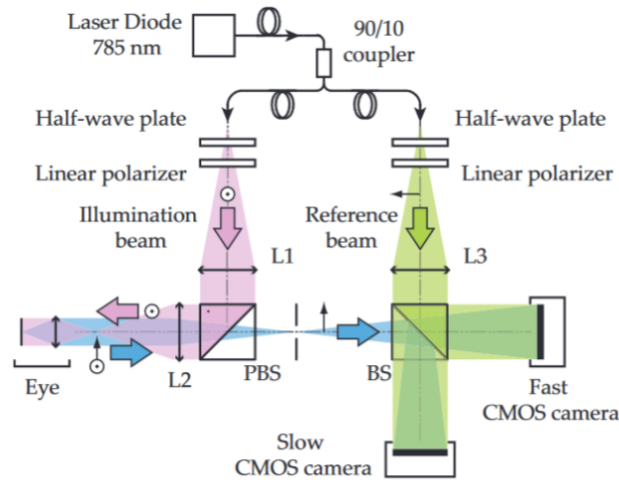


Figure 5.4

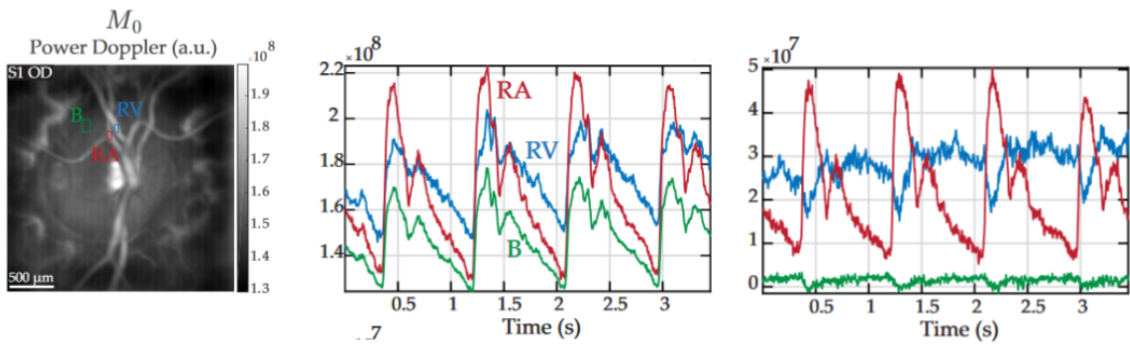


Figure 5.5

diffusantes n'était pas encore développé. Une analyse comparative du signal détecté dans les artères rétiniennes, les veines et le fond suggérait que la soustraction du signal moyenné sur l'ensemble du champ de vision permettrait d'extraire des signaux compatibles avec les connaissances actuelles sur la physiologie du flux sanguin.

Les mesures par LDH ont également été utilisées pour mesurer l'élasticité des vaisseaux rétiniens [39]. Un signal le long d'un vaisseau choisi est extrait des vidéos M_0 précédemment calculées et traité en utilisant : une remise au point numérique basée sur la rétroaction temporelle et une approche par temps de vol. Les résultats obtenus suggèrent l'existence d'ondes de cisaillement dispersives se propageant dans les vaisseaux rétiniens avec des vitesses relativement faibles de l'ordre de quelques mm/s à des fréquences de 1 Hz.

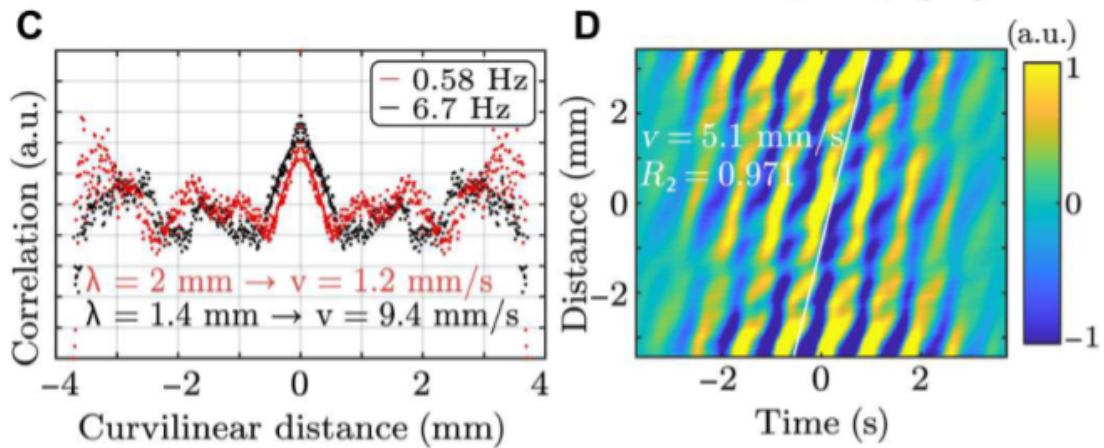


Figure 5.6

Resultats

Imagerie Grand Champ et Correction des Aberrations

Pour maximiser le champ-de-vue façonner le faisceau laser illuminant la rétine, nous plaçons une lentille devant l'œil du patient. En conséquence, le faisceau laser est focalisé devant l'œil du patient, créant un point chaud où la concentration locale de puissance dépasse les limites de sécurité pour le segment antérieur de l'œil. Un diffuseur a été introduit dans le chemin d'illumination de l'objet pour atténuer ce problème et créer une configuration totalement sécurisée.

La résolution des images obtenues avec la LDH peut être compromise par la présence d'aberrations oculaires ou de mouvements axiaux de l'œil, qui agissent effectivement comme un défocus. Pour atténuer la distorsion du front d'onde, nous avons opté pour une approche d'optique adaptative (AO) numérique basée sur la détection du front d'onde par corrélation croisée des images reconstruites à partir de sous-ouvertures dans le plan pupillaire. Pour relever les défis spécifiques résultant du schéma de détection holographique, nous proposons l'utilisation d'images redimensionnées pour l'évaluation des décalages dans les sous-images. La comparaison entre deux méthodes de reconstruction du front d'onde - régularisation par polynômes de Zernike et intégration de gradient - suggère que, dans le cas spécifique de la LDH, la seconde méthode permet d'obtenir des images mieux résolues.

5.5 Quantification du Flux Sanguin et Elastographie des Vaisseaux Rétiniens

Il a été démontré précédemment que le signal détecté avec la LDH permet la détection de formes d'ondes dans les artères et les veines. Cependant, le signal mesuré n'a jamais pu être quantifié. Dans ce manuscrit, nous développons un modèle permettant de lier le spectre d'hogrammes détectés avec la vitesse locale. De plus, nous avons estimé à 100 kHz la fréquence d'échantillonnage requise pour fournir une bonne approximation de la solution analytique du problème.

Les données LDH peuvent également être employées pour les mesures élastographiques. Une

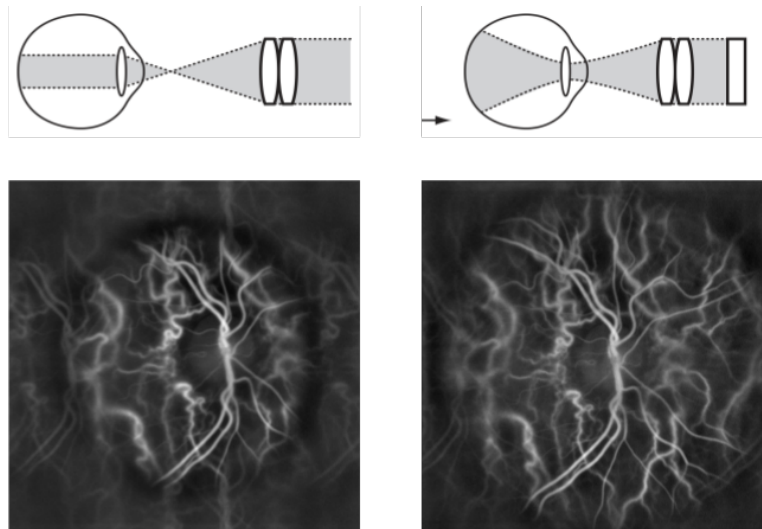


Figure 5.7

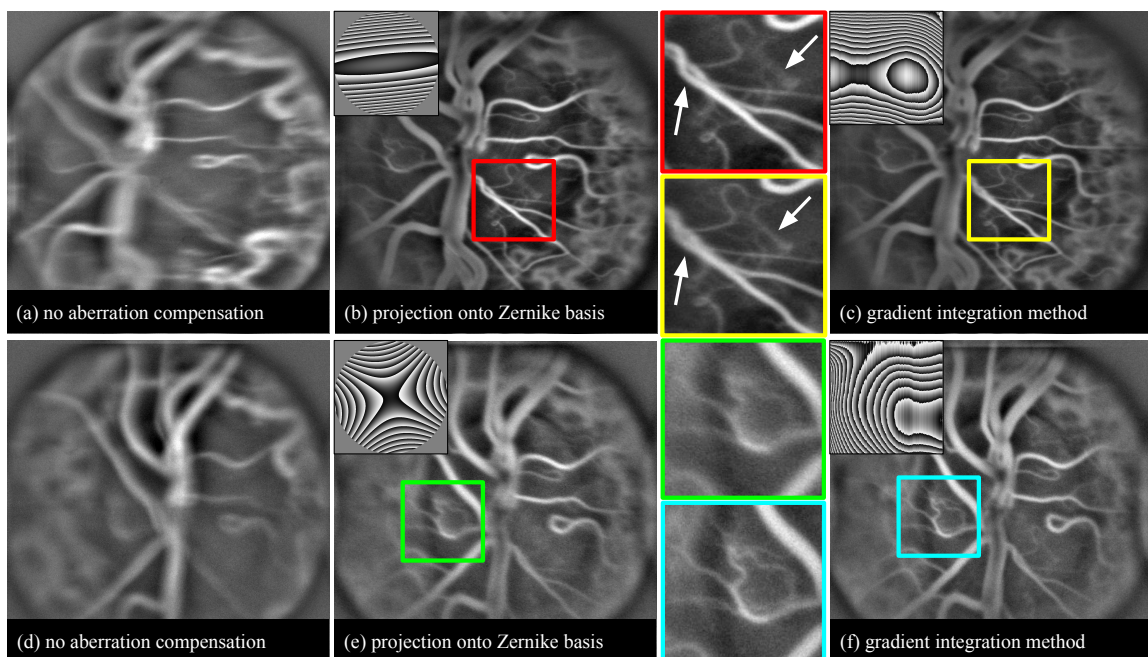
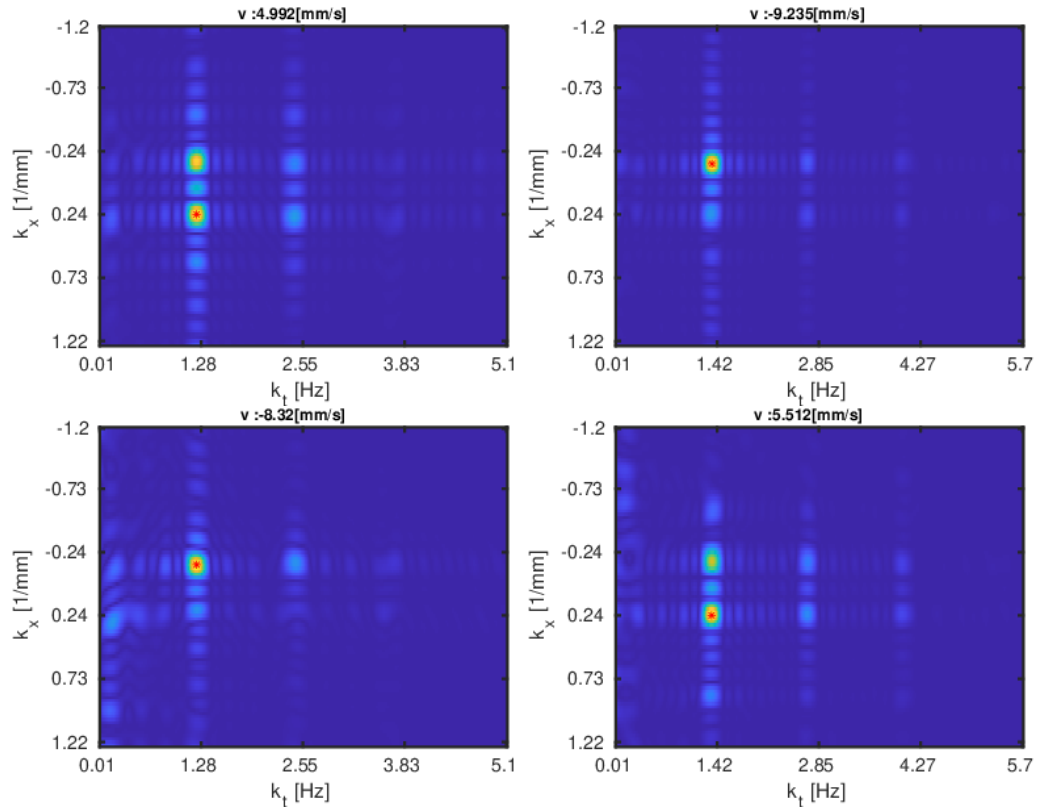


Figure 5.8: Les images holographiques Doppler de la région papillaire de la rétine d'un volontaire qui tient une lentille de 6D pour l'astigmatisme devant son œil. L'expérience est répétée deux fois (a, d). Lors de la reconstruction des images, nous appliquons un algorithme numérique de Shack-Hartmann pour mesurer le front d'onde des aberrations. Dans les images (b, e), le front d'onde est projeté sur la base des polynômes de Zernike, et dans (c, f), il est reconstruit en utilisant la technique d'intégration de gradient. Les images représentées ci-dessus sont moyennées sur plusieurs images d'une vidéo.



(a) 67 kHz interferogram sampling rate

(b) 30 kHz interferogram sampling rate

Figure 5.9: Les mesures de temps de vol sont représentées dans l'espace de Fourier pour les veines (rangée du haut) et les artères (rangée du bas). Les données acquises avec des cadences de 67 kHz (a) et 30 kHz (b) sont prises en compte.

partie de ce manuscrit est dédiée à l'automatisation du processus d'estimation de l'élasticité. La difficulté de réalisation de mesures précises est due à la confusion des signaux provenant d'artères et d'autres tissus causée par la diffusion multiple. Enfin, nos mesures par temps de vol indiquent que l'onde de flexion d'énergie maximale se propage dans les artères et les veines dans des directions opposées, c'est-à-dire dans la direction du flux sanguin.

5.6 Perspectives et Conclusions

La LDH représente une avancée significative dans le domaine de l'imagerie rétinienne, avec un potentiel d'application étendu au diagnostic précoce des maladies oculaires et systémiques. Les travaux futurs devraient se concentrer sur la démonstration que le Shack-Hartmann numérique avec intégration de gradient est l'approche la plus optimale de compensation d'aberration pour la LDH, et sur le développement d'un meilleur modèle capable de prédire les courbes de dispersion pour les ondes de flexion se propageant dans les vaisseaux rétiniens et sur le développement de modèles plus précis pour la quantification du flux sanguin.

En conclusion, l'holographie Doppler laser offre des possibilités uniques pour la détection des pathologies oculaires, grâce à sa capacité à fournir des images détaillées et dynamiques du flux sanguin dans l'œil. Les perspectives d'amélioration technologique et d'application clinique font de la LDH un domaine de recherche prometteur pour les années à venir.

Bibliography

- [1] Pedro Baracal de Mece. *4D exploration of the retina for Adaptive Optics-assisted laser photocoagulation*. Phd thesis, Sorbonne Paris Cité, 2018.
- [2] Leo Puyo. *Clinical application of laser Doppler holography in ophthalmology*. Phd thesis, PSL University, 2019.
- [3] Epuri Kumar and Shoba Chigarapalle. Two-stage framework for optic disc segmentation and estimation of cup-to-disc ratio using deep learning technique. *Journal of Ambient Intelligence and Humanized Computing*, 03 2021.
- [4] B. Anand-Apte and J.G. Hollyfield. Developmental Anatomy of the Retinal and Choroidal Vasculature. In *Encyclopedia of the Eye*, pages 9–15. Elsevier, 2010.
- [5] Lamprini Banou, Anna Dastiridou, Athanasios Giannoukas, Georgios Kouvelos, Christos Baros, and Sofia Androudi. The Role of Color Doppler Imaging in the Diagnosis of Glaucoma: A Review of the Literature. *Diagnostics*, 13(4):588, February 2023.
- [6] Albert Alm and Anders Bill. The Oxygen Supply to the Retina, II. Effects of High Intraocular Pressure and of Increased Arterial Carbon Dioxide Tension on Uveal and Retinal Blood Flow in Cats: A study with radioactively labelled microspheres including flow determinations in brain and some other tissues. *Acta Physiologica Scandinavica*, 84(3):306–319, March 1972.
- [7] Mircea Mujat, Yang Lu, Gopi Maguluri, Youbo Zhao, Nicusor Iftimia, and R. Daniel Ferguson. Visualizing the vasculature of the entire human eye posterior hemisphere without a contrast agent. *Biomedical Optics Express*, 10(1):167, January 2019.
- [8] Michel E. Safar and P. Lacolley. Disturbance of macro- and microcirculation: relations with pulse pressure and cardiac organ damage. *American Journal of Physiology-Heart and Circulatory Physiology*, 293(1):H1–H7, July 2007.
- [9] Galina Dimitrova and Satoshi Kato. Color Doppler Imaging of Retinal Diseases. *Survey of Ophthalmology*, 55(3):193–214, May 2010.
- [10] Michel E. Safar. Arterial stiffness as a risk factor for clinical hypertension. *Nature Reviews Cardiology*, 15(2):97–105, February 2018.
- [11] Yukihiro Shiga, Hiroshi Kunikata, Naoko Aizawa, Naoki Kiyota, Yukiko Maiya, Yu Yokoyama, Kazuko Omodaka, Hidetoshi Takahashi, Tomoki Yasui, Keiichi Kato, Aiko Iwase, and Toru Nakazawa. Optic Nerve Head Blood Flow, as Measured by Laser Speckle Flowgraphy, Is Significantly Reduced in Preperimetric Glaucoma. *Current Eye Research*, 41(11):1447–1453, November 2016.

- [12] Hedwig J. Kaiser, Andreas Schoetzau, Daniela Stumpfig, and Josef Flammer. Blood-flow velocities of the extraocular vessels in patients with high-tension and normal-tension primary open-angle glaucoma. *123(3):320–327*.
- [13] J Flammer. Optic nerve blood-flow abnormalities in glaucoma. *17(2):267–289*.
- [14] Xingdi Wu, Katarzyna Konieczka, Xin Liu, Min Chen, Ke Yao, Kaijun Wang, and Josef Flammer. Role of ocular blood flow in normal tension glaucoma. *2(1):100036*.
- [15] William H. Morgan, Martin L. Hazelton, and Dao-Yi Yu. Retinal venous pulsation: Expanding our understanding and use of this enigmatic phenomenon. *Progress in Retinal and Eye Research*, 55:82–107, November 2016.
- [16] Allen C. Clermont and Sven-Erik Bursell. Retinal Blood Flow in Diabetes. *Microcirculation*, 14(1):49–61, January 2007.
- [17] T M Curtis, T A Gardiner, and A W Stitt. Microvascular lesions of diabetic retinopathy: clues towards understanding pathogenesis? *Eye*, 23(7):1496–1508, July 2009.
- [18] Vinod Patel, Salwan Rassam, Richard Newsom, Jutta Wiek, and Eva Kohner. Retinal blood flow in diabetic retinopathy. *BMJ*, 305:678–83, 1992.
- [19] Léa Krafft. *Spatial filtering for flood illumination ophthalmoscope*. Phd thesis, Paris-Saclay University, 2022.
- [20] Damien Gatinel, Radhika Rampat, Laurent Dumas, and Jacques Malet. An alternative wave-front reconstruction method for human eyes. *36(2):74–81*.
- [21] H. Hashemi, A. Fotouhi, A. Yekta, R. Pakzad, H. Ostadimoghaddam, and Khabazkhoob M. Global and regional estimates of prevalence of refractive errors: Systematic review and meta-analysis. *Curr Ophthalmol*, 30(1):3–22, March 2018.
- [22] José Francisco Castejón-Mochón, Norberto López-Gil, Antonio Benito, and Pablo Artal. Ocular Wave-Front Aberration Statistics in a Normal Young Population. *Vision Research*, 42(13):1611–17, 2002.
- [23] Damien Gatinel. <https://www.gatinel.com/recherche-formation/astigmatisme/astigmatisme-regulier-et-irregulier/>, 2016.
- [24] Jessica Jarosz, Pedro Mecê, Jean-Marc Conan, Cyril Petit, Michel Paques, and Serge Meimon. High temporal resolution aberrometry in a 50-eye population and implications for adaptive optics error budget. *Biomedical Optics Express*, 8(4):2088, April 2017.
- [25] Pedro Mecê, Jessica Jarosz, Jean-Marc Conan, Cyril Petit, Kate Grieve, Michel Paques, and Serge Meimon. Fixational eye movement: a negligible source of dynamic aberration. *Biomedical Optics Express*, 9(2):717, February 2018.
- [26] A Roorda, CA Garcia, JA Martin, S Poonja, H Queener, F Romero-Borja, R Sepulveda, K Venkateswaran, and Y Zhang. What can adaptive optics do for a scanning laser ophthalmoscope ? *Bull Soc Belge Ophtalmol*, 302:231–44, 2006.
- [27] Susana Martinez-Conde, Stephen L. Macknik, and David H. Hubel. The role of fixational eye movements in visual perception. *Nature Reviews Neuroscience*, 5(3):229–240, March 2004.

- [28] Yao Cai, Kate Grieve, and Pedro Mecê. Characterization and analysis of retinal axial motion at high spatiotemporal resolution and its implication for real-time correction in human retinal imaging. 9:868217.
- [29] Etienne Cuche, Pierre Marquet, and Christian Depeursinge. Spatial filtering for zero-order and twin-image elimination in digital off-axis holography. *Appl. Opt.*, 39(23):4070–4075, Aug 2000.
- [30] Joseph W Goodman. Introduction to fourier optics. *Introduction to Fourier optics, 3rd ed., by JW Goodman. Englewood, CO: Roberts & Co. Publishers, 2005*, 1, 2005.
- [31] R. Bonner and R. Nossal. Model for laser Doppler measurements of blood flow in tissue. *Applied Optics*, 20(12):2097, June 1981.
- [32] Charles Riva, Benjamin Ross, and George B Benedek. Laser Doppler measurements of blood flow in capillary tubes and retinal arteries. 11, 1972.
- [33] L. Puyo, M. Paques, M. Fink, J.-A. Sahel, and M. Atlan. In vivo laser Doppler holography of the human retina. *Biomedical Optics Express*, 9(9):4113, September 2018.
- [34] Léo Puyo, Michel Paques, and Michael Atlan. Spatio-temporal filtering in laser Doppler holography for retinal blood flow imaging. *Biomedical Optics Express*, 11(6):3274, June 2020.
- [35] Charlie Demene, Thomas Deffieux, Mathieu Pernot, Bruno-Felix Osmanski, Valerie Biran, Jean-Luc Gennisson, Lim-Anna Sieu, Antoine Bergel, Stephanie Franqui, Jean-Michel Correas, Ivan Cohen, Olivier Baud, and Mickael Tanter. Spatiotemporal Clutter Filtering of Ultrafast Ultrasound Data Highly Increases Doppler and fUltrasound Sensitivity. *IEEE Transactions on Medical Imaging*, 34(11):2271–2285, November 2015.
- [36] Leo Puyo, Michel Paques, and Michael Atlan. Reverse contrast laser Doppler holography for lower frame rate retinal and choroidal blood flow imaging. *Optics Letters*, 45(14):4012, July 2020. arXiv:2004.00007 [physics].
- [37] Léo Puyo, Michel Paques, Mathias Fink, José-Alain Sahel, and Michael Atlan. Waveform analysis of human retinal and choroidal blood flow with laser Doppler holography. *Biomedical Optics Express*, 10(10):4942, October 2019.
- [38] Léo Puyo, Michel Paques, Mathias Fink, José-Alain Sahel, and Michael Atlan. Choroidal vasculature imaging with laser Doppler holography. *Biomedical Optics Express*, 10(2):995, February 2019.
- [39] Gabrielle Laloy-Borgna, Léo Puyo, Hidero Nishino, Michael Atlan, and Stefan Catheline. Observation of natural flexural pulse waves in retinal and carotid arteries for wall elasticity estimation. *Science Advances*, 9(25):eadf1783, June 2023.
- [40] Denos C. Gazis. Three-Dimensional Investigation of the Propagation of Waves in Hollow Circular Cylinders. I. Analytical Foundation. *The Journal of the Acoustical Society of America*, 31(5):568–573, May 1959.
- [41] Hideo Nishino, Sunao Takashina, Fukutoshi Uchida, Mikio Takemoto, and Kanji Ono. Modal Analysis of Hollow Cylindrical Guided Waves and Applications. *Japanese Journal of Applied Physics*, 40(1R):364, January 2001.

- [42] Gabrielle Laloy Borgna. Micro-élastographie : caractérisation mécanique de la cellule par ondes élastiques.
- [43] H W Babcock. THE POSSIBILITY OF COMPENSATING ASTRONOMICAL SEEING.
- [44] Junzhong Liang, David R. Williams, and Donald T. Miller. Supernormal vision and high-resolution retinal imaging through adaptive optics. *Journal of the Optical Society of America A*, 14(11):2884, November 1997.
- [45] Austin Roorda, Fernando Romero-Borja, William J. Donnelly Iii, Hope Queener, Thomas J. Hebert, and Melanie C.W. Campbell. Adaptive optics scanning laser ophthalmoscopy. *Optics Express*, 10(9):405, May 2002.
- [46] Pooja Godara, Adam M. Dubis, Austin Roorda, Jacque L. Duncan, and Joseph Carroll. Adaptive Optics Retinal Imaging: Emerging Clinical Applications. *Optometry and Vision Science*, 87(12):930–941, December 2010.
- [47] Joy A. Martin and Austin Roorda. Direct and Noninvasive Assessment of Parafoveal Capillary Leukocyte Velocity. *Ophthalmology*, 112(12):2219–2224, December 2005.
- [48] Karen M. Hampson, Raphaël Turcotte, Donald T. Miller, Kazuhiro Kurokawa, Jared R. Males, Na Ji, and Martin J. Booth. Adaptive optics for high-resolution imaging. *Nature Reviews Methods Primers*, 1(1):68, October 2021.
- [49] Changgeng Liu, Xiao Yu, and Myung K. Kim. Phase aberration correction by correlation in digital holographic adaptive optics. *Applied Optics*, 52(12):2940, April 2013.
- [50] Dierck Hillmann, Hendrik Spahr, Carola Hain, Helge Sudkamp, Gesa Franke, Clara Pfäffle, Christian Winter, and Gereon Hüttmann. Aberration-free volumetric high-speed imaging of in vivo retina. *Scientific Reports*, 6(1):35209, October 2016.
- [51] Dawid Borycki, Egidijus Auksorius, Piotr Wegrzyn, and Maciej Wojtkowski. Computational aberration correction in spatiotemporal optical coherence (STOC) imaging. *Optics Letters*, 45(6):1293, March 2020.
- [52] Abhishek Kumar, Wolfgang Drexler, and Rainer A Leitgeb. Subaperture correlation based digital adaptive optics for full field optical coherence tomography. 2013.
- [53] Laurin Ginner, Abhishek Kumar, Daniel Fechtig, Lara M. Wurster, Matthias Salas, Michael Pircher, and Rainer A. Leitgeb. Noniterative digital aberration correction for cellular resolution retinal optical coherence tomography in vivo. *Optica*, 4(8):924, August 2017.
- [54] Myung K Kim. Adaptive optics by incoherent digital holography.
- [55] Changgeng Liu and Myung K Kim. Digital holographic adaptive optics for ocular imaging: proof of principle.
- [56] Amaury Badon, Victor Barolle, Kristina Irsch, A. Claude Boccara, Mathias Fink, and Alexandre Aubry. Distortion matrix concept for deep optical imaging in scattering media. *Science Advances*, 6(30):eaay7170, July 2020.
- [57] Abhishek Kumar, Wolfgang Drexler, and Rainer A. Leitgeb. Numerical focusing methods for full field OCT: a comparison based on a common signal model. *Optics Express*, 22(13):16061, June 2014.

- [58] Fredrick A. South, Kazuhiro Kurokawa, Zhuolin Liu, Yuan-Zhi Liu, Donald T. Miller, and Stephen A. Boppart. Combined hardware and computational optical wavefront correction. *9(6):2562*.
- [59] Weizhong Lan, Zhenghua Lin, Zhikuang Yang, and Pablo Artal. Two-dimensional Peripheral Refraction and Retinal Image Quality in Emmetropic Children. *Scientific Reports*, 9(1):16203, November 2019.
- [60] Anthony Podkowa, Michael Oelze, and Jeffrey Ketterling. High-Frame-Rate Doppler Ultrasound Using a Repeated Transmit Sequence. *Applied Sciences*, 8(2):227, February 2018.
- [61] Charles E. Riva, Gilbert T. Feke, Bruno Eberli, and Vili Benary. Bidirectional LDV system for absolute measurement of blood speed in retinal vessels. *Applied Optics*, 18(13):2301, July 1979.
- [62] Frederic Truffer, Martial Geiser, Marc-Antoine Chappelet, Helene Strese, Gilbert Maître, Serge Amoos, Florent Aptel, and Christophe Chiquet. Absolute retinal blood flowmeter using a laser Doppler velocimeter combined with adaptive optics. *Journal of Biomedical Optics*, 25(11), November 2020.
- [63] C E Riva, G T Feke, B Eberli, and V Benary. Bidirectional LDV system for absolute measurement of blood speed in retinal vessels. *Appl. Opt.*, 18(13):2301–2306, July 1979.
- [64] Balwantray C. Chauhan. Confocal Scanning Laser Doppler Flowmetry in the Rat Retina: Origin of Flow Signals and Dependence on Scan Depth. *Archives of Ophthalmology*, 124(3):397, March 2006.
- [65] Zhongping Chen, Thomas E. Milner, Shyam Srinivas, Xiaojun Wang, Arash Malekafzali, Martin J. C. Van Gemert, and J. Stuart Nelson. Noninvasive imaging of in vivo blood flow velocity using optical Doppler tomography. *Optics Letters*, 22(14):1119, July 1997.
- [66] R. Leitgeb, C. Hitzenberger, and Adolf Fercher. Performance of fourier domain vs time domain optical coherence tomography. *Optics Express*, 11(8):889, April 2003.
- [67] Rainer A. Leitgeb, René M. Werkmeister, Cedric Blatter, and Leopold Schmetterer. Doppler Optical Coherence Tomography. *Progress in Retinal and Eye Research*, 41:26–43, July 2014.
- [68] Edward James. Frangi vesselness segmentation. *GitHub repository*, 2023.
- [69] Leo Puyo. Clinical application of laser Doppler holography in ophthalmology.
- [70] E Gordon-Lipkin, B Chodkowski, D S Reich, S A Smith, and M Pulicken. Retinal nerve fiber layer is associated with brain atrophy in multiple sclerosis. 2007.
- [71] Thomas Weber, Johann Auer, Michael F. O’Rourke, Erich Kvas, Elisabeth Lassnig, Robert Berent, and Bernd Eber. Arterial Stiffness, Wave Reflections, and the Risk of Coronary Artery Disease. *Circulation*, 109(2):184–189, January 2004.
- [72] T Hirai, S Sasayama, T Kawasaki, and S Yagi. Stiffness of systemic arteries in patients with myocardial infarction. A noninvasive method to predict severity of coronary atherosclerosis. *Circulation*, 80(1):78–86, July 1989.
- [73] WW Nichols and CJ Pepine. Ventricular/vascular interaction in health and heart failure. *Comprehensive therapy*, 18(7):12—19, July 1992.

- [74] Stéphane Laurent, Sandrine Katsahian, Céline Fassot, Anne-Isabelle Tropeano, Isabelle Gautier, Brigitte Laloux, and Pierre Boutouyrie. Aortic Stiffness Is an Independent Predictor of Fatal Stroke in Essential Hypertension. *Stroke*, 34(5):1203–1206, May 2003.
- [75] Stéphane Laurent, Pierre Boutouyrie, Roland Asmar, Isabelle Gautier, Brigitte Laloux, Louis Guize, Pierre Ducimetiere, and Athanase Benetos. Aortic Stiffness Is an Independent Predictor of All-Cause and Cardiovascular Mortality in Hypertensive Patients. *Hypertension*, 37(5):1236–1241, May 2001.
- [76] P V Vaitkevicius, J L Fleg, J H Engel, F C O’Connor, J G Wright, L E Lakatta, F C Yin, and E G Lakatta. Effects of age and aerobic capacity on arterial stiffness in healthy adults. *Circulation*, 88(4):1456–1462, October 1993.
- [77] Louise Marais, Mathieu Pernot, Hakim Khettab, Mickael Tanter, Emmanuel Messas, Mustapha Zidi, Stéphane Laurent, and Pierre Boutouyrie. Arterial Stiffness Assessment by Shear Wave Elastography and Ultrafast Pulse Wave Imaging: Comparison with Reference Techniques in Normotensives and Hypertensives. *Ultrasound in Medicine & Biology*, 45(3):758–772, March 2019.
- [78] Shigeo Godo, Michel T. Corban, Takumi Toya, Rajiv Gulati, Lilach O. Lerman, and Amir Lerman. Association of coronary microvascular endothelial dysfunction with vulnerable plaque characteristics in early coronary atherosclerosis. *EuroIntervention*, 16(5):387–394, August 2020.
- [79] Jay N. Cohn. Arterial Stiffness, Vascular Disease, and Risk of Cardiovascular Events. *Circulation*, 113(5):601–603, February 2006.
- [80] Mahdiah Rezaeian, S. Mojtaba Golzan, Alberto P. Avolio, Stuart Graham, and Mark Butlin. The Association between Retinal and Central Pulse Wave Velocity in the Elderly. *Artery Research*, 26(3):148–153, September 2020.
- [81] Konstantin Kotliar, Henner Hanssen, Karla Eberhardt, Walthard Vilser, Christoph Schmaderer, Martin Halle, Uwe Heemann, and Marcus Baumann. Retinal Pulse Wave Velocity in Young Male Normotensive and Mildly Hypertensive Subjects. *Microcirculation*, 20(5):405–415, July 2013.
- [82] Hendrik Spahr, Dierck Hillmann, Carola Hain, Clara Pfäffle, Helge Sudkamp, Gesa Franke, and Gereon Hüttmann. Imaging pulse wave propagation in human retinal vessels using full-field swept-source optical coherence tomography. *Optics Letters*, 40(20):4771, October 2015.
- [83] Qian Li, Lin Li, Shanhui Fan, Cuixia Dai, Xinyu Chai, and Chuanqing Zhou. Retinal pulse wave velocity measurement using spectral-domain optical coherence tomography. *Journal of Biophotonics*, 11(20), October 2018.
- [84] Léo Puyo, Hendrik Spahr, Clara Pfäffle, Gereon Hüttmann, and Dierck Hillmann. Retinal blood flow imaging with combined full-field swept-source optical coherence tomography and laser doppler holography. *Opt. Lett.*, 47(5):1198–1201, Mar 2022.

RÉSUMÉ

L'holographie laser Doppler (HLD) est une technique relativement nouvelle conçue pour imager le flux sanguin dans le fond de l'œil. Ce travail présente des avancées qui rapprochent l'HLD de l'utilisation clinique et exploitent les données acquises pour obtenir des biomarqueurs pertinents. Dans la première partie, une correction d'aberration numérique basée sur la corrélation de sous-ouvertures a été mise en œuvre et adaptée aux exigences uniques de l'holographie. De plus, un premier modèle de quantification du flux sanguin a été proposé. Par ailleurs, sur la base d'une démonstration antérieure de la faisabilité des mesures d'élastographie rétinienne, un traitement permettant d'améliorer le rapport signal/bruit (SNR) et d'automatiser l'analyse a été proposé. Une comparaison préliminaire entre les artères et les veines a été effectuée.

MOTS CLÉS

holographique, imagerie, ophtalmologie, Doppler

ABSTRACT

Laser Doppler holography (LDH) is a relatively new technique designed to image blood flow in the eye fundus. This work presents advancements that bring LDH closer to clinical use and exploit the acquired data to obtain relevant biomarkers. In the first part, a subaperture correlation-based digital aberration correction was implemented and adapted to the unique requirements of holography. Additionally, a first model for blood flow quantification was proposed. Furthermore, based on a previous demonstration of feasibility of retinal elastography measurements, processing allowing to improve the SNR and automate the analysis was proposed. A preliminary comparison between arteries and veins was performed.

KEYWORDS

holography, imaging, ophthalmology, Doppler

